Ab-initio STUDIES OF STRUCTURAL, ELECTRONIC, MAGNETIC AND OPTICAL PROPERTIES OF NICKEL OXIDE

BY

FELIX DUSABIRANE

A THESIS SUBMITTED IN PARTIAL FULFILMENT OF THE REQUIREMENTS FOR THE DEGREE OF MASTER OF SCIENCE IN PHYSICS IN THE SCHOOL OF SCIENCE

UNIVERSITY OF ELDORET, KENYA.

2014

This page is intentionally left blank.

DECLARATION

Declaration by the Candidate

This thesis is my original work and has not been presented for a degree in any other University. No part of this thesis may be reproduced without the prior written permission of the author and/or University of Eldoret.

Felix Dusabirane

Signature: ..... Date: .....

SC/PGP/010/12

Declaration by Supervisors

This thesis has been submitted for examination with our approval as University of Eldoret supervisors.

Signature: ..... Date: .....

Prof. George O. Amolo,

Department of Physics, University of Eldoret, Eldoret, Kenya

Signature: ..... Date: .....

Dr. Nicholas W. Makau,

Department of Physics, University of Eldoret, Eldoret, Kenya

DEDICATION

To my family

ABSTRACT

Nickel Oxide (NiO) has many applications in solar energy utilization, due to variations in electronic, optical and magnetic properties. However, a satisfactory description of its properties is still not available. There is therefore need to understand its properties using theoretical predictions, so as to facilitate a deeper knowledge of the characteristics of this important material. In this work, the NiO ground state properties have been studied using Quantum-ESPRESSO code, while the optical properties are investigated using *Yambo* code. The ground state properties of NiO are determined using the Local Spin Density Approximation with Hubbard interaction energy (LSDA+U) method. The Hubbard values of 5.4 eV, 6.2 eV, 7.3 eV, 8 eV, 8.5 eV, 9 eV, 9.5 eV, 10 eV and 12 eV have been used, whereby a Hubbard term of 9.5 eV has given the results that are closer to other theoretical and experimental findings. The calculated lattice parameters are found to increase with increasing U term, and for a Hubbard term of 9.5 eV, the value of 9.652 a.u is obtained for rhombohedral (RHL) NiO with a rhombohedral angle α_{rh} = 33.557^0. The bulk modulus is found to decrease with increasing U value, giving values of 224.5 GPa, for RHL NiO with α_{rh} = 33.557^0, when a U term of 9.5 eV was used. LSDA and LSDA+U predicted RHL NiO with α_{rh} = 60.08^0 to be a metal, while it is expected to be an insulator. For RHL NiO with α_{rh} = 33.557^0, the LSDA calculations have revealed very narrow indirect and direct energy band gaps of 0.61 eV and 0.85 eV, respectively, whereas they are increased up to 3.05 eV and 3.65 eV, respectively, upon the addition of a U term of 9.5 eV. The projected density of states shows that RHL NiO with α_{rh} = 33.557^0 is a charge transfer insulator. The LSDA and LSDA+U calculations further have predicted both structures of RHL NiO with α_{rh} = 60.08^0 and α_{rh} = 33.557^0 to be antiferromagnetic materials. The Green function and the dynamically screened interaction (GW), as well as the Bethe Salpeter Equation (BSE) have been used to study the absorption energy and the electron energy loss spectra. GW is found to overestimate the value of the fundamental energy band gap of NiO, while BSE gives a better prediction of the optical energy band gap. For RHL NiO with α_{rh} = 33.557^0, both the optical indirect and direct band gaps are found to be 3.34 eV and 3.74 eV, respectively. The absorption spectra obtained from BSE calculations show that there is minimal absorption in the range of the infrared to the visible region and stronger absorption towards the ultraviolet region. The maximum light absorbed by NiO with α_{rh} = 33.557^0 was found to be in the ultraviolet wavelength region near 330 nm (3.74 eV) and this makes NiO a good absorber in the ultraviolet region of the electromagnetic spectrum.

TABLE OF CONTENTS

LIST OF TABLES

LIST OF FIGURES

LIST OF ABBREVIATIONS, ACRONYMS AND SYMBOLS

NiO	Nickel oxide
RHL	Rhombohedral
fcc	Face centered cubic
DFT	Density Functional Theory
LDA	Local Density Approximation
GGA	Generalized Gradient Approximation
LSDA	Local Spin Density Approximation
U	Hubbard interaction energy
HF	Hartree-Fock
KS	Kohn-Sham
MBPT	Many-body perturbation theory
GW	Green function and dynamically screened interaction
BSE	Bethe Salpeter Equation
RPA	Random Phase Approximation
ESPRESSO	opEn Source Package for Research in Electronic Structure, Simulation, and Optimization
BZ	Brillouin zone
T_N	Néel temperature
AF	Antiferromagnetic
FM	Ferromagnetic
NM	Non magnetic
TM	Transition metals
UV	Utltraviolet

Vis	Visible
NIR	Near Infrared
DOS	Density of states
PDOS	Projected density of states
XRD	X-ray diffraction
TEM	Transmission electron microscope
SEM	Scanning electron microscopy
PL	Photoluminescence
AFM	Atomic force microscope
ALFDT	Automated Liquid Flow Deposition Technique
SCP	Standard Critical Point model
EEL	Electron energy loss
LCAO	Linear combination of atomic orbitals
FLAPW	Full potential linearized augmented plane wave
LAPW	Linearized augmented plane wave
LMTO	Linear muffin-tin orbital
NaCl	Sodium chloride
E_F	Fermi energy
E_g	Energy band gap
E_{min}	Energy minimum
Å	Angstrom
$a.u$	Atomic unit
B_0	Bulk modulus
B'_0	Derivative of bulk modulus

eV	Electron-volt
Ry	Rydberg
nm	nanometer
GPa	Giga-Pascal
K	Kelvin degree
μ_B	Bohr magneton
α_{rh}	Rhombohedral angle
$\hat{H}$	Total Hamiltonian
$\hat{H}_e$	Electronic Hamiltonian
Ψ	Many body wave function
ψ	Electron wave function
E	Hamiltonian Total Energy
ϵ	Energy per electron
r_i	Electron position
R_i	Nuclei position
M_I	Mass of a nucleus
m_i	Mass of an electron
$\hbar$	Plank constant
Z_i	Atomic number of nucleus
σ_i	Spin coordinates
n	Ground state charge density
n_{ind}	Induced charge density
T	Kinetic energy
J	Spin exchange interaction

E_{xc}	Exchange-correlation energy
V_{xc}	Exchange-correlation potential
Σ	Self-energy
Γ	Vertex function
P	Irreducible polarizability
G	Dyson equation
V	Screened Coulomb interaction
v	Bare Coulomb interaction
L	Electron–hole Green's function
ε	Dielectric function
ε_M	Macroscopic dynamical dielectric function
χ	Reducible polarizability
ω	Frequency
q	Wave vector
∇	The gradient (Partial differential)
∇^2	Second derivative of the gradient
N	Number of electron
$F[n(r)]$	Universal functional of the charge density
ξ	Fractional spin polarization
$n^{\uparrow}$	Density of spin up electrons
$n^{\downarrow}$	Density of spin down electrons
m	Quantum number
a, b, c	Lattice constants
@	Based at

ACKNOWLEDGEMENTS

I would like to thank the University of Eldoret, and in particular the Department of Physics, for use of its facilities. I wish to appreciate University of Rwanda, College of Agriculture, Animal Sciences and Veterinary Medicine (UR-CAVM) for giving me the study leave. It is a pleasure to acknowledge my supervisors, Prof. George O. Amolo and Dr. Nicholas W. Makau. Thank you for offering me an opportunity to work under your supervision and learn with you. You were always available for support and guidance throughout this work. I appreciate the helpful discussions and corrections you made to this work. I would like also to thank Prof. Daniel P. Joubert of the University of the Witwatersrand, Johannesburg, South Africa, for the assistance he rendered during this work. I wish to acknowledge the developers of Quantum ESPRESSO and *Yambo* codes that I used in all calculations in this work. I would like to express my deep gratitude to the family of Innocent Rwandanga and Marie Yvonne Ingabire. Thank you very much for your assistance. I would like also to thank my friend Fébronie Dusingizimana for her support and encouragement. I thank the members of Computational Material Science Group of University of Eldoret, for sharing their experiences and for providing a cheerful atmosphere in the laboratory. I thank my parents, my brothers and my sisters; you have been ever helpful. Last, but by no means least, I acknowledge all of the rest of my friends for their support and encouragement, whatever it is, I really appreciate.

CHAPTER ONE

INTRODUCTION

1.1 Nickel oxide

Nickel oxide (NiO) is a semitransparent semiconducting material with a wide band gap in the range of 3.5-4.0 eV [1–8]. It is a well known antiferromagnetic (AF) material with strong electronic correlations and high spin structure at low temperatures. It has a Néel Temperature (T_N) of 523 K and has a cubic rock salt structure with a lattice constant of 0.4168 nm above its T_N [1, 5, 9]. Below 523 K, the NiO transforms to a rhombohedral distorted rock salt structure by a compression along the body diagonal direction with the rhombohedral angle α_{rh} of 60.08^0 or 33.557^0 [2, 10–12].

The NiO conduction band is made up of mainly the nickel atom 3d orbitals while the valence band consists of Ni d states with O 2p states. In NiO the d band is expected to be partly full, since Ni^{2+} has 8d electrons and the band can hold 10 electrons [13], but instead the d band is split into a completely filled part and an empty part and this makes NiO a strongly-correlated material.

1.2 *Ab initio* studies

In the last few decades, great advances [14–16] have been seen in both theoretical methodology and computer technology that have allowed researchers to investigate materials properties from first principles (i.e., without any input parameters other than the constituent atoms making up the material). Today, the ground-state and excited states properties for a wide range of materials, particularly for reduced dimensional systems characterized by enhanced many-electron interaction effects, can be predicted using first principles techniques [14]. In principle, determining the properties of a material from first principles involves solving the Schrodinger equation for a quantum many-body interacting system. However, its exact numerical solution is impractical, due to the size of the system. Therefore, the evaluation of physical quantities of interacting systems requires some approximations.

In the solid state, the majority of electronic structure calculations are done by the Kohn-Sham equations within the density functional theory (DFT) using either the local density approximation (LDA), the local spin density approximation (LSDA) or generalized gradient approximation (GGA), where the many-body problem is solved considering a non-interacting system with a one-electron exchange correlation potential [17]. DFT is used in many circumstances, since it gives results which are accurate enough to help interpret experimental data or to have some predictive power, and leads to calculations which are computationally cheap in comparison to more sophisticated methods [15].

LSDA and GGA have proved to be very efficient for extended systems, but as an approximation, they cannot be successful for all systems although the exact DFT should be capable of obtaining ground-state properties. The strongly correlated materials are examples where deficiency of the LDA and GGA are seen most clearly. Such systems usually contain transition metals (TM) or rare-earth metal ions with partially filled d (or f) shells [18]. Therefore, depending on the solid being studied and its properties, the application of DFT can lead to results which are in very bad agreement with experiments. An example, is the band gap of semiconductors and insulators which is normally underestimated or even absent. Better band gap calculations can be obtained using other methods such as Hybrid functionals and LSDA+U, where the parameter U is the Hubbard interaction or Coulomb energy, which is one among the methods used for strongly correlated materials [18–21].

1.3 Problem statement

NiO is one of the most commonly used TM oxides for a wide range of applications. NiO thin films and nanoparticles are functional materials that have attracted extensive interests due to their novel optical, electronic, magnetic, thermal, and mechanical properties and associated potential applications [3, 22]. It has been the subject of extensive experimental and theoretical investigations for the past decade and understanding of its electronic structure has been a topic of great interest to many researchers. However, a satisfactory description of its energy spectrum is still not available, and this is due to the fact that NiO is a strongly correlated electron system. Therefore, there is still need to understand the

theoretical predictions to facilitate a deeper knowledge of the characteristics and properties for this important material. This study therefore seeks to establish the properties that make NiO an important material in solar energy applications.

1.4 Objectives

1.4.1 General objective

The main objective of this research is to study the ground-state properties and optical properties of NiO.

1.4.2 Specific Objectives

a) To determine the structural properties of bulk rhombohedral (RHL) NiO, using LSDA and LSDA+U methods;

b) To determine the electronic and magnetic properties of bulk RHL NiO, using LSDA and LSDA+U methods;

c) To determine the optical properties of face centered cubic (fcc) NiO and RHL NiO, using the Green function and the dynamically screened interaction (GW) and the Bethe Salpeter Equation (BSE).

1.5 Significance and justification of the study

NiO is an attractive material due to its wide variations in physical properties related to electronic structure, optical and magnetic behaviours. It is a p-type semiconductor with wide band-gap energy [1–8], making NiO thin films have many applications in optics, electronics and solar energy depending on their absorption, reflectance and transmittance properties [3, 22].

The problem of understanding the properties of strongly correlated systems and especially TM, is one of the main challenges in condensed matter physics. In this case one has to go beyond DFT and employ more sophisticated treatment of electron-electron interactions. As such, one has to restrict the study to the most important orbitals so that the

many-electron interactions can be explicitly treated. For instance, the valence d electrons are the most relevant ones responsible for the properties of TM compounds, and a model Hamiltonian can be formulated involving only these electrons.

The treatment of correlation in these metal oxides remains also a major challenge and the O 2p - Ni 3d hybridization in the valence band has proved especially difficult to be predicted accurately. Therefore, it is still highly desirable to have more first-principles investigations of the electronic structure of NiO within different approaches to provide a better understanding of its properties. Such approaches include the LSDA+U, which works better for TM, and as a result gives a better prediction of the mechanical, electronic and magnetic properties. Since NiO has many applications in solar energy use, studying its excited states by analyzing the NiO optical properties, using GW and BSE methods becomes very critical.

CHAPTER TWO

LITERATURE REVIEW

2.1 Introduction

As stated in the chapter one, NiO is a TM oxide exhibiting wide variations in physical properties related to its electronic structure. Its optical and magnetic behaviours, in particular, form the basis of the enormous range of applications, and therefore, it has been the subject of extensive experimental and theoretical investigations for the past several years. In this chapter, some reviews on NiO which form an essential background in studying this material are given.

2.2 Experimental and theoretical studies

2.2.1 Structural studies

NiO crystallizes in the rock-salt (NaCl) structure with a lattice constant of 0.4168 nm [1, 5, 9] above T_N. Below T_N, NiO transforms to a rhombohedral distorted rock salt structure by a compression along the body diagonal direction with the rhombohedral angle α_{rh} of 60.08^0 or 33.557^0 [2, 10–12]. The various values of the lattice constant that have been obtained experimentally and theoretically include 4.176 Å [1], 4.1678 Å [9], 4.172 Å [5], 4.180 Å [23], 4.16 Å [24], for fcc NiO; 2.948 Å [10] and 8.47 Å [11] for fcc NiO. The bulk modulus has been determined by different workers and found to have the value of 202.2 GPa [23], 196 GPa [2], 184 GPa [25], 166.4 GPa [26], and 230.72 GPa calculated recently by Gillen and Robertson [11].

2.2.2 Electronic studies

The electronic properties of the NiO have been studied from both the experimental and theoretical points of view, where the material has long been studied as an insulating material. In a purely ionic picture of NiO, the Ni^{2+} ions have a partially filled d shell in a $3d^8$ ground-state configuration [6]. According to conventional band theory, this should result

in metallic behavior, yet NiO is a semiconductor with a wide band gap. DFT studies have been successfully applied to describe many details of electronic structure, magnetic coupling, and character of the band gap since a long time. However, it fails to describe the band structure of TM oxides as insulators and predicts them to be metals. LSDA studies predicted NiO to have a band gap of around 0.5 eV [7, 11, 17, 20, 27], which is narrower compared to the experimental results. Therefore, various computational methods have been applied to predict NiO energy band gap, and different results have been obtained as shown in Table 2.1. Various researchers have investigated the band structure of the bulk and surface of NiO using different methods, such as DFT [7, 11, 17, 20, 27], DFT+U [2, 19, 20, 23, 27–29] and GW [7, 30–32] methods.

Table 2.1: Calculated NiO energy band gap with different methods.

Method	Ref.	Band gap (eV)	Structure
LDA+U; U=4.6	[19]	2.7	Bulk; Cubic
LSDA+U; U=6.2	[20]	3	Cubic
LDA+U; U=5	[28]	2.6	Bulk; Cubic
LDA+U; U=5		2.1	Surface 001
LDA+U; U=5		0.8	Surface 111 p(2×2)
DFT+U ; U=7	[2]	3.8	Bulk; Rhombohedral
LSDA+U ; U=6.1	[29]	3.7	Bulk
LSDA+U; U=5.4	[27]	4.1	Bulk
MBJLDA	[17]	4.16	Bulk
LSDA+U ; U=6.2	[23]	4.04	Cubic; Surface 001
GGA(96)+U ; U=6.2		4.31	
GG(06)+U ; U=6.2		3.4	
GW	[7]	4.8	Bulk
Hybrid B3LYP	[33]	3.9	Bulk
sX-LDA	[11]	3.85; 4.1	Cubic
GW@LDA	[30]	5.5	Rhombohedral
GoWo@LDA+U; U=5.2	[31]	3.76	Rhombohedral
U+GW; U=4	[32]	3.99	Rhombohedral

From the projected density of states, some studies have predicted the conduction band of NiO and the upper edge of the valence band to be of the same character, i.e Ni 3d, making NiO to become a Mott-Hubbard insulator [6, 7, 17, 34]. However, the upper edge of the valence band was correctly predicted by some other authors [19, 20, 29, 30, 35, 36]

to be of the O 2p character and that NiO should therefore be classified as a charge-transfer insulator, as opposed to a Mott-Hubbard insulator.

2.2.3 Optical studies

Various methods have been used to prepare nickel oxide films in different experiments, including Sol gel spin coating [5, 9], Automated liquid flow deposition [37], Magnetron sputtering [4, 38], Electron beam evaporation [39], Thermal oxidation [13] and Chemical bath deposition [40], as shown in Table 2.2. Different methods like X-ray diffraction (XRD) [1, 3–5, 9, 24, 37–40], Scanning electron microscopy (SEM) [1, 3, 4, 9, 37, 38], Atomic force microscope (AFM) [39], Transmission electron microscope (TEM) [1, 3, 5], Photoluminescence (PL) and Energy dispersive X-ray (EDX) [3], Standard Critical Point model (SCP) [6], the Automated Liquid Flow Deposition Technique (ALFDT) [37] and Ultraviolet (UV) - visible (Vis) - near infrared (NIR) spectroscopies (UV-Vis [1, 3, 13, 39], UV-Vis-IR [9, 38] and UV-Vis-NIR [4, 5, 24, 40]) were used to analyze NiO properties.

In many experiments, the energy band gap was determined using UV-Vis-NIR spectrophotometers, and the gap was found to depend on the techniques of thin film preparation, thin film size and the temperature. Table 2.2 gives a review of some published data on the NiO optical energy band gap, the preparation techniques and the methods used to analyse the NiO thin-films microstructure and optical properties.

The NiO thin films properties were found to depend on the reflectance and transmittance properties of the films during their preparation [22]. The properties of NiO thin films depend also on substrate temperature as well as on the amount of oxygen during their fabrication, and a good transmittance was observed for the NiO films deposited at elevated temperature [38].

The spectral transmittance and reflectance of the NiO thin film samples showed that they are transparent with transmittance exceeding 80% within the spectral ranges between 300-2400 nm [24, 38, 40–42]. It was also found that a lower transmittance depends on the increase in the film thickness, with subsequent increase in absorption. The maximum absorbance for the thin films occurred within the UV region and from where, the absorbance

Table 2.2: Experimental NiO energy band gap.

Band gap (eV)	Ref.	NiO preparation techniques	Method used
3.8	[1]	Thermal decomposition	TEM, UV-Vis
3.32	[39]	Electron beam evaporation	UV-Vis
3.89 - 3.92	[3]	Cationic surfactant (CTAB)	PL, UV-Vis
3.65 - 3.82	[4]	DC reactive magnetron sputtering	SEM, UV-Vis-NIR
3.4 - 3.71	[38]	RF magnetron sputtering	SEM; UV-VIS-IR
3.47 - 3.86	[9]	Sol gel spin coating	SEM, UV-VIS-IR
3.35 - 3.73	[37]	Automated Liquid Flow Deposition	SEM, ALFDT
3.744 - 3.867	[5]	Sol-gel dip coating	TEM, UV-Vis-NIR
3.6	[13]	Thermal oxidation	UV-Vis
2.10 - 3.9	[40]	Chemical bath deposition	Absorption spectroscopy, UV-VIS-NIR
3.87	[6]	Verneuil (flame fusion)	SCP
3.17 - 3.83	[24]	Spray pyrolysis	UV-Vis-NIR

decreased with the wavelength towards the NIR region. The absorption coefficient tends to decrease exponentially as the wavelength increases whereas the reflectivity of thin films increases with increasing wavelength [5, 40].

2.2.4 Magnetic studies

Several theoretical and experimental studies have been carried out to understand the magnetic properties of NiO. Different magnetic ordering including antiferromagnetic type one (AF1) [11, 25], ferromagnetic (FM) [11, 43–46], non magnetic (NM) [25] and antiferromagnetic type two (AF2) [11, 25, 36] have been observed on NiO. In the AF2 case, Ni atoms have finite magnetic moments but the total magnetization is zero as the magnetic moments of Ni ion align ferromagnetically on every (111) plane and antiferromagnetically for adjacent planes [47, 48]. In the FM state all spin moments are aligned in one direction. The NiO AF2 ordering was predicted to be the most stable magnetic configuration followed by the FM state and then the AF1 one, which is consistent with experiments and other calculations [25].

The hybridization [23, 27] of the O 2p and Ni 3d states, i.e the covalent bonding between the Ni and O atoms, was observed to be stronger than the coupling of the d - d states

between nearest neighbouring Ni ions, and the opposite spin next nearest neighbours of Ni ions are energetically favoured and this makes the AF spin structure the ground state of NiO. Some theoretical calculations predicted NiO to have the magnetic moment values of 1.75 μ_B [2, 17], 2.00 μ_B [23] and 1.91 μ_B [27]. The experiments showed that the NiO magnetic moment value ranged between 1.7 μ_B and 1.9 μ_B [47].

CHAPTER THREE

THEORETICAL BACKGROUND

3.1 Introduction

One of the fundamental problems in condensed matter physics is the theoretical study of electronic properties. This is necessary to understand the behaviour of materials ranging from atoms, molecules, and nanostructures to complex materials. However, it is a very difficult problem in many-body theory to solve the Schrödinger equation for a system of N interacting electrons in the external coulombic field created by a collection of atomic nuclei (and may be some other external field). The exact solution can be known only in the case of the uniform electron gas, for atoms with a small number of electrons and for a few small molecules. Since electrons are governed by the laws of quantum mechanics, the many-electrons problem is, in principle, fully described by a Schrödinger equation [14, 49, 50].

3.2 Many body Schrödinger equation

The determination of the properties of a material from first principles, involves the solution of a quantum many-body interacting problem, over both the atomic nuclei and electron coordinates,

$$\hat{H}\Psi(\{R_I\},\{r_i,\sigma_i\}) = E\Psi(\{R_I\},\{r_i,\sigma_i\}). \tag{3.1}$$

whereby for a system containing M nuclei and N electrons the many-body wavefunction (Ψ) is a function of all the spatial coordinates of nuclei $(\{R_I\}, I = 1, ..., M)$ and spatial and spin coordinates of electrons $(\{r_i, \sigma_i\}), i = 1, ..., N$. The Hamiltonian $(\hat{H})$ is the sum of all possible interactions between electrons and nuclei. In atomic units (energy in Hartree and length in Bohr, $e^2 = m_i = \hbar = 1$, where e and m_i are electric charge and mass of an electron, respectively, and $\hbar$ is the Plank constant) [49], $\hat{H}$ can be expanded as

$$\hat{H} = -\sum_{i=1}^{N}\frac{\nabla_i^2}{2} - \sum_{I=1}^{M}\frac{\nabla_I^2}{2M_I} + \sum_{i=1}^{N}\sum_{j>i}^{N}\frac{1}{|r_i - r_j|} + \sum_{I=1}^{M}\sum_{J>J}^{M}\frac{Z_I Z_J}{|R_J - R_J|} - \sum_{i=1}^{N}\sum_{I=1}^{M}\frac{Z_I}{|r_i - R_I|}. \tag{3.2}$$

In Eq.(3.2), M_I is the mass of nucleus I and Z_I is the atomic number of nucleus I. The symbols ∇_i^2 and ∇_I^2 are the Laplacian operators. The first two terms in Eq. (3.2) represents the kinetic energies of all the electrons and nuclei, respectively, while the third and fourth terms, respectively, correspond to the Coulomb repulsion between electrons and between nuclei. The fifth term is the Coulomb attraction between electrons and nuclei.

The many-electrons Schrödinger equation, is generally believed capable of predicting and describing almost every phenomena experienced in everyday life. It is deceptively simple by its form but enormously complex to solve. The evaluation of physical quantities of interest with appropriate approximations is then required and desirable in order to reduce the complexity. The first important approximation is obtained by decoupling the dynamics of the electrons and the nuclei, which is known as Born-Oppenheimer approximation.

3.3 Born Oppenheimer approximation

The majority of the properties of a condensed matter system can be determined by investigating just the interactions of the valence (outer) electrons with the relatively slower-moving atomic ionic cores (nuclei plus core electrons) and the interactions of the valence electrons among themselves. In the Born–Oppenheimer, or adiabatic approximation for electronic properties, nuclei can be treated as classical particles and can be considered as static with respect to quantum particle electrons. Then for any given nuclear configurations, the electrons are assumed to remain in their instantaneous ground state. As a result, the second term in Eq. (3.2) can be neglected and the fourth term, the repulsion between nuclei, can be treated as a constant for a fixed configuration of the nuclei. The remaining terms in Eq. (3.2) are called the electronic Hamiltonian (H_e) [49, 50],

$$\hat{H}_e = -\sum_{i=1}^{N} \frac{\nabla_i^2}{2} + \sum_{i=1}^{N}\sum_{j>i}^{N} \frac{1}{|r_i - r_j|} - \sum_{i=1}^{N}\sum_{I=1}^{M} \frac{Z_I}{|r_i - R_I|}. \tag{3.3}$$

The Schrödinger equation involving the electronic Hamiltonian $\hat{H}_e$ becomes

$$\hat{H}_e \Psi_e(\{R_I\}, \{r_i, \sigma_i\}) = E_e \Psi_e(\{R_I\}, \{r_i, \sigma_i\}). \tag{3.4}$$

Furthermore, for simplicity, the electronic spatial and spin coordinates $(\{r_i, \sigma_i\})$ are put together into one variable and Eq. (3.3) is rewritten as

$$\hat{H}_e \Psi_e(\{R_I\}, \{X_i\}) = E_e \Psi_e(\{R_I\}, \{X_i\}). \tag{3.5}$$

3.4 Wave function based method

The eigenfunction of a quantum mechanical operator depends on the coordinates upon which the operator acts. The particular operator that corresponds to the total energy of the system is called the Hamiltonian operator. The eigenfunctions of this particular operator are then called wave functions.

3.4.1 Hartree approximation

The Hartree method is useful as an introduction to the solution of the many-particle system and to the concepts of self-consistency and of the self-consistent-field. In Eq. (3.3) the kinetic energy term and the nucleus-electron interaction term are sums of single-particle operators, each of which act on a single electronic coordinate. The electron-electron interaction term on the other hand is a pair interaction and acts on pairs of electrons. To facilitate the upcoming mathematics, let's make the following definition

$$\hat{H}_e = \sum_i \hat{h}_1(\vec{x}_i) + \frac{1}{2} \sum_{i \neq j} \hat{h}_2(\vec{x}_i, \vec{x}_j), \tag{3.6}$$

where $\vec{x}_i$ is now a generalized coordinate that includes spatial as well as spin degrees of freedom. The Schrodinger equation can now be written as

$$\left(\sum_i \hat{h}_1(\vec{x}_i) + \frac{1}{2} \sum_{i \neq j} \hat{h}_2(\vec{x}_i, \vec{x}_j)\right) \Psi(r_1, r_2, ..., r_N) = E \Psi(r_1, r_2, ..., r_N). \tag{3.7}$$

The Hartree method is a variational, wavefunction-based approach. Although it is a many-body technique, the approach followed is that of a single-particle picture, i.e the electrons are considered as occupying single-particle orbitals making up the wavefunction. To apply the variational principle, we assume that the trial wavefunction is built from

these single particle orbitals. Let us suppose that we have n arbitrary one-particle states $\psi(r_1), \psi(r_2), ..., \psi(r_N)$. We should choose them as an orthonormal set, since this will make the calculation of expectation values easier. The simplest wavefunction that can be formed is their direct product

$$\Psi(r_1, r_2, ..., r_N) = \psi(r_1)\psi(r_2)...\psi(r_N). \tag{3.8}$$

This is the Hartree approximation and it is a straightforward task to calculate the variational lowest energy. Each of the functions in Eq. (3.8) is normalized to unity. If we calculate the expectation value of H in this state, we obtain [14]

$$< H >= \sum_{i=1}^{N} \int dr_i^3 \; \psi^*(r_i) \; (\frac{-\nabla_i^2}{2} - \frac{Z}{r_i}) \; \psi(r_i) + \sum_{i>j} \sum_{j} \frac{|\psi_i(r_i)|^2 \;\; |\psi_j(r_j)|^2}{|r_i - r_j|}. \tag{3.9}$$

The procedure of the variational principle is to pick the $\psi_i(r_i)$ such that $< H >$ is a minimum and then Eq. (3.9) leads to the condition that

$$[-\frac{\nabla_i^2}{2} - \frac{Z}{r_i} + V_H]\psi_i(r_i) = E_j\psi_i(r_i), \tag{3.10}$$

where V_H is the Hartree potential

$$V_H(r_i) = \sum_{i \neq j} \int dr_j^3 \; \frac{|\psi_j(r_j)|^2}{|r_i - r_j|}. \tag{3.11}$$

3.4.2 Hartree-Fock Approximation

The Hartree-Fock (HF) method treats electron-electron interactions at a mean field level, with the Hartree and exchange interactions. The simple product of the wavefunctions in Eq. (3.8) does not satisfy the principle of indistinguishability, and fails to satisfy antisymmetry, which states that a fermion wavefunction changes sign under odd permutations of the electronic variables. It is however possible to build an antisymmetric solution by introducing the following determinant, called Slater determinant [14, 49]:

$$\Psi(r_1, r_2, ..., r_N) = \frac{1}{\sqrt{N!}} \begin{vmatrix} \psi_1(r_1) & \psi_1(r_2) & ... & \psi_1(r_N) \\ \psi_2(r_1) & \psi_2(r_2) & ... & \psi_2(r_N) \\ \vdots & \vdots & \ddots & \vdots \\ \psi_N(r_1) & \psi_N(r_2) & ... & \psi_N(r_N) \end{vmatrix}. \tag{3.12}$$

The exchange of two particles is equivalent to the exchange of two columns, which induces, due to the known properties of determinants, a change of sign. Note that if two rows are equal, the determinant is zero. Therefore, all ψ_i must be different. This demonstrates Pauli's exclusion principle where two (or more) identical fermions cannot occupy the same state. The HF potentials can be derived from minimizing the total ground-state energy, and Eq.(3.12) leads directly to the HF mean-field, self-consistent field equation :

$$[-\frac{\nabla_i^2}{2} - \frac{Z}{r_i} + V_H + V_i^x]\ \psi_i(r_i) = E_j \psi_i(r_i), \tag{3.13}$$

where V_i^x is a non-local potential, called exchange potential due to the anti-symmetric nature of the wavefunction,(Eq. 3.14):

$$V_i^x(x_i)\ \psi_i(r_i) = [\sum_{j=1}^{N} \int \psi_i^*(r_j)\ \frac{-1}{|r_i - r_j|}\ \psi_j(r_i)\ dr_j]\ \psi_i(r_i). \tag{3.14}$$

The HF equation, (3.13), represents the one-electron approximation for interacting fermions which includes the anti-symmetry of the wavefunction or exchange interaction. This HF method has been implemented on periodic systems, including bulk and surface crystalline materials [51]. In the HF equation, the non local potential causes the problems. One of the problems is that it provides an inaccurate description of the spatial separation of the electrons as it would be in a complete many-electron interaction. This missing part is widely designated as electron correlation. The difference between the ground state HF energy and the exact ground state energy is used as a standard definition of the correlation energy in quantum chemistry [49]. Going beyond the HF formalism, the HF method is improved by taking account of the electron correlation.

3.5 Density Functional Theory (DFT)

Density functional theory (DFT) is one of the most frequently used computational tools for studying and predicting the properties of materials. It is a ground-state theory in which the emphasis is on the charge density as the relevant physical quantity. DFT has proved to be highly successful in describing structural and electronic properties in a vast class of materials. For these reasons DFT has become a common tool in first-principle calculations aimed at describing and predicting the properties of molecular and condensed matter systems [14, 15, 19, 52].

3.5.1 The Hohenberg-Kohn Theorem

Suppose a system of N interacting (spinless) electrons is under an external potential $V(r)$, usually the Coulomb potential of the nuclei. If the system has a nondegenerate ground state, it is obvious that there is only one ground-state charge density $n(r)$ that corresponds to a given $V(r)$. Hohenberg and Kohn demonstrated that there is only one external potential $V(r)$ that yields a given ground-state charge density $n(r)$:

$$n(r) = N \int |\Psi(r_1, r_2, ..., r_N)|^2 dr_1 dr_2 ... dr_N, \tag{3.15}$$

where Ψ is the ground state wavefunction. The consequence of the Hohenberg and Kohn theorem is that the ground state energy E is also uniquely determined by the ground-state charge density, (Eq. 3.16):

$$E[n(r)] = F[n(r)] + \int n(r)\, V(r) dr, \tag{3.16}$$

where the internal energy $F[n(r)]$ is a universal functional of the charge density $n(r)$ (and not of $V(r)$). In this way, DFT exactly reduces the N-body problem to the determination of a 3-dimensional function $n(r)$ which minimizes a functional $E[n(r)]$.

3.5.2 Kohn-Sham Equations

In 1965, Kohn and Sham (KS) [53] reformulated the problem in a more familiar form and opened the way to practical applications of DFT. The system of interacting electrons is mapped on to an auxiliary system of non-interacting electrons having the same ground state charge density $n(r)$. For a system of non-interacting electrons, the charge density is represented as a sum over one-electron orbitals (the KS orbitals) $\psi_i(r_i)$:

$$n(r) = \sum_{i}^{N} |\psi_i(r)|^2, \tag{3.17}$$

where N is the number of electrons. The KS orbitals are the solutions of the Schrödinger equation [53, 54]:

$$[-\frac{\nabla^2}{2} + V_H(r) + V_{xc}(r) + V(r)]\psi_i(r) = (-\frac{\nabla^2}{2} + V_{KS}(r))\ \psi_i(r) = E_i\ \psi_i(r), \tag{3.18}$$

where the energy functional E, defined as (Eq. 3.19):

$$E_{tot}[n(r)] = T_0[n(r)] + E_{Coul}[n(r)] + E_{xc}[n(r)] + E_{ext}[n(r)], \tag{3.19}$$

is assumed to hold for an arbitrary density $n(r)$. $T_0(n)$ is the kinetic energy for the antisymmetrized product wave function (independent electrons), E_{Coul} is the classical Coulomb energy term, $E_{ext}(n)$is potential energy between electrons and ions, and $E_{xc}(n)$ is the exchange correlation energy and includes all corrections in these quantities due to electron correlation.

3.5.3 Exchange-correlation energy

The exchange-correlation energy $E_{xc}(n)$ accounts for the difference between the exact ground-state energy and the energy calculated in a HF approximation and using the non-interacting kinetic energy;

$$E_{xc}(n) = T(n) - T_0(n) + U_{xc}. \tag{3.20}$$

$T(n)$ and $T_0(n)$ are exact and non-interacting kinetic energy functionals, respectively, whereas U_{xc} is the interaction of the electrons with their own exchange-correlation hole. The exchange-correlation energy can also be expressed in the form of a classical electrostatic interaction between the electron density $n(r)$, and the hole density $n_{xc}(r, r')$,

$$E_{xc}[n(r)] = \frac{1}{2} \int \int dr\, dr' \, \frac{n(r)\, n_{xc}\,(r, r')}{|r - r'|}. \tag{3.21}$$

Approximations are sought for $E'_{xc}[n]$, which though it contains also contributions from the kinetic energy, it is usually just called **Exchange-correlation functional** and written as $E_{xc}[n]$.

The following subsections explain some typical approximations for the exchange- correlation functional that are commonly employed in practical DFT codes.

3.5.4 Local density approximation (LDA)

The local density approximation (LDA) is the basis of all approximate exchange-correlation functionals. At the centre of this model is the idea of uniform electron gas. This is a system in which electrons move on a positive background charge distribution such that the total ensemble is neutral. The effects of exchange and correlation are local in character, and in LDA, the exchange-correlation energy is assumed to be simply an integral over all space with the exchange-correlation energy density at each point, and assumed to be the same as in a homogeneous electron gas with that density [15, 47, 49, 50, 55],

$$E_{xc}^{LDA}[n(r)] = \int dr\, \epsilon_{xc}[n(r)]\, n(r), \tag{3.22}$$

In this case $\epsilon_{xc}[n(r)]$ is the the exchange-correlation energy per electron in a homogeneous electron gas of the density, $n(r)$. This energy per particle is weighted with the probability that there is an electron at this position, and usually, represents the number of electrons per unit volume. The exchange-correlation energy $\epsilon_{xc}[n(r)]$ consists of two components: the exchange energy per electron $\epsilon_x[n(r)]$ which represents the exchange energy of an

electron in a uniform gas of a density $n(r)$, and the correlation energy $\epsilon_c[n(r)]$,

$$\epsilon_{xc}[n(r)] = \epsilon_x[n(r)] + \epsilon_c[n(r)]. \tag{3.23}$$

The exchange-correlation potential is obtained from the exchange-correlation energy functional and is normally expressed as [49, 50],

$$V_{xc}^{LDA}(r) = \frac{\delta E_{xc}^{LDA}[n(r)]}{\delta n(r)}. \tag{3.24}$$

3.5.5 Local spin density approximation (LSDA)

The extension of density functionals to spin-polarized systems is straightforward for exchange, where the exact spin-scaling is known, but for correlation further approximations must be employed. A spin polarized system in DFT employs two spin-densities, $n^{\uparrow}$ and $n^{\downarrow}$, the densities of spin up and spin down electrons, respectively, with

$$n(r) = n^{\uparrow}(r) + n^{\downarrow}(r), \tag{3.25}$$

and the form of the local-spin-density approximation (LSDA) is written as [56]:

$$\begin{aligned} E_{xc}^{LSDA}[n^{\uparrow}, n^{\downarrow}] &= \int dr\ \epsilon_{xc}[n^{\uparrow}(r), n^{\downarrow}(r)]\ n(r) \\ &= \int dr\ n(r)\ \{\epsilon_x[n^{\uparrow}(r), n^{\downarrow}(r)] + \epsilon_c[n^{\uparrow}(r), n^{\downarrow}(r)]\} \\ &= \int dr\ n(r)\ \{\epsilon_x[n, \xi] + \epsilon_c[n, \xi]\}. \end{aligned} \tag{3.26}$$

The fractional spin polarization $\xi(r)$ is defined by [56, 57]

$$\xi(r) = \frac{n^{\uparrow}(r) - n^{\downarrow}(r)}{n(r)}, \tag{3.27}$$

In LSDA, $E_{xc}^{LSDA}[n]$ is the usual local spin-density functional of the total electron spin densities $n^{\sigma}(r)$ with spin $\sigma = \uparrow, \downarrow$.

The $\delta E_{xc}^{LSDA}[n]$ can be written as [49, 50],

$$\delta E_{xc}^{LSDA}[n] = \sum_{\sigma} \int dr[\epsilon_{xc} + n\frac{\partial \epsilon_{xc}}{\partial n^{\sigma}}]\, \delta n(r,\sigma), \tag{3.28}$$

The exchange-correlation potential becomes

$$V_{xc}^{\sigma} = \frac{\delta E_{xc}}{\delta n^{\sigma}(r)} = [\epsilon_{xc} + n\, \frac{\partial \epsilon_{xc}}{\partial n^{\sigma}}]_{r,\sigma}. \tag{3.29}$$

The range of the effects of exchange and correlation is short in solids. The success of the LSDA is partly caused by the fact that the exchange-correlation hole is reproduced by the LDA.

3.5.6 Generalized Gradient Approximation (GGA)

An improvement in the accuracy provided by the LDA can be obtained by using the Generalized Gradient Approximation (GGA) functionals. In GGA a functional form is adopted to ensure the normalisation condition and the exchange hole is negative definite. These depend both on the value of the charge density and also on its gradient, but retains the analytic properties of the exchange-correlation hole inherent in the LDA [58].

$$E_{xc}^{GGA} = \int dr\; n(r)\epsilon_{xc}[n(r), \nabla n(r)]. \tag{3.30}$$

GGA functionals are often called "semi-local" functionals due to their dependence on $\nabla n(r)$. Those functionals are known to satisfy some known conditions that the exact functional should satisfy as well. For many properties, for example geometries and ground state energies of molecules and solids, GGA can yield better results. Especially for covalent bonds and weakly bonded systems, GGA is far superior to LDA. It yields much better atomic energies and binding energies, at a modest additional computational cost. LDA, LSDA and GGA approximations, predict correctly for a lot of systems' ground states properties such as ground state energy, forces acting on atoms, charge density, band structure and density of states, as well as vibrational properties. However, they are not valid

for excited states and fail to predict the properties of some other materials especially for transition metal oxides or strongly correlated systems, where the band gaps are always underestimated [57, 59, 60].

3.5.7 DFT+U Approximation

DFT+U also known as LDA+U, or sometimes GGA+U, is a method used to describe strongly correlated electron systems especially in transition metals and transition metal oxides. The first expression of the LDA+U approach was formulated in 1997 by Anisimov, *et al.*, [18]. Most of the currently available exchange-correlation functionals which include the LSDA and GGA functionals are not successful in describing the exchange-correlation energy of a system with a strong tendency of electron localization and interaction. The origin of the failure of the LSDA in strongly correlated oxides (transition metal oxides, rare-earth compounds) is known to be associated with an inadequate description of the strong Coulomb repulsion between 3d and or 4f electrons localized on metal ions.

The LDA and its extensions underestimate local magnetic moments and the tendency to favour high-spin ground-states in such materials, and the insulating gap in cases where it is related to electron localization. Underestimation of the gap in the LSDA and GGA due to the absence of the derivative discontinuity with respect to orbital occupancy in the exact exchange-correlation functional, may be confounded by an underestimation of the exchange splitting induced by local magnetic moments. Thus, it is desirable to incorporate the on-site Coulomb interaction term into the exchange-correlation functional.

The DFT+U correction term is usually thought to be an explicit mean-field treatment of the exchange-correlation energy contributed by the correlated sites, within the Hubbard model. DFT+U includes also the double-counting correction, to take into account that contribution which is already included in the LDA term. The Hubbard U term is the effective interaction parameter characterizing the on-site Coulomb repulsion between 3d electrons. The LSDA+U functional can be expressed in terms of the density matrix as [20, 59]:

$$E_{xc}^{LSDA+U} = E_{xc}^{LSDA} + \frac{U-J}{2}\sum_{\sigma}[\sum_{m} n_{mm}^{\sigma} - \sum_{mm'} n_{mm'}^{\sigma}\, n_{m'm}^{\sigma}], \tag{3.31}$$

where J is the spin-spin exchange interaction parameter, $n^{\sigma}_{mm'}$ is the (mm') component of the density matrix of d electrons with the spin configuration σ and the orbital magnetic quantum numbers of m and m'. Therefore, the mm' matrix element of the (one-electron) LSDA+U exchange-correlation potential [20, 49, 50] can be obtained from Eq. (3.31);

$$V^{\sigma}_{mm'} = \frac{\delta E^{LSDA+U}}{\delta n^{\sigma}_{m'm}} = \frac{\delta E^{LSDA}}{\delta n^{\sigma}_{m'm}} + (U - J)[\frac{1}{2}\delta_{mm'} - n^{\sigma}_{mm'}]. \tag{3.32}$$

In 1998, an important contribution was given by Pickett, *et al.*, [21] who, while slightly refining the functionals, introduced a linear response technique for calculating the Hubbard parameters. U and J are determined from the relations,

$$U = \epsilon^{\uparrow}_{3d}\,(\frac{\bar{n}}{2} + \frac{1}{2}\,,\ \frac{\bar{n}}{2}) - \epsilon^{\uparrow}_{3d}\,(\frac{\bar{n}}{2} + \frac{1}{2}\,,\ \frac{\bar{n}}{2} - 1), \tag{3.33}$$

in which the d occupation differs by unity around a mean polarization of unity, and

$$J = \epsilon^{\uparrow}_{3d}\,(\frac{\bar{n}}{2} + \frac{1}{2}\,,\ \frac{\bar{n}}{2} - \frac{1}{2}) - \epsilon^{\downarrow}_{3d}\,(\frac{\bar{n}}{2} + \frac{1}{2}\,,\ \frac{\bar{n}}{2} - \frac{1}{2}), \tag{3.34}$$

which is a difference between up and down eigenvalues for unit spin polarization. The term $\bar{n}$ is the LDA charge density value and $\epsilon^{\uparrow}_{3d}\,(n^{\uparrow}, n^{\downarrow})$, $\epsilon^{\downarrow}_{3d}\,(n^{\uparrow}, n^{\downarrow})$ are spin-up and spin-down 3d eigenvalues, respectively, for occupancies $n^{\uparrow}$ and $n^{\downarrow}$. In practice, the U and J terms are often combined by redefining U as an effective value, $U_{eff} = U - J$ and setting $J = 0$ [20]. Consequently, all values for U used in this study are considered to be effective values.

3.6 Many-body perturbation theory (MBPT)

The closed set of five integrodifferential of Hedin's equations [61], for the self-energy (Σ), the Dyson equation (G), the vertex function (Γ), the screened (W) and the bare (v) Coulomb interaction, and the polarizability (P), are used in Many body perturbation theory (MBPT).

$$\Sigma(1,2) = i \int d(3,4)\, G(1,3)\, W(1,4)\, \Gamma(3,2,4), \tag{3.35}$$

$$G(1,2) = G_0(1,2) + \int d(3,4)\, G_0(1,3)\, \Sigma(3,4)\, G(4,2), \tag{3.36}$$

$$\Gamma(1,2,3) = \delta(1,2)\delta(2,3) + \int d(4,5,6,7)\, \frac{\delta\Sigma(1,2)}{\delta G(4,5)}\, G(4,6)\, G(7,5)\, \Gamma(6,7,3), \tag{3.37}$$

$$P(1,2) = -i \int d(3,4)\, G(1,3)\, \Gamma(3,4,2)\, G(4,1), \tag{3.38}$$

$$W(1,2) = v(1,2) + \int d(3,4)\, v(1,3)\, P(3,4)\, W(4,2). \tag{3.39}$$

In Eqs. (3.35-3.39), we adopted the short-hand form $1 \equiv (r_1, \sigma_1, t)$ to denote a triple of space, spin, and time variables. Accordingly, $\int d(1)$ is a shorthand notation for the integration in all three variables of the triple. To simplify the notations, the Hedin's equations (3.35-3.39), are represented by Hedin's wheel or Hedin's pentagon shown in Figure 3.1, and can be rewritten as,

$$\Sigma = iGW\Gamma, \tag{3.40}$$

$$G = G_0 + G_0\Sigma G, \tag{3.41}$$

$$\Gamma(1,2,3) = 1 + \frac{\delta\Sigma}{\delta G}\, G\, G\, \Gamma, \tag{3.42}$$

$$P = -i\, G\, \Gamma\, G, \tag{3.43}$$

$$W = v + v\, P\, W. \tag{3.44}$$

The Dyson equation links the noninteracting system with Green's function (Go) to the fully interacting one (G), via the self-energy Σ. It can be rewritten in the form of a geometric series by subsequently replacing G on the right-hand side by $G_0 + G_0\Sigma G$ which

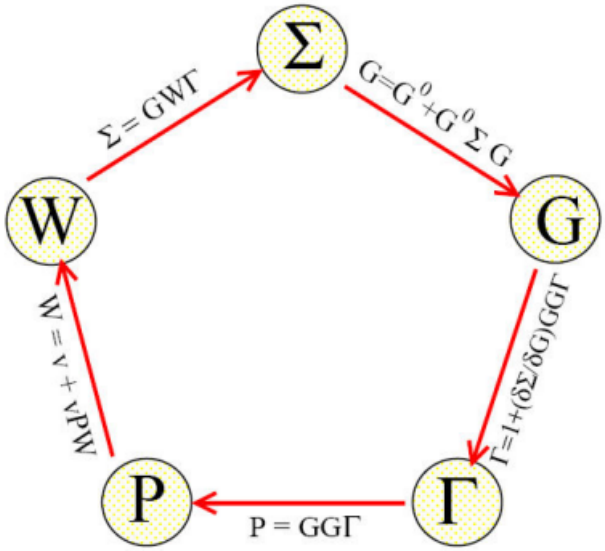

Figure 3.1: Hedin's wheel [61].

may be written symbolically as [62]:

$$G = G_0 + G_0\Sigma G_0 + G_0\Sigma G_0\Sigma G_0 + G_0\Sigma G_0\Sigma G_0 G_0\Sigma G_0 + \ldots \tag{3.45}$$

This equation (3.45) is a typical equation of scattering theory, where the different terms of the geometric series describe single, double, triple, etc., scattering processes; these are the exchange interaction, the creation of an electron-hole pair, and finally the creation of a pair that itself creates another pair. The scattering potential (Σ) is given by the sum of all single scattering processes. In order to obtain the complete Green function, we have to sum over all multiple scattering processes.

3.6.1 Green function and dynamically screened coulomb interaction (GW) approximation

The GW approximation, is based on the many-body perturbation theory at the *ab initio* level. In order to solve the Hedin's equations, one of the possible strategies could be to start from the top of the pentagon, Figure 3.1, with $\Sigma = 0$, and the 1 particle Green function reduces to G_0. The vertex function, [Eq. (3.42)], is approximated to unity $(\Gamma = 1)$ and the polarizability and the Self-energy are then rewritten:

$$P = iGG, \tag{3.46}$$

$$\Sigma = iGW. \tag{3.47}$$

Equation (3.47) gives the name of the GW approximation. In integrodifferential form [30, 31], the self energy and the dynamically screened interaction are given by:

$$\Sigma(r, r', \omega) = \frac{i}{2\pi} \int G(r, r', \omega + \omega') d\omega, \tag{3.48}$$

$$W(r, r', \omega) = \int \varepsilon^{-1}\,(r, r'', \omega + \omega')\; v(r'' - r')\; d^3 r'', \tag{3.49}$$

where G is the full interacting Green's function, W is the dynamically screened Coulomb interaction, within the random phase approximation (RPA) and is described by the inverse dielectric matrix ε^{-1} and the bare Coulomb potential v. In short notation, Eq. (3.49), can be rewritten as :

$$W = \varepsilon^{-1} v. \tag{3.50}$$

The dynamically screened interaction $W(r, r', \omega)$ is the effective potential at r' induced by a quasiparticle at r, as shown in Figure 3.2. The Coulomb potential of the electron repels other electrons in its neighbourhood and thus gives rise to the formation of an exchange and correlation hole, whose effective positive charge density $n_{ind}(r, r'', \omega)$ screens the bare Coulomb potential $v(r, r')$. The formation of the Coulomb hole around an electron at r,

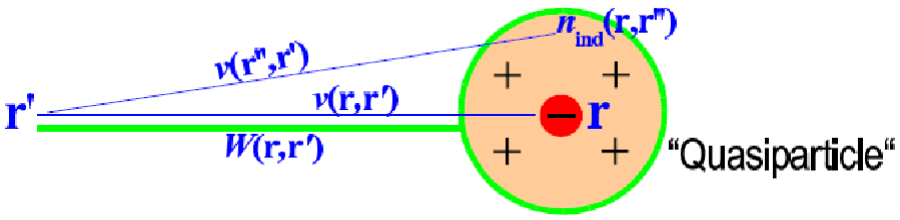

Figure 3.2: Formation of quasiparticle [62].

screens its Coulomb potential v. The screened interaction W takes into account the combined potentials of the bare electron and its screening cloud charge density $n_{ind}(r, r'', \omega)$, and the ensemble of the electron and its polarization cloud is called quasiparticle.

The total perturbation V_{tot} acting on the electronic system is given by the sum of the external perturbation applied on the sample and the induced perturbation.

$$V_{tot} = V_{ext} + V_{ind}. \tag{3.51}$$

The induced charge is given by

$$n_{ind} = P\, V_{tot} = \chi\, V_{ext}, \tag{3.52}$$

where P is the irreducible polarizability and χ is the reducible polarizability, also called the response function. The response function measures the change in the electronic density induced by the external applied potential. The microscopic (symmetric) dielectric function links the longitudinal component of an external field (i.e. the part polarized along the propagation wave vector q) to the longitudinal component of the total electric field by:

$$\varepsilon(q,\omega) = \frac{\delta V_{ext}}{\delta V_{tot}} = 1 - vP, \tag{3.53}$$

$$\varepsilon^{-1}(q,\omega) = \frac{\delta V_{tot}}{\delta V_{ext}} = 1 + v\chi. \tag{3.54}$$

Substituting Eq. (3.50) in Eq. (3.44), also yields the dielectric function given by Eq. (3.53). The evaluation of the response function and the irreducible polarizability makes it possible to get the microscopic dielectric function and its macroscopic dynamical dielectric function, which gives the optical spectra [16, 63].

$$\varepsilon_M(\omega) = \lim_{q\to 0} \frac{1}{\varepsilon(q,\omega)^{-1}}. \tag{3.55}$$

The spectral function of the absorption energy $(Abs(\omega))$ and electron energy loss $(Eel(\omega))$ are obtained from the imaginary part of the macroscopic dynamical dielectric function [30].

$$Abs(\omega) = \lim_{q\to 0} Im\, \varepsilon_M(\omega), \tag{3.56}$$

$$Eel(\omega) = \lim_{q \to 0} \; Im \; \frac{1}{\varepsilon_M(\omega)}. \tag{3.57}$$

3.6.2 Bethe Salpeter Equation - BSE

The BSE is used to treat excitonic effects introduced by using the electron–hole (e–h) Green's function L. It can be obtained from Hedin's equations, (Eqs. 3.40-3.42), and this can be written as,

$$L = L_0 + L_0 \left(v + i\frac{\delta\Sigma}{\delta G}\right) L. \tag{3.58}$$

Substituting the self energy by the Eq. (3.47) in Eq. (3.58) gives,

$$L = L_0 + L_0 \left(v - \frac{\delta GW}{\delta G}\right) L = L_0 + L_0 \left[v - \left(W + G\,\frac{\delta W}{\delta G}\right)\right] L. \tag{3.59}$$

The variation of the screened Coulomb interaction (W) with respect to the Dyson equation (G) tends to zero, thus Eq. (3.59) is written as,

$$L = L_0 + L_0 \left(v - W\right) L. \tag{3.60}$$

Equation (3.60) is known as the Bethe Salpeter Equation and describes the (coupled) propagation of two particles, namely the electron and the hole.

CHAPTER FOUR

METHODOLOGY

4.1 Introduction

In this study, the calculations on the NiO ground state properties were done using Quantum-ESPRESSO package [15], which is an integrated suite of computer codes for electronic-structure calculations and materials modeling, based on density functional theory (DFT), plane waves and pseudopotentials (norm-conserving, ultrasoft, and projector augmented wave). Quantum-ESPRESSO stands for Quantum opEn Source Package for Research in Electronic Structure, Simulation, and Optimization. In this work, it was used for the structural optimizations and for description of the NiO ground state. The optical properties were studied with *Yambo* code [16] which is an *ab initio* code for calculating quasiparticle energies and optical properties of electronic systems within the framework of many-body perturbation theory and time-dependent density functional theory.

4.2 DFT and DFT+U formalism

The major problem in solving the quantum many body problem described by the Hamiltonian given in Section 3.2, is the interaction between the electrons, which are identical Fermionic particles. For the purpose of calculating ground-state properties of the system, this complex many-body problem is reduced to solving the simpler problem of a single non-interacting electron moving in an effective field. In DFT [15], the ground state energy of a system is obtained from the ground state electron density, as it reformulates the total energy in terms of a functional of the charge density of the system, as shown in Eq. (3.16). A number of successful approximations, discussed in Section 3.5 including the LDA, GGA, LSDA and LSDA+U, have allowed practical and quantitatively accurate calculations for ground-state properties to be made using the DFT approach.

4.2.1 Solving self-consistency Kohn-Sham equation

In the Kohn-Sham (KS) approach, the electron charge density, and hence the total energy, may be obtained by solving an associated system of noninteracting electrons with the same charge density as the interacting system [53]. Within the KS scheme, the charge density n(r), can be expressed exactly in terms of sums over single-particle orbitals, as shown by Eq. (3.17). Therefore, KS equation has to be solved iteratively until a self- consistent solution is reached, and in practical calculations, the basic approximation lies in the construction of the energy functional itself [15, 53]. The schematic diagram of the procedure is shown in Figure 4.1.

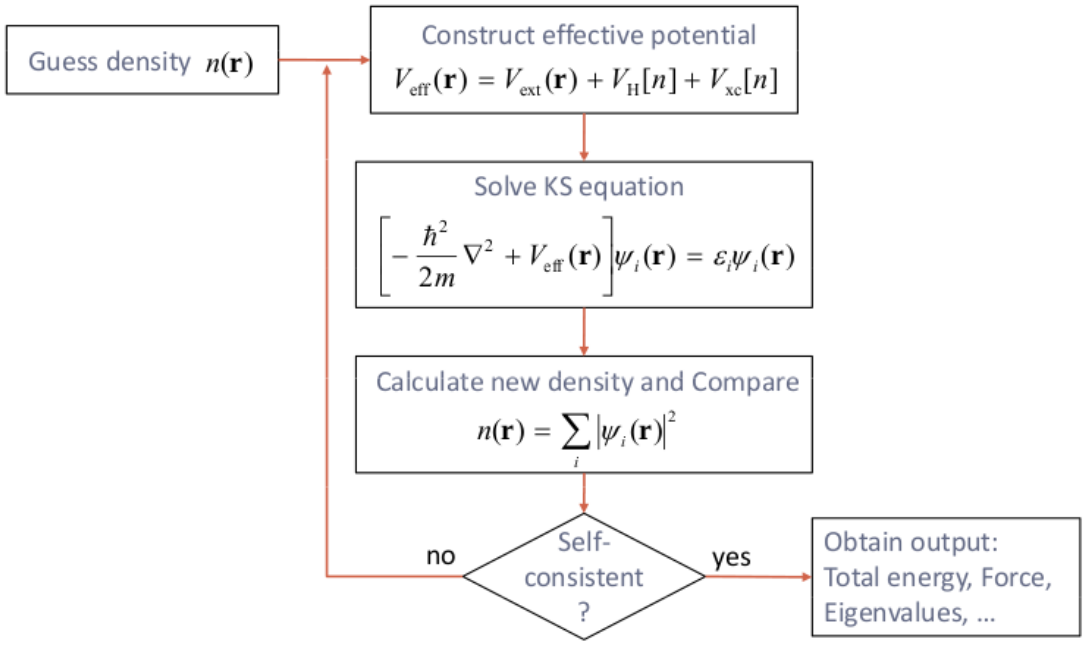

Figure 4.1: Schematic representation of the self-consistent loop for the solution of KS equation.

The wave functions are constructed from atomic positions and the pseudopotentials, and from these wave functions, an initial effective potential is constructed. Then the KS Hamiltonian is diagonalized to yield a new set of wave functions and eigenvalues. The process is repeated until the wave functions are below a specified convergence criteria. If the convergence is reached, then the total energy and the forces are calculated [14, 15].

4.2.2 Structure optimization

The NiO ground states properties were calculated using LSDA and LSDA+U. The Hubbard values of 5.4 eV [27], 6.2 eV [23], 7.3 eV [64] and 8 eV [18] determined previously by other workers with Linear combination of atomic orbitals (LCAO), Full potential linearized augmented plane wave (FLAPW), Linearized augmented plane wave (LAPW) and Linear muffin-tin orbital (LMTO) methods, respectively, were used. To investigate what is happening beyond U term of 8 eV, the Hubbard values of 8.5 eV, 9 eV, 9.5 eV, 10 eV and 12 eV, taken randomly, were used in order to investigate the NiO properties. The optimization results shown in Appendix A, of the k-points, the plane wave energy cutoff of the wave function (ecutwfc) and the lattice parameter were carried out using a RHL primitive unit cell. The T_N of NiO is 523 K and it has a cubic rock salt structure with a lattice constant of a_0 = 4.168 Å= 7.877 a.u above T_N as seen previously in Section 2.2.1. Below T_N, NiO transforms to a RHL distorted rock salt structure by a compression along the body diagonal direction with the RHL angle α_{rh} of 60.08^0 or 33.557^0 as shown in Figures 4.2 - 4.4.

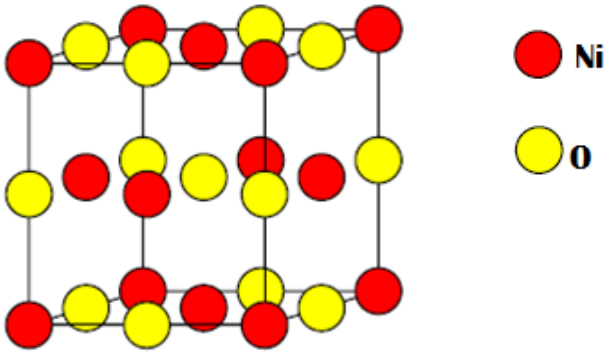

Figure 4.2: Face centered cubic structure of NiO.

The lattice parameters of 5.5699 a.u and 9.6475 a.u, of RHL NiO with α_{rh} = 60.08^0 and RHL NiO with α_{rh} = 33.557^0, respectively, were used to optimize the k-points and the plane wave cut off energies (ecutwfc). In this study, the ground-state properties were investigated for the bulk RHL NiO structure in its AF state, because it was found to have the lowest energy [11, 25, 36]. The NiO was modeled by a RHL unit cell containing two Ni and two O atoms. The calculations were done by assuming the two Ni atoms had opposite starting magnetization, in order to consider its AF state. The NiO atoms were allowed to

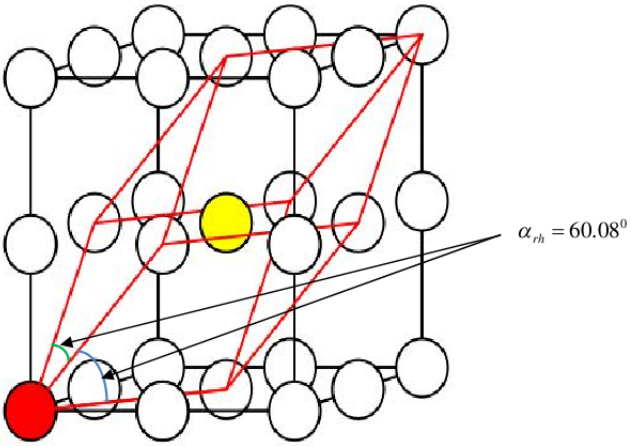

Figure 4.3: Transformation of fcc NiO into RHL NiO with α_{rh} = 60.08^0.

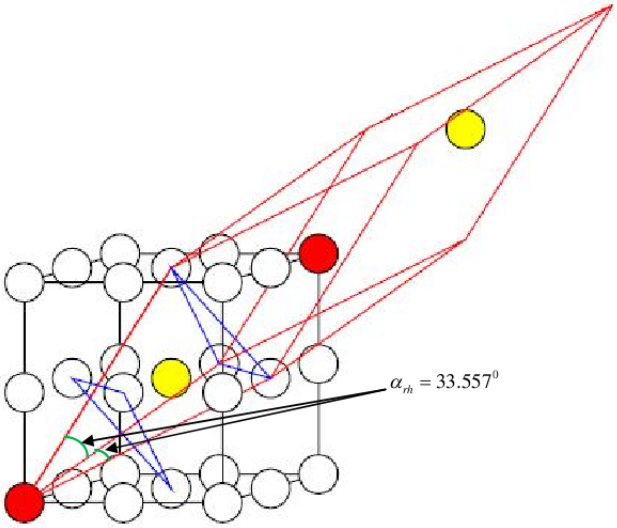

Figure 4.4: Transformation of fcc NiO into RHL NiO with α_{rh} = 33.557^0.

relax in x, y and z directions until the systems achieved the minimum energy according to some set convergence criteria and the corresponding relaxed atomic positions were then used in all subsequent calculations.

K-points were varied from a $2 \times 2 \times 2$ grid to higher values of $20 \times 20 \times 20$. The plane wave cut off energy was fixed at 30 Ry to make the calculations less computationally expensive during the test runs. The values of minimum energies obtained with respect to the corresponding k-points grids were then plotted for both NiO structures. The converged k-points mesh which had a consistent energy for the structure, was then used to optimize the plane wave cut off energy.

The trial density was picked by specifying the kinetic energy cutoff for charge density and potential (ecutrho) which also depends on the type of pseudopotential to be used.

During the optimization process, the Nickel and Oxygen ultrasoft pseudopotentials (see Appendix C) were used. The ultrasoft pseudopotentials offer a faster convergence than norm-conserving pseudopotentials, because they reduce the number of plane waves, therefore convergence is achieved faster. As the optimization involved the use of ultrasoft pseudopotential, a larger value than the default value of ecutrho, was desirable, therefore the value of the charge density cut off (ecutrho) was 10 times ecutwfc value, during the optimization process. The values of minimum energies obtained with respect to the corresponding ecutwfc were then plotted, and the ecutwfc which had the lowest and consistent energy for the structure, and its corresponding ecutrho, were used for optimization of the lattice parameter. The lattice parameter found to have the lowest energy was used in all subsequent calculations.

4.2.3 Brillouin zone (BZ)

A Brillouin zone [65] is a Wigner-Seitz primitive cell in the reciprocal lattice. A Wigner-Seitz cell around a point is the set of points in space that are closer to that lattice point than to any of the other lattice points. A set of those points is referred to as the k-path. The BZ gives the vivid geometrical interpretation of the diffraction condition, which means the descriptions of electron energy band theory and of the elementary excitations of other kinds. To plot the band structure for RHL NiO, the high symmetry points and the path [66] in the primitive Brillouin zone of $\Gamma \rightarrow L \rightarrow B \rightarrow Z \rightarrow \Gamma \rightarrow Q \rightarrow F \rightarrow P_1 \rightarrow Z \rightarrow P$, generated using a crystalline and molecular structure visualisation programme (XCrysDen) [15, 67], were used, as shown in Figure 4.5.

Figure 4.5 shows the k-points and the k-path used for the band structure calculations of RHL NiO. The k-points coordinates for RHL structure are given in Table 4.1. For RHL NiO with α_{rh} = 33.557^0, the values of η and ν were calculated and found to be 0.8125 and 0.34375 respectively, while for RHL NiO with α_{rh} = 60.08^0, they were 0.7497 and 0.37515, respectively.

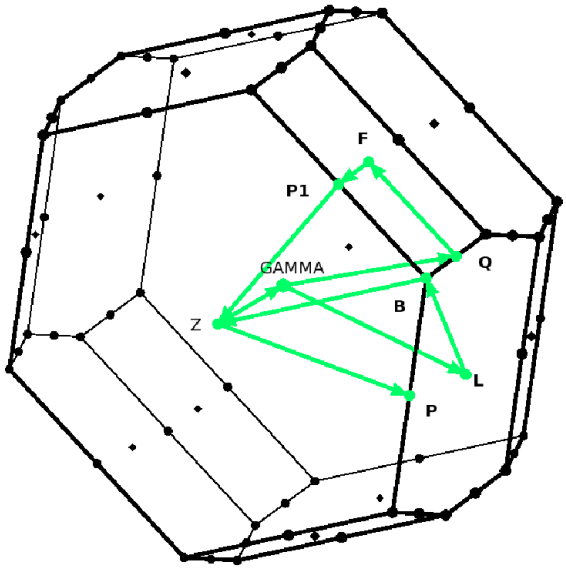

Figure 4.5: Brillouin zone of rhombohedral NiO.

Table 4.1: Symmetry k-points of RHL [66].

$\times b_1$	$\times b_2$	$\times b_3$		$\times b_1$	$\times b_2$	$\times b_3$	
0	0	0	Γ	η	ν	ν	P
η	$\frac{1}{2}$	$1-\eta$	B	1-ν	1-ν	1-η	P_1
$\frac{1}{2}$	1-η	1-η	B_1	ν	ν	η -1	P_2
$\frac{1}{2}$	$\frac{1}{2}$	0	F	1-ν	ν	0	Q
$\frac{1}{2}$	0	0	L	ν	0	- ν	X
0	0	-$\frac{1}{2}$	L_1	$\frac{1}{2}$	$\frac{1}{2}$	$\frac{1}{2}$	Z
$\eta = (1 + 4cos\alpha)/(2 + 4cos\alpha)$							
$\nu = 3/4 - \eta/2$							

4.2.4 Determination of Energy band gap

Owing to the extensive use of NiO in optical applications [3, 22, 68–70], determination of its energy band gap is key to these applications. In this study, the energy band gap was calculated with and without the U term in order to establish the manner in which it varies. From the basic definition, the fundamental energy band gap [65] is normally considered as the energy difference between the lowest point of the conduction band (the conduction band edge) and the highest point of the valence band (the valence band edge). For an indirect semiconductor, the electron transitions from the valence band to the conduction band can either be direct or indirect. Although the indirect transition requires less energy than direct transition, it has smaller probability of occurring than the direct transition, and

the absorption of a photon is proportional to the transition probability [71]. This means that in this study, the optical band gap was calculated as the minimum direct band gap, measured from the valence band edge to the conduction band at the same high symmetry k-point.

4.2.5 Determination of magnetic properties

Since Ni is a transition metal with some unpaired electrons, it is likely to influence the NiO matrix or crystal in a way that makes it magnetic. The bulk NiO possesses a RHL structure and exhibits AF behavior below its T_N of 523 K. Bulk RHL NiO calculations were done by assuming the two Ni atoms possess opposite but equal starting magnetizations, in order to consider its AF state. As such, during the calculations on RHL NiO, both structures with α_{rh} = 33.557^0 and α_{rh} = 60.08^0 were taken into account.

4.3 The GW formalism

The GW approximation was applied as a perturbation theory beginning from a DFT mean field Hamiltonian. The Nickel and Oxygen norm-conserving pseupotentials (see Appendix C) were used for DFT-GGA calculations. The GW calculations were performed by taking the wave functions and eigenvalues of a DFT-GGA calculations as an input for *Yambo* [16], in order to generate the core databases that contain the ground state data necessary for starting the code and to get a starting point of GW's non interacting method (GoWo). The Green function G was then updated to GWo, called GW-RPA, and thereafter both Green function G and screened Coulomb interaction W, (GW), were updated until self-consistency was obtained.

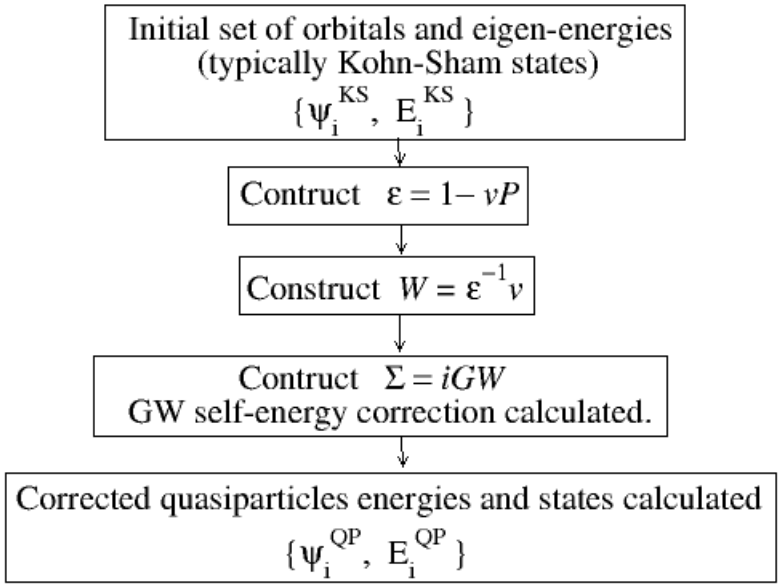

Figure 4.6: The schematic implementation of the GW method [14].

Figure 4.6 shows the schematic diagram of implementation of the GW method. In GW, the screened Coulomb potential W is calculated with the dielectric matrix (ε) at the RPA level. The self-energy Σ can be obtained from a self-consistent set of Dyson-like equations (i.e., diagonalized within the basis) known as Hedin's equations seen in Section 3.6.1, and is just the direct product of G and W [52]. For the GW calculations, the GW Newton solver was used and the dynamical screened interaction is studied with Plasmon Pole Approximation and RPA.

Since the electromagnetic spectrum of interest to this study ranges from near infrared (750 nm, i.e 1.65 eV) up to ultraviolet (200 nm, i.e 6.18 eV), the energy calculations were limited from 0 eV to 10 eV, i.e from $+\infty$ to 123.7 nm (see Figures 5.13 - 5.16).

4.4 The BSE formalism

The Bethe Salpeter Equation (BSE) is normally solved to treat Excitonic effects introduced by using the electron-hole (e-h) Green's function [61]. The BSE calculations take as input the quasiparticle energies and wave functions from GW, therefore the calculations start from the GGA or LDA within the DFT, then the GW and its correction. Often only a scissor shift is applied, and the eigenstates are updated. Figure 4.7, shows the procedure for a GW-BSE calculations.

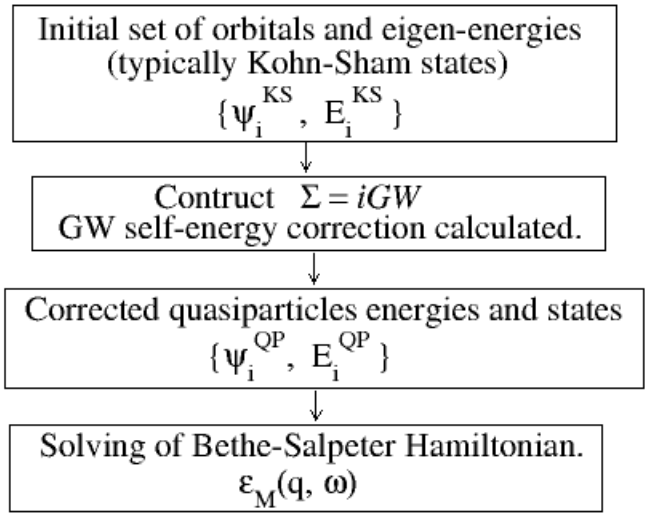

Figure 4.7: Procedure for BSE calculations [14] .

The full dielectric matrix calculated in the GW step is used to screen the attractive direct electron-hole interaction. With the excitation energies and amplitudes of the electron-hole pairs, the macroscopic dielectric function for various light polarizations can be calculated, and quantities like electron-hole correlation functions in real space and higher-order optical effects such as multi-photon absorption and phonon-assisted absorption spectra are obtained [14, 52]. The full BSE with screened interaction (Static screened interaction) was used for the Approximations for the Kernel, with the Haydock as the BSE solver.

CHAPTER FIVE

RESULTS AND DISCUSSION

5.1 Study of structural properties of bulk NiO using LSDA+U

5.1.1 Structural properties of rhombohedral NiO with α_{rh} = 60.08^0

Below its Néel temperature of 523 K, NiO transforms from fcc structure to a rhombohedral (RHL) structure by a compression along the body diagonal direction with the rhombohedral angle α_{rh} being 60.08^0 [10, 12, 25] as shown in Figures 4.3 and 5.1. The lattice parameter a of RHL NiO with α_{rh} = 60.08^0 shown, was calculated as follows: $a = b = c = \frac{1}{2}\sqrt{a_0^2 + a_0^2} = \frac{\sqrt{2}}{2}\, a_0 = 5.5699\ a.u.$ In this study, the LSDA+U optimization of RHL NiO involved the use of a dense k-point mesh of $15 \times 15 \times 15$ and an energy cutoff (ecutwfc) of 50 Ry, (see Appendix A, Figures A.1 - A.2).

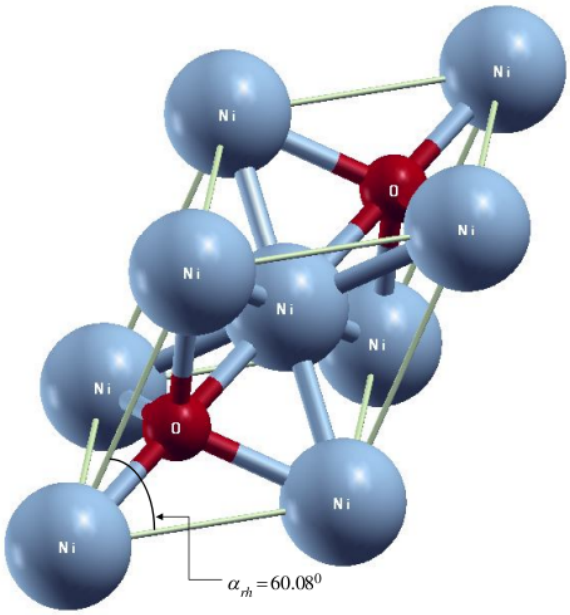

Figure 5.1: Optimized structure of RHL NiO with α_{rh} = 60.08^0.

Table 5.1 shows that the optimized lattice constant (see also Appendix A, Figures A.3 - A.7) for LSDA and LSDA+U calculations, is greater than the experimental one of 5.571 a.u [10] owing to the different conditions under which the experiment was done.

The bulk modulus and its pressure derivative of RHL NiO were calculated using Murnaghan's Equation of State [26] and were found to be 170.3 GPa and 5.19, respectively.

Table 5.1: Calculated DFT - LSDA and LSDA+U lattice constant a, bulk modulus B_0, first pressure derivative of the bulk modulus B_0' and the bond lengths $Ni-Ni$ and $Ni-O$ of RHL NiO with α_{rh} = 60.08^0.

	LSDA	LSDA+U				Experiment
U (eV)	-	5.4	6.2	7.3	8	-
a (a.u)	6.716	6.785	6.786	6.789	6.793	5.571 [10]
B_0 (GPa)	170.3	156.3	155.8	155.2	155.2	184 [12]
B_0'	5.19	4.52	4.55	4.57	4.56	4.93 [12]
$Ni-Ni$ (a.u)	4.7518	4.8006	4.8013	4.8035	4.8063	-
$Ni-O$ (a.u)	4.1102	4.1524	4.1530	4.1549	4.1573	-
	4.1168	4.1591	4.1597	4.1616	4.1640	-

The calculated bulk modulus without U term, was however small by 13.7 GPa compared to the experimental bulk modulus of 184 GPa, while the calculated pressure derivative was higher than the experimental of 4.93 [12] by 0.26 for RHL NiO with α_{rh} = 60.08^0.

The calculated Ni-Ni bond length was 4.7518 a.u and the Ni-O bond lengths were 4.1168 a.u and 4.1102 a.u for LSDA calculations without U term. The lattice parameter and the bond length were found to increase slightly with U term, while the bulk modulus was decreasing with U term, as shown in Table 5.1. The bond angles Ni-Ni-Ni were found to be 90.069^0 and 89.931^0, while the Ni-Ni-O bond angles were found to be 54.785^0 and 54.654^0. The bond angles Ni-O-Ni were found to be 109.504^0, 109.439^0 and 70.561^0, demonstrating a significant variation due to the distortion in the structure.

5.1.2 Structural properties of rhombohedral NiO with α_{rh} = 33.557^0

The RHL distorted NiO rock salt structure is also achieved by a compression along the body diagonal direction with the rhombohedral angle α_{rh} being 33.557^0. This is shown in Figures 4.4 and 5.2. The lattice parameter of RHL NiO with α_{rh} = 33.557^0 shown in Figure 4.4, was calculated as follows: $a = b = c = \sqrt{a_0^2 + \frac{a_0^2}{2}} = \sqrt{\frac{3}{2}}\, a_0 = 9.6475\ a.u.$

A k-point mesh of $12 \times 12 \times 12$ and a Plane wave energy cut off (ecutwfc) value of 50 Ry, were used for the calculations involving both LSDA and LSDA+U for RHL NiO with an angle of 33.557^0 (see Appendix A, Figures A.8 - A.27). A lattice parameter of 9.408 a.u was obtained for the calculation without the U term, and it was found to increase with

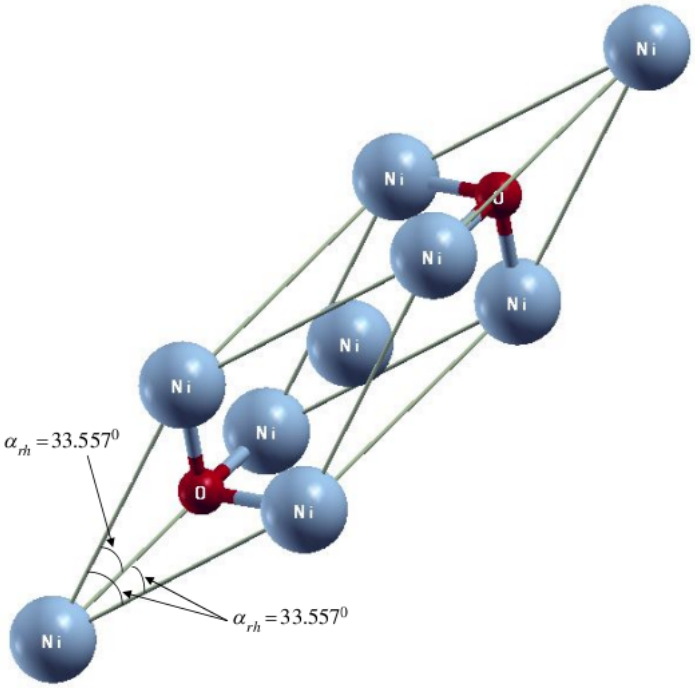

Figure 5.2: Optimized structure of RHL NiO with α_{rh} = 33.557^0.

increasing U term. For a U term of 9.5 eV, a lattice parameter of 5.107 Å= 9.652 a.u was obtained, which was only slightly longer than the experimental value of 9.648 a.u by 0.041 %.

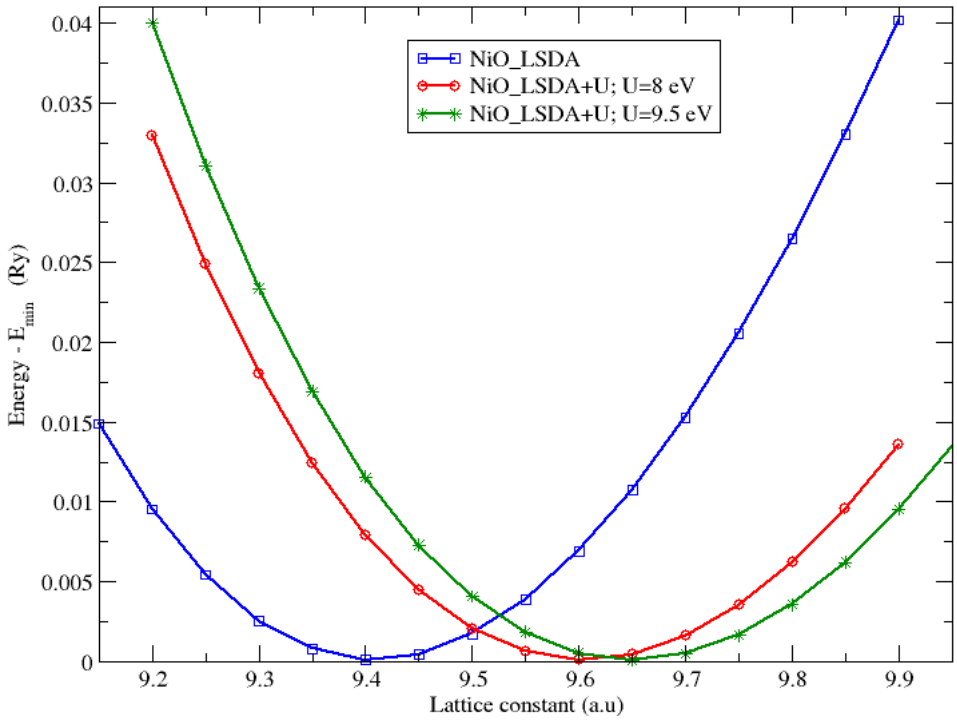

Figure 5.3: Optimized lattice constant of RHL NiO for LSDA and LSDA+U.

Therefore, a U term of 9.5 eV is used for calculating other properties of RHL NiO with 33.557^0. A plot of the total energy with lattice parameters for LSDA and LSDA+U is shown in Figure 5.3, whereby a clear shift in the value of the lattice parameter is seen after including the Hubbard term, and this suggests that the U term shifts the charge density in a manner that increases the size of the unit cell. This also effectively alters the energy band gap. The increase of lattice parameter with U term is also shown by Table 5.2.

Table 5.2: Calculated DFT - LSDA and LSDA+U lattice constant a, bulk modulus B_0, first pressure derivative of the bulk modulus B_0', the bond length $Ni-O$ and bond angles $Ni-O-Ni$ and $O-Ni-O$ of RHL NiO with α_{rh} = 33.557^0.

	LSDA	LSDA+U								
U (eV)	-	5.4	6.2	7.3	8	8.5	9	9.5	10	12
a (a.u)	9.408	9.536	9.556	9.586	9.605	9.620	9.635	9.652	9.668	9.738
B_0 (GPa)	276.3	247.5	243.4	237.6	233.7	230.2	227.6	224.5	222.2	211.0
B_0'	4.82	4.60	4.54	4.47	4.42	4.44	4.42	4.32	4.34	4.19
$Ni-O$ (a.u)	3.841	3.893	3.901	3.913	3.921	3.927	3.936	3.940	3.948	3.980
$Ni-O-Ni$	90^0	90^0	90^0	90^0	90^0	90^0	90^0	90^0	90^0	90^0
$O-Ni-O$	90^0	90^0	90^0	90^0	90^0	90^0	90^0	90^0	90^0	90^0

The bulk modulus for RHL NiO with α_{rh} = 33.557^0 was found to be B_0 = 224.5 GPa when a U term of 9.5 eV was used. This value was closer to the bulk modulus value of 230.72 GPa calculated recently by Gillen and Robertson [11]. Table 5.2 further shows that the bulk modulus for RHL NiO with α_{rh} = 33.557^0 decreased with increasing U term. This observation is consistent with the observed increase in the lattice parameter with increasing U term. The calculated first pressure derivative of the bulk modulus, B_0', was found to decrease with increase of the U term, from 4.82 for LSDA calculations, up to 4.32 for LSDA+U with Hubbard term of 9.5 eV. The calculated values of B_0' were in the range of other reported theoretical values, which lie between 3.6 and 5.7 [25]. The calculated bond angle between Ni-O-Ni and O-Ni-O was found to be 90 degrees, while the value of the Ni-O bond length increased from 3.841 a.u for LSDA without U term, to 3.940 a.u with inclusion of U term of 9.5 eV, an increase that was consistent with the observed increase in the lattice parameter with increasing U term.

5.2 Study of electronic properties of bulk NiO with LSDA+U

5.2.1 Electronic properties of rhombohedral NiO with α_{rh} = 60.08^0

The band structure of bulk RHL NiO with α_{rh} = 60.08^0 studied with LSDA, is shown in Figure 5.4. The zero of the energy was set at the Fermi energy (E_F) value. Figure 5.4

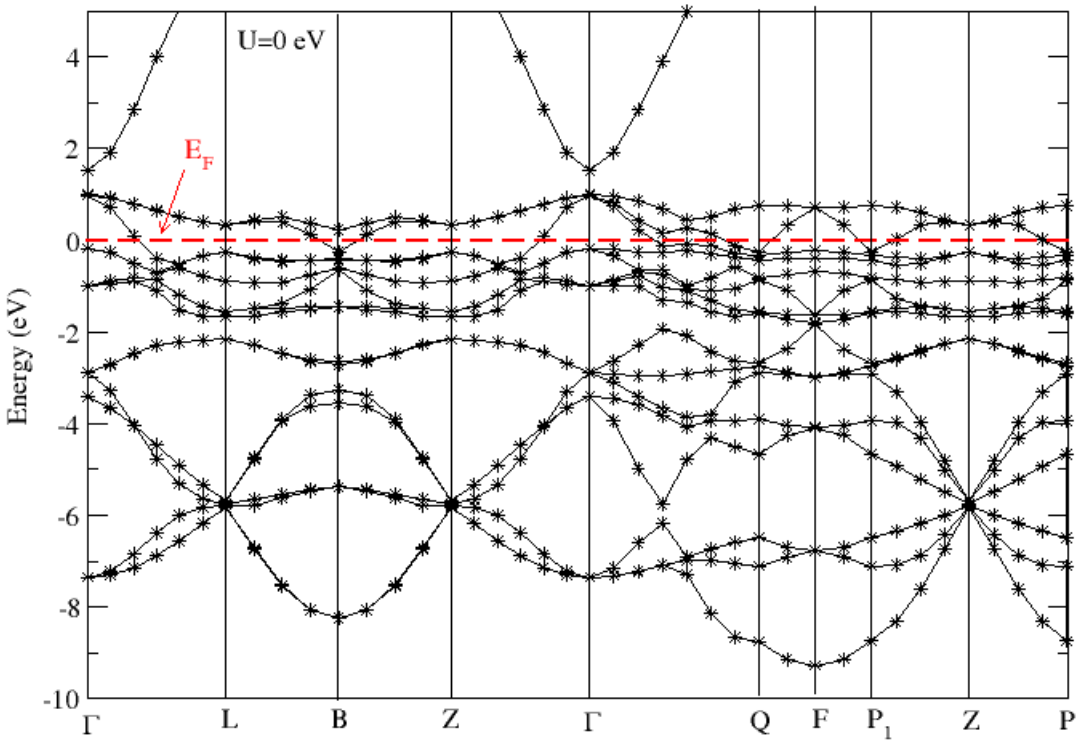

Figure 5.4: Band structure of bulk RHL NiO of α_{rh} = 60.08^0, calculated using LSDA.

further shows that the valence and the conduction bands overlap; therefore the material seems to be a metal instead of being a semiconductor with a wide energy band gap. The same results were found with inclusion of U term as shown in Appendix B, Figures B.1 - B.2. This means that, both LSDA and LSDA+U approaches did not describe correctly the electronic properties of RHL NiO with α_{rh} = 60.08^0, and this might be due to the reduction of the lattice parameter, as it was smaller by 1.161 a.u when compared to the experimental lattice parameter of 7.877 a.u for fcc NiO. Due to this incorrect prediction of the electronic properties of rhombohedral NiO with α_{rh} = 60.08^0, and owing to the fact that NiO exists in either fcc structure, RHL structure with α_{rh} = 60.08^0 and also rhombohedral structure with α_{rh} = 33.557^0, it was necessary to also study the electronic properties of RHL NiO with α_{rh} = 33.557^0 as outlined in the following subsections.

5.2.2 Electronic properties of rhombohedral NiO with α_{rh} = 33.557^0

For the LSDA calculations on RHL NiO with α_{rh} = 33.557^0 in the antiferromagnetic (AF) state, both narrow indirect and direct band gaps of 0.61 eV and 0.85 eV, respectively, were obtained as shown in Figure 5.5. The valence band edge for the RHL NiO was located at the Z point, whereas the conduction band edge was located almost midway between Γ and L points. Correspondingly, the minimum direct band gap was found at Z point.

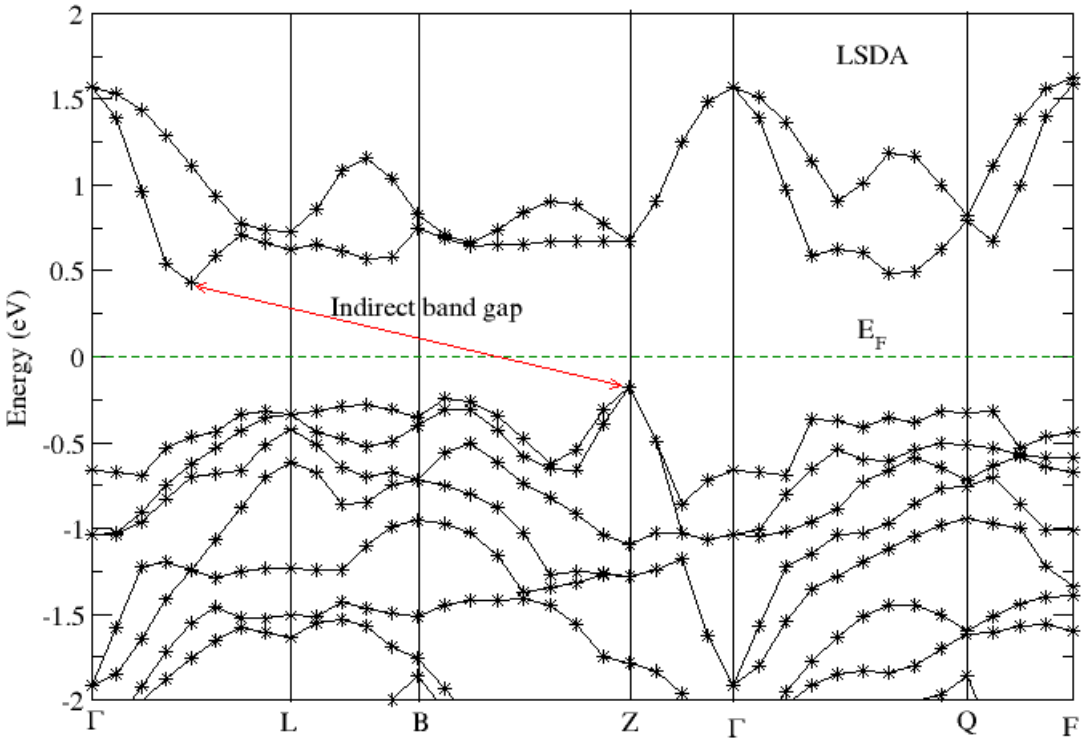

Figure 5.5: Band structure of RHL $(\alpha_{rh}$ = $33.557^0)$ **NiO calculated using LSDA.**

The value of the band gap energy was found to increase with the value of U term as shown in Figures 5.6, 5.7 and 5.8 and Table 5.3. For purposes of referencing the band gap, the Fermi energy was set at 0 eV as mentioned earlier.

Figure 5.6 shows the calculated density of states (DOS) for RHL NiO with α_{rh} = 33.557^0, whereby the Fermi energy was set at 0 eV. Both the conduction band and valence band edges were shifted from the E_F in opposite directions by around 1.3 eV and 1.5 eV, respectively, when a U term of 9.5 eV was used.

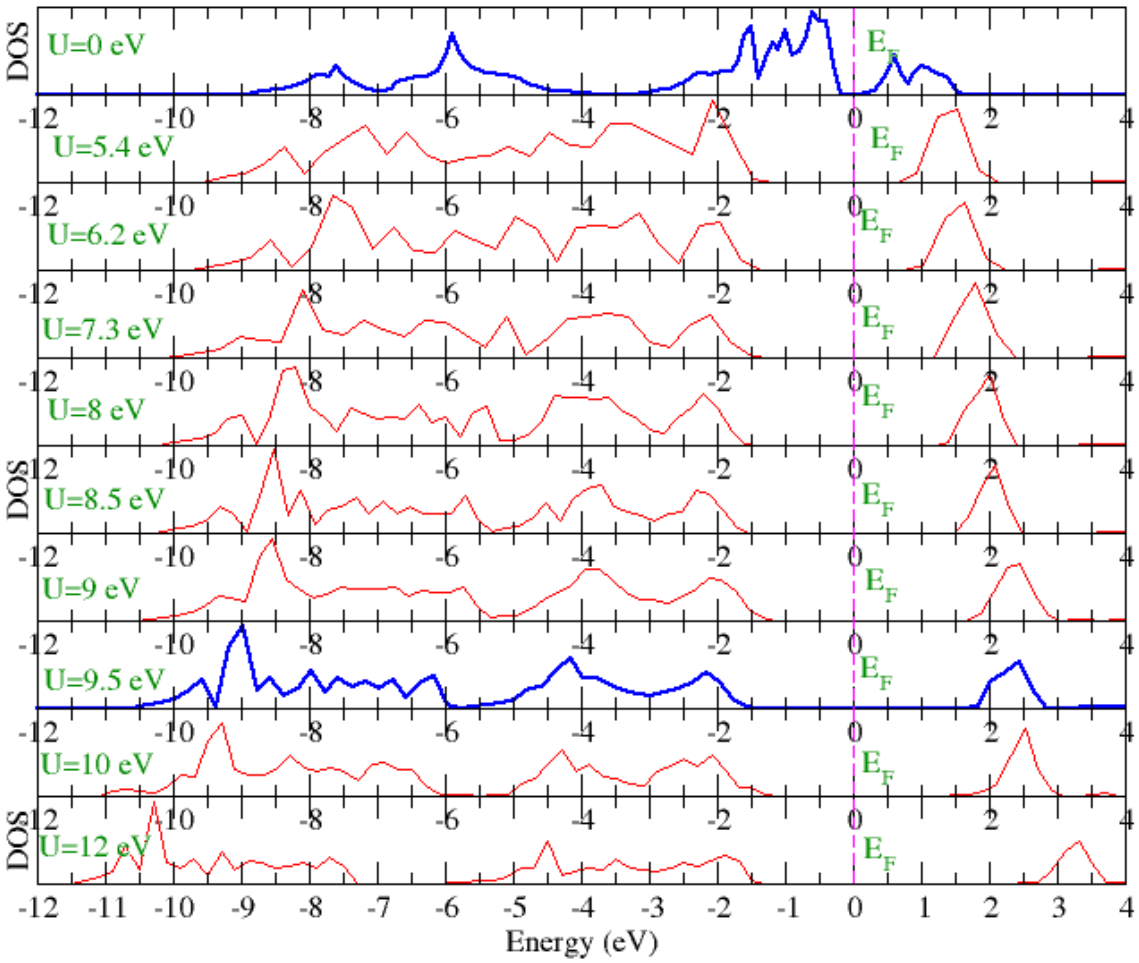

Figure 5.6: DOS of RHL (α_{rh} = 33.557^0) **NiO for LSDA and LSDA+U.**

The features of the DOS have also been found to change with varying U terms, due to the charge redistribution. The highest intensity peak which was located at the top of the valence band, for the calculations without U term, was found to be located almost at the bottom of the valence band for LSDA+U calculations, especially for values of U greater than 6.2 eV (see Figure 5.6). The features of the DOS in the conduction band have also been found to change with U term, where the peak intensities were found to decrease with increasing value of the U term.

For the LSDA+U calculations, the valence band edge for RHL (α_{rh} = 33.557^0) NiO was also located at the Z point (see Figure 5.7), but the conduction band edge was located between B and Z points, for U term varying between 5.4 eV and 8.5 eV (see Appendix B, Figures B.3 - B.7), while it was located at Γ point for U term greater than 9 eV (see Figure 5.7 and Appendix B, Figures B.8 - B.10), unlike in the case of plain LSDA where this was

found between Γ and L. Likewise to LSDA calculations, the minimum direct band gap was found at Z point.

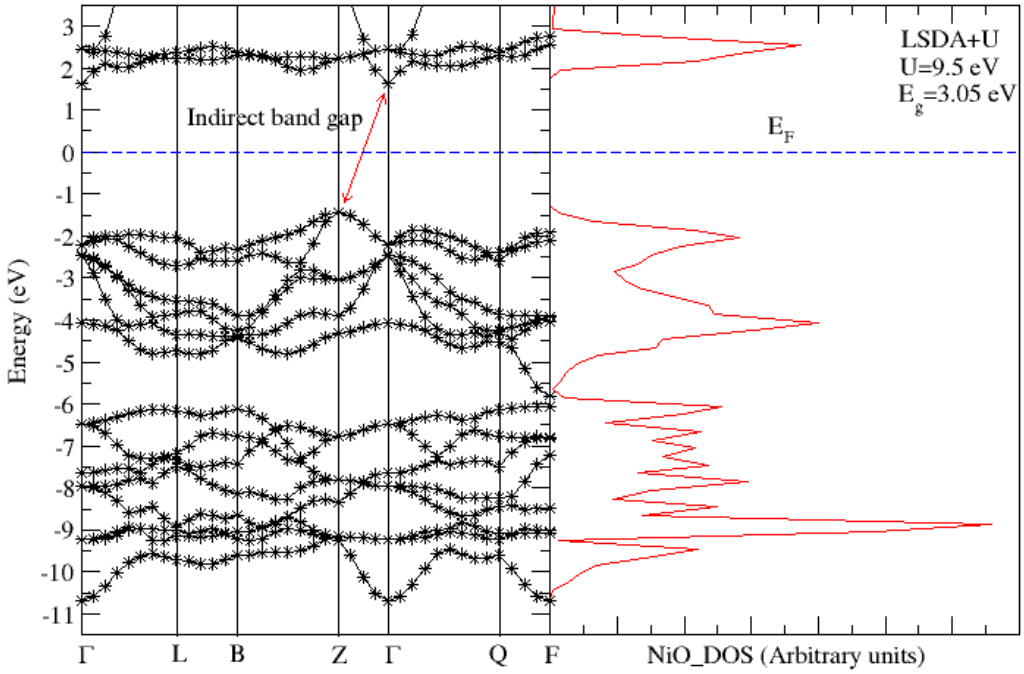

Figure 5.7: Band structure and DOS of RHL $(\alpha_{rh} = 33.557^0)$ **NiO with LSDA+U, U = 9.5 eV.**

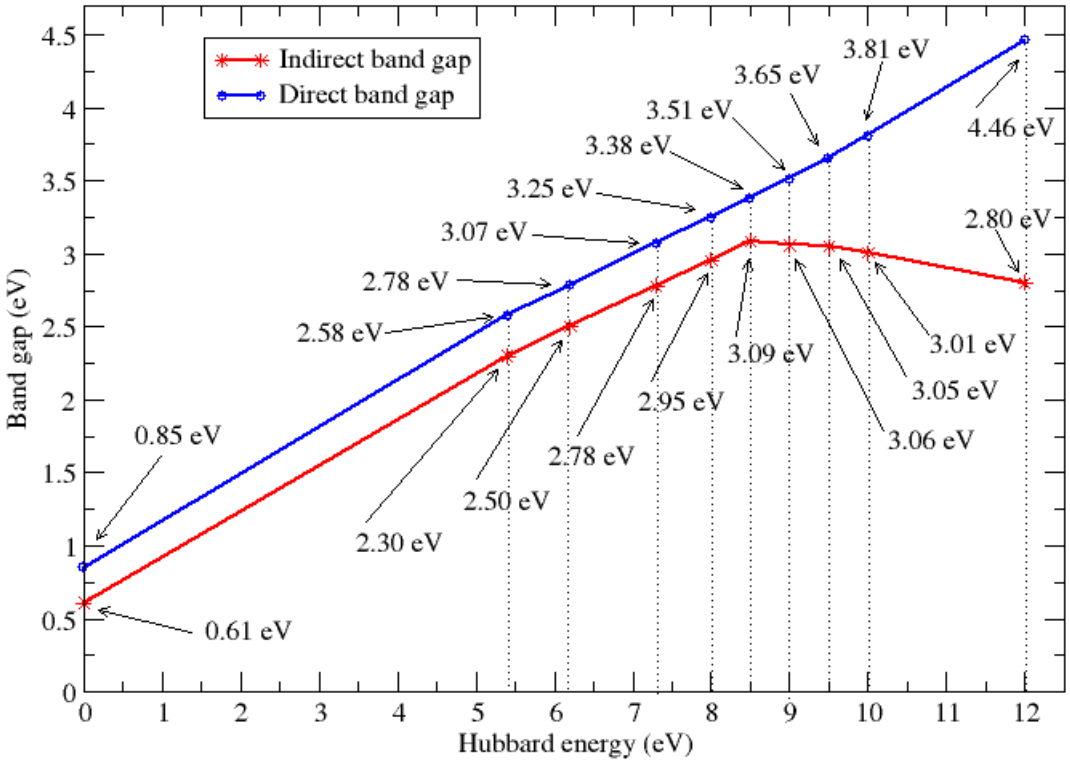

Figure 5.8: Variation of energy band gap with U term.

From Figures 5.5 - 5.8, it is found that the addition of the U term in LSDA opens both the indirect and the direct band gaps from 0.61 eV and 0.85 eV, respectively, (see Figures 5.5 and 5.6 (U=0 eV)) to 3.05 eV and 3.65 eV (see Figures 5.6 (U=9.5 eV) and 5.7 - 5.8), respectively, for U=9.5 eV. Generally, the calculated direct band gap was found to increase with increasing value of the Hubbard term U, while the indirect band gap was found to increase from 0.61 eV to 3.09 eV, and then start decreasing as summarized in Figure 5.8 and Table 5.3. The calculated values of the indirect and direct band gap of 3.05 eV and 3.65 eV, respectively, for a U term of 9.5 eV are within the range of some other calculated band gap values as shown in Table 5.3.

Table 5.3: Calculated band gap values for RHL $(\alpha_{rh} = 33.557^0)$ **NiO.**

	U (eV)	Band gap (eV)	
		Indirect band gap	Direct band gap
LSDA	-	0.61	0.85
LSDA+U	5.4	2.30	2.58
	6.2	2.50	2.78
	7.3	2.78	3.07
	8	2.95	3.25
	8.5	3.09	3.38
	9	3.06	3.51
	9.5	3.05	3.65
	10	3.01	3.81
	12	2.80	4.46
Other theoretical work			
LDA+U	5 [28] ; 7 [2]	2.6 [28]; 3.8 [2]	
LSDA+U	6.1 [29] ; 5.4 [27]; 6.2 [20, 23]	3.7 [29] ; 3 [20] ; 4.04 [23]; 4.1 [27]	
GGA+U	4.6 [19] ; 6.2 [23]	4.31 ; 3.4 [23]	2.7 [19]

Figures 5.9 - 5.10 show the calculated projected density of states (PDOS) for RHL $(\alpha_{rh} = 33.557^0)$ NiO for LSDA and LSDA+U approaches.

Figure 5.9 shows that the Ni 3d up states and O 2p states are situated in the valence band while Ni 3d down states are located at the top of the valence and at the bottom of the conduction band. Therefore Ni 3d states dominate the upper edge of the valence band and the conduction band too, whereas the higher energies in the valence band between - 9 eV

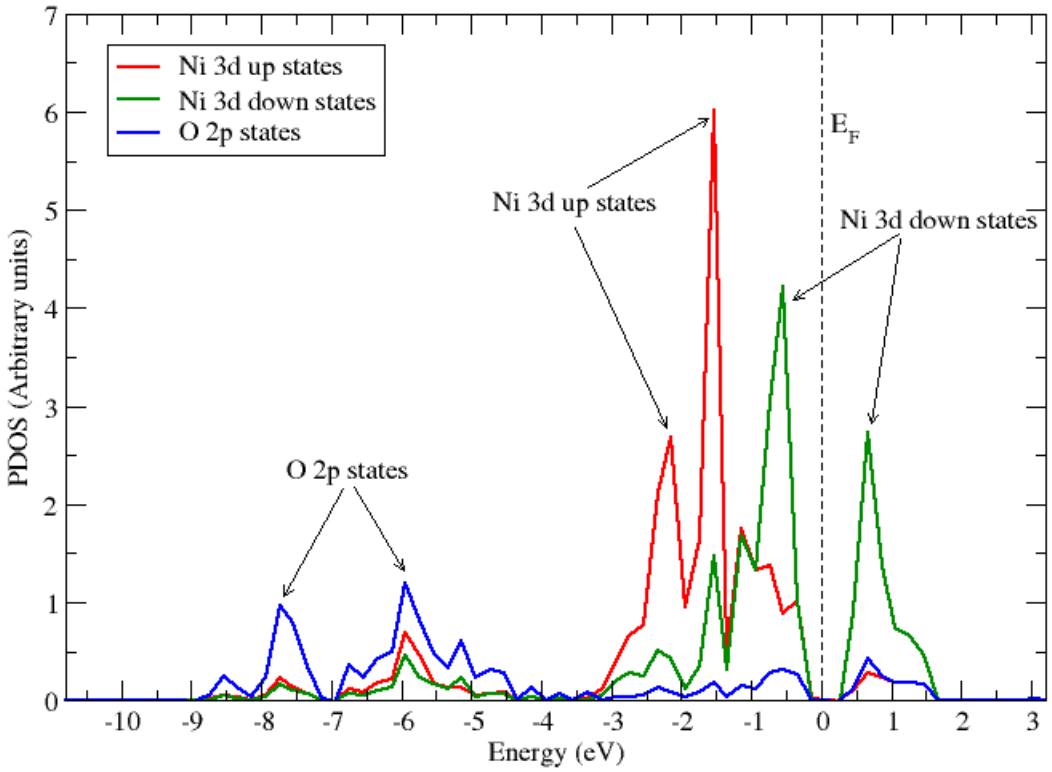

Figure 5.9: PDOS of RHL $(\alpha_{rh} = 33.557^0)$ **NiO with LSDA.**

and - 4 eV are occupied predominantly by O 2p states. The conduction band and the upper edge of the valence band was of the same character (d-d type), suggesting that NiO is a Mott-Hubbard insulator.

However, other studies [19, 20, 29, 30, 35, 36], have predicted NiO to be a "Charge transfer insulator" with a big band gap instead of being a "Mott-Hubbard insulator". To investigate the findings of these studies, the LSDA+U method was employed and the results are shown in Figure 5.10.

In Figure 5.10, a mixed character of Ni 3d and O 2p states was observed in the valence band, but it was mainly dominated by an appreciable amount of Ni 3d up and down states. The upper edge of the highest occupied molecular orbitals (Valence band) is dominated by O 2p orbitals whereas the bottom of the conduction band is occupied by Ni 3d down states. It is also important to notice that the inclusion of U term shifts the Ni 3d up states to the higher energies within the valence band, with a strong peak located at around - 9 eV, while the O 2p states are shifted to the top of the valence band with a strong peak located at around - 2 eV. As such, the band gap character is a p-d type and NiO, therefore be-

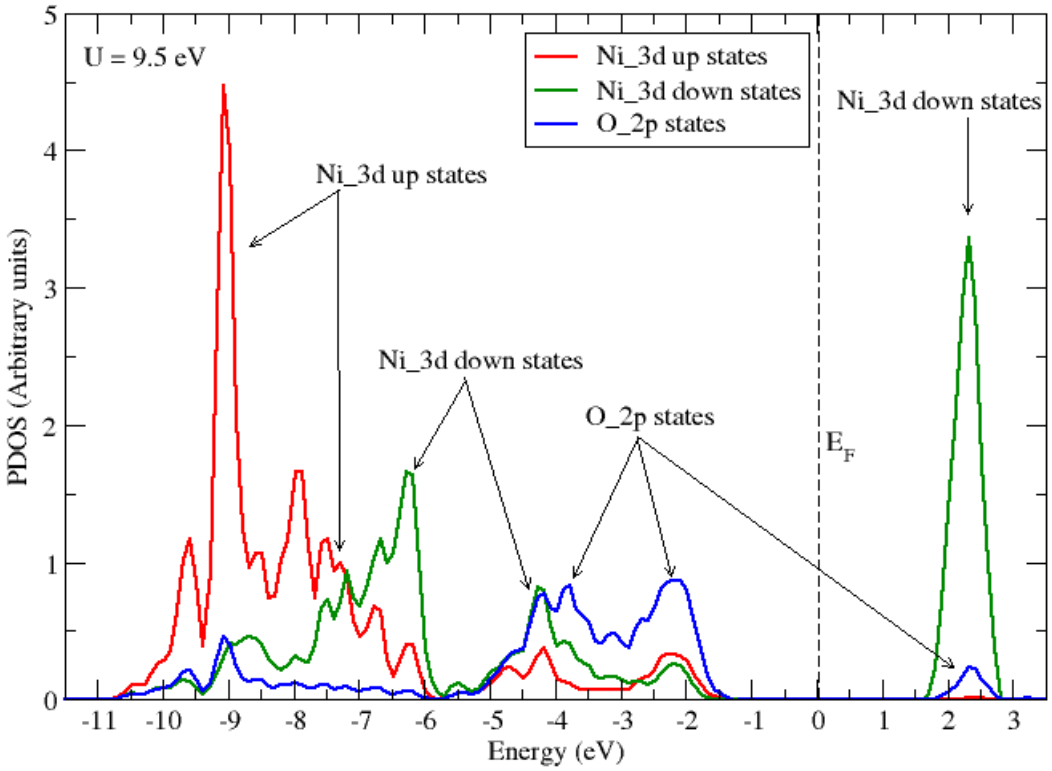

Figure 5.10: PDOS of RHL $(\alpha_{rh} = 33.557^0)$ **NiO with LSDA+U, U=9.5 eV.**

comes a "Charge transfer insulator" which is in good agreement with some other previous theoretical [19, 20, 29, 30] and experimental [35, 36] works.

5.3 Study of magnetic properties of bulk NiO using LSDA+U

The bulk NiO possesses a RHL structure and exhibits AF behavior below its N_N 523 K. Both RHL NiO structures with α_{rh} = 33.557^0 and α_{rh} = 60.08^0 were taken into account, and Figures 5.11 and 5.12 show plots of magnetic density of states for the spin up and spin down states for RHL NiO. Both Figures 5.11 and 5.12 show that RHL NiO, with α_{rh} = 60.08^0 and α_{rh} = 33.557^0, is indeed an antiferromagnetic material of type two (AF2), as the total magnetization was found to be 0.00 Bohr mag/cell.

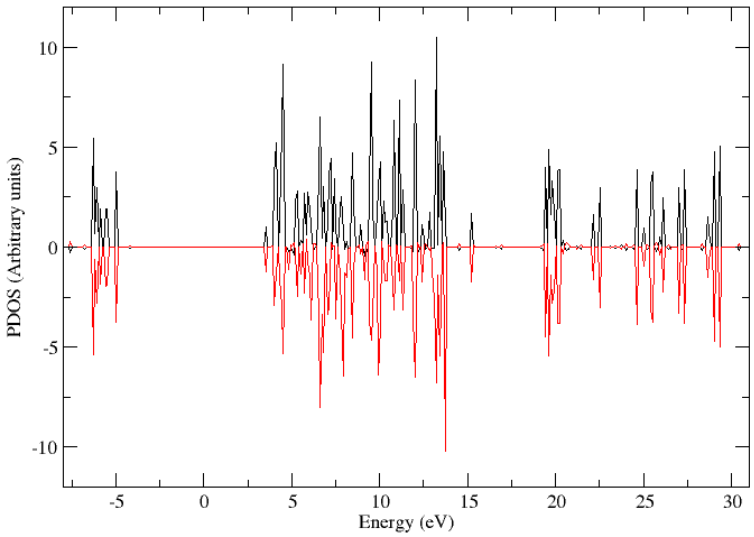

Figure 5.11: Calculated up and down spins of RHL NiO of α_{rh} = 60.08^0 studied by LSDA+U, U=8 eV.

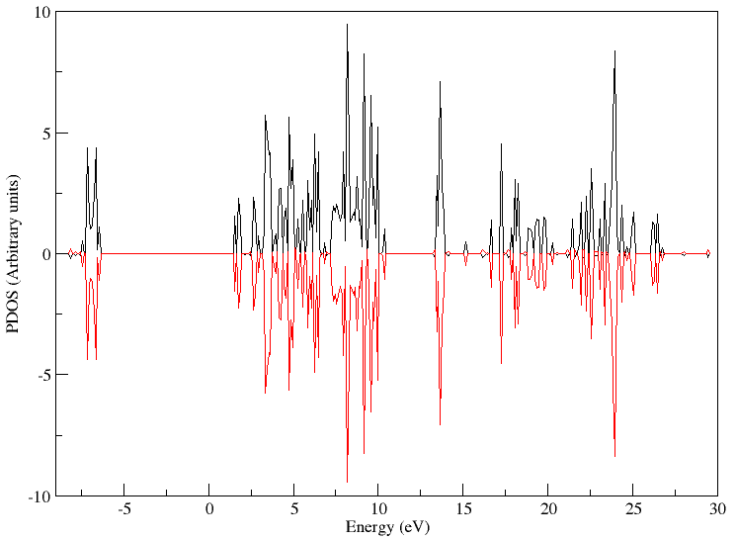

Figure 5.12: Calculated up and down spins of RHL NiO of α_{rh} = 33.557^0 studied by LSDA+U, U=9.5 eV.

5.4 Study of optical properties of bulk NiO using GW and BSE

In this section, the optical properties of fcc NiO and RHL NiO with α_{rh} = 33.557^0 were investigated using *Yambo* code. The optical properties of NiO with α_{rh} = 60.08^0 were not investigated because it was predicted earlier to be a metal.

5.4.1 Optical properties of fcc NiO

Figure 5.13 shows the absorption energy spectrum of fcc NiO. It shows a plot of the imaginary part of the energy absorption spectrum, which was plotted because the absorption is linked to the imaginary part of the macroscopic dielectric function [72], as shown earlier in Eq. (3.56).

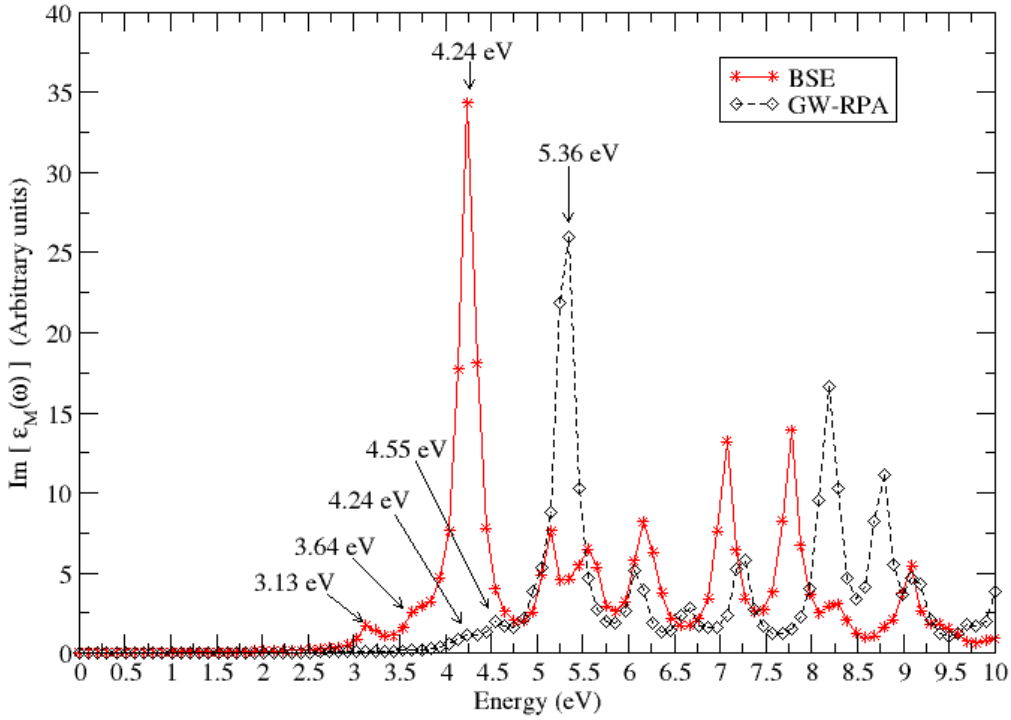

Figure 5.13: Absorption energy spectrum for fcc NiO.

The first bound exciton peaks were established at 3.13 eV and 4.24 eV for the BSE and GW-RPA methods, respectively, and their positions indicate the size of the indirect band gap. The highest intensity peak of the absorbed energy is observed for BSE at approximately 4.24 eV whereas this is observed at 5.36 eV for GW-RPA. Thus, the GW-RPA graph is shifted by 1.12 eV to the right of the BSE plot. The other major peaks are ob-

served at 4.55 eV and 8.18 eV for GW-RPA and at 3.64 eV; 7.07 eV and 7.78 eV for the case of BSE.

Contrary to absorption linked to the imaginary part of the macroscopic dielectric function, the electron energy loss (EEL) is linked to the imaginary part of the inverse of the macroscopic dielectric function [72], as seen in Eq. 3.57. In this case, the EEL peaks observed between 3 eV and 10 eV in Figure 5.14 are due to mobile concentration of energy in a crystal formed by excited electrons and associated holes (exciton states) [16, 73].

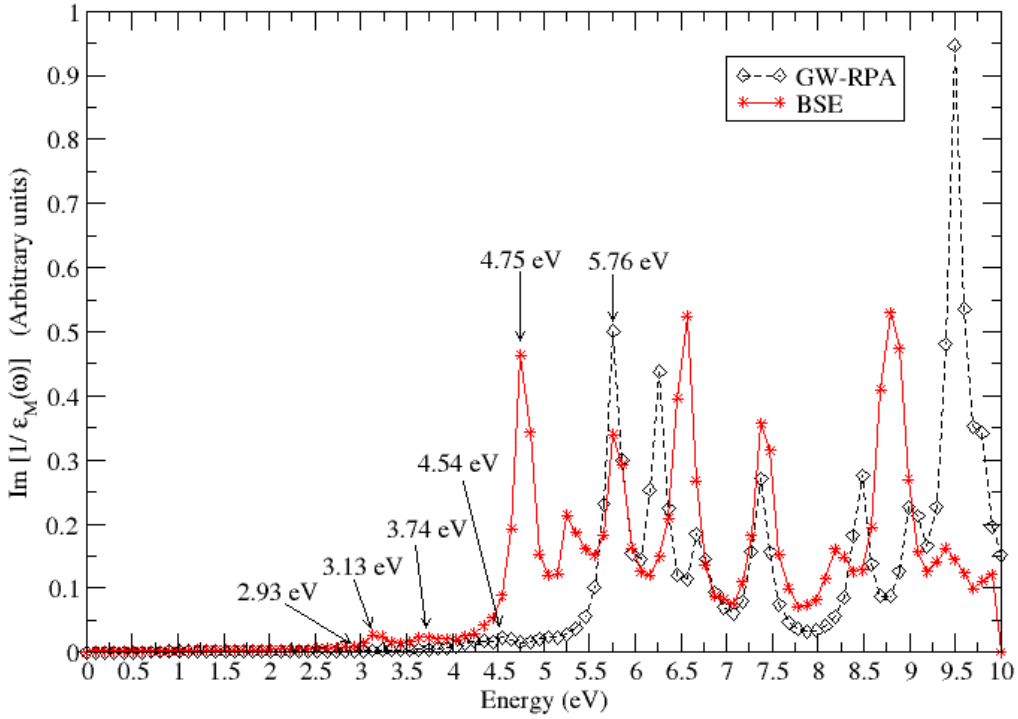

Figure 5.14: Electron energy loss spectrum for fcc NiO.

The spectral intensity is related to the electronic transitions between conduction and valence bands just like in the case of density of states. Ideally the inelastic intensity should remain zero up to an energy loss equal to the band gap energy of the material. However, exciton peaks can also occur due to transitions to exciton states below the conduction band [73]. The first peak for EEL spectrum of fcc NiO located at 3.13 eV for BSE, corresponds to the size of the optical indirect band gap, whereas for GW-RPA aproach the first peak is located at 4.54 eV represents fundamental indirect band gap. In general the GW-RPA method appears to overestimate the indirect band gap of fcc NiO.

5.4.2 Optical properties of Rhombohedral NiO with α_{rh} = 33.557^0

As mentioned earlier, the NiO absorption spectrum is obtained from the imaginary part of the macroscopic dielectric function. Figure 5.15 shows that RHL NiO with α_{rh} = 33.557^0 has major absorption peaks at around 3.23 eV, 3.74 eV, 5.35 eV and 9.90 eV for BSE, and at around 3.74 eV, 4.24 eV and 5.86 eV for GW-RPA. The highest and most intense peaks are situated near 4.24 eV and 3.74 eV for GW-RPA and BSE, respectively. The first peak positions for both BSE and GW-RPA correspond to optical and fundamental, respectively, indirect band gap of RHL NiO with α_{rh} = 33.557^0 and they are both within acceptable errors of experimental band gap which is in range of 3.5 eV - 4 eV [1–8].

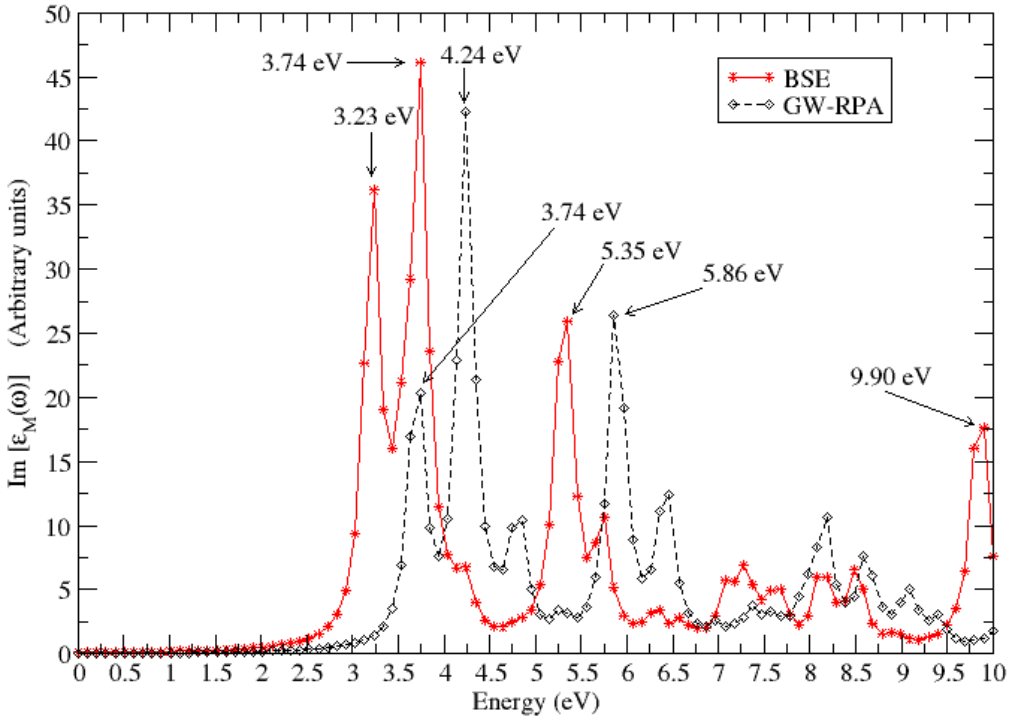

Figure 5.15: Absorption energy spectrum for RHL NiO with α_{rh} = 33.557^0.

Figure 5.15 shows that the absorption energy spectrum for RHL NiO with α_{rh} = 33.557^0 is characterized by a weak intensity in the low energy range (0 – 2.5 eV) and, relatively stronger peaks at around 3.23 eV (282.8 nm) and 3.74 eV (330.9 nm). Therefore, there is minimal absorption in the range of the infrared to the visible region and stronger absorption towards the ultraviolet region, and this is in agreement with other experimental works [1, 3, 9, 13, 74].

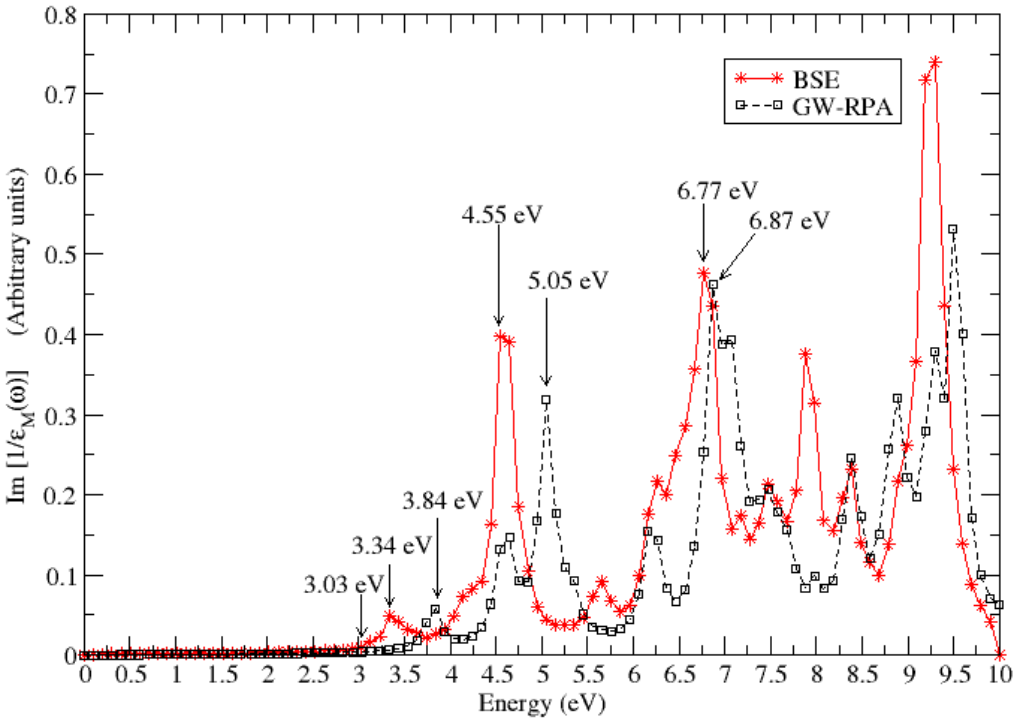

Figure 5.16: Electron energy loss spectrum for RHL NiO with α_{rh} = 33.557^0.

Figure 5.16 shows EEL spectra observed for BSE and RPA calculations in the case of RHL NiO with α_{rh} = 33.557^0. It shows that the onset of optical absorption in RHL NiO starts at a photon energy of around 3.03 eV. Peaks between 3 eV and 10 eV are due to exciton states [16, 73], as seen for the EEL in fcc NiO. For GW-RPA, the first peak is observed at 3.84 eV and indicates the size of NiO fundamental direct band gap, while from the BSE calculations the optical band gap is found to be 3.34 eV.

By updating both Green function G and screened Coulomb interaction W, the GW approach was used and the band structures obtained with this method are shown in Figures 5.17 - 5.18, for fcc and RHL (α_{rh} = 33.557^0) NiO structures, respectively. From Figure 5.17, a direct band gap of 2.51 eV was obtained at Γ point with the GW approximation, a value that is small compared to the other calculated values by about 1.5 eV on average. Unlike the fcc structure where the fundamental band gap was a direct band gap, the fundamental band gap for RHL NiO with α_{rh} = 33.557^0, was found to be an indirect one of 3.46 eV and it was from B to Γ points as shown in Figure 5.18.

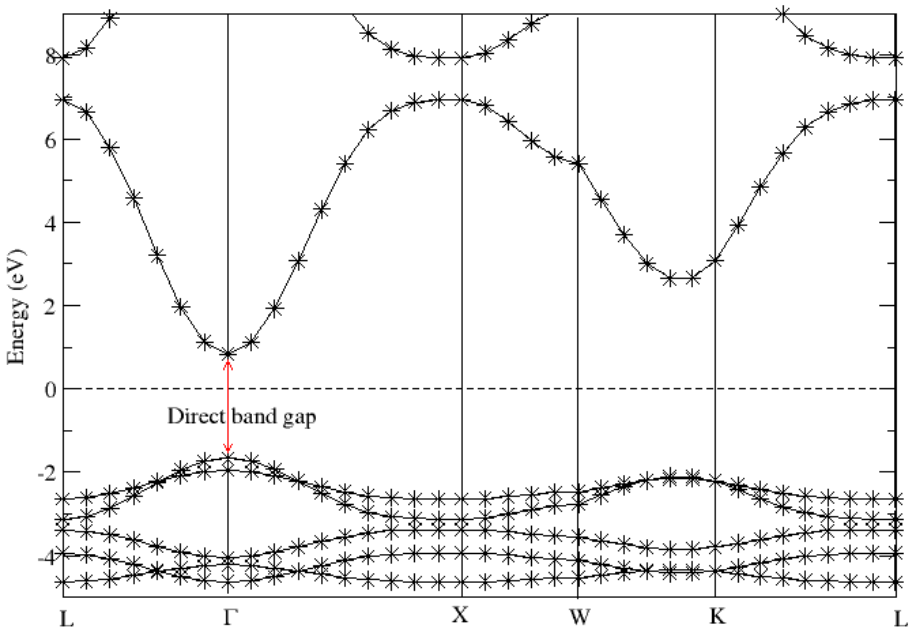

Figure 5.17: Band structure of fcc NiO with GW.

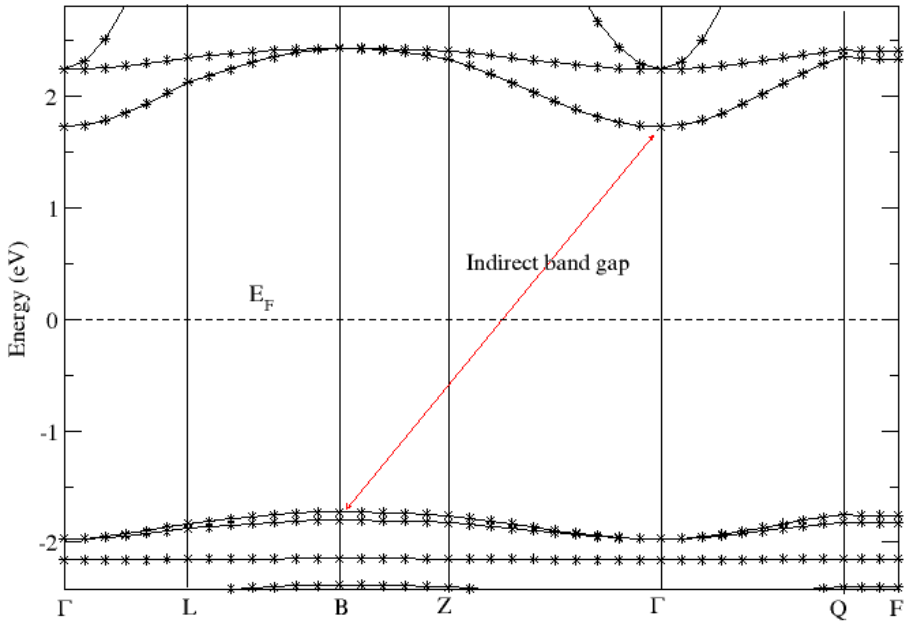

Figure 5.18: Band structure of RHL NiO of α_{rh} = 33.557^0 with GW.

The energy band gap values obtained for the non-interacting system with Green's function and the dynamically screened Coulomb interaction based on GGA calculations GoWo-GGA, the interacting system with updated Green's function GW-RPA based on GGA calculations GWo-GGA, as well as updated G and W (GW) functions, and BSE methods are summarized in Table 5.4.

These are presented together, so as to compare with the other theoretical and experimental values.

Table 5.4: Theoretical and experimental values of energy band gap of NiO.

Methods	U (eV)	fcc NiO band gap (eV)		RHL NiO (α_{rh} = 33.557^0) band gap (eV)	
		Indirect	Direct	Indirect	Direct
GoWo-GGA	-	4.01	4.12	3.46	3.70
GWo-GGA	-	4.25	5.36	3.74	4.24
GW	-	-	2.51	3.46	3.70
BSE	-	3.13	4.24	3.34	3.74
Other theoretical works					
sX-LDA [11]	-	3.85	4.1		
GW@LDA	-	4.8 [7]			5.5 [30]
U+GW [32]	4^a ; 7.5^b	3.99^a; 4.7^b	4.16^a ; 5.4^b		
GoWo@LDA+U [31]	5.2	3.75			
GWo@LDA+U [31]	5.2	3.76			
Experimental band gap of fcc NiO obtained using UV-Vis spectroscopy					
3.8 [1] ; 3.89-3.92 [3] ; 3.6 [13] ; 3.32 [39] ; 3.65-3.82 [4] ; 3.47-3.86 [9] ; 3.4-3.71 [38] ; 2.10-3.9 [40] ; 3.744-3.867 [5] ; 3.17-3.83 [22] ; 3.35-3.73 [37]					

The results of the RHL NiO with α_{rh} = 33.557^0 structure are found to be much closer to other theoretical and experimental results than those of fcc NiO, as shown in Table 5.4. This difference is attributed to the fact that NiO crystallizes in the NaCl structure in the paramagnetic phase above T_N, while below its T_N, it has a RHL structure, with the type-two AF phase, which is the most stable structure. Table 5.4 further shows that the direct band gap values of 5.36 eV and 4.24 eV obtained from GWo calculations for fcc NiO and RHL NiO, respectively, are greater than those obtained with BSE of 4.24 eV and 3.74 eV, respectively. This study established that the larger the energy band gap, the less adequate is the GWo method. The reason for this poor performance of the GWo method for determining the energy band gap, is that the response function measures the change in the electronic density induced by the external applied potential [16].

The BSE method gave a good description of the size of the energy band gap than GWo and GW, therefore the direct and the indirect band gap values obtained with BSE are taken as more accurate, and are also in good agreement with the available theoretical and experimental results. In general, the band gap values for RHL NiO with α_{rh} = 33.557^0 obtained with different methods were found to be in the same range between 3 eV and 3.8 eV as shown in Figure 5.19.

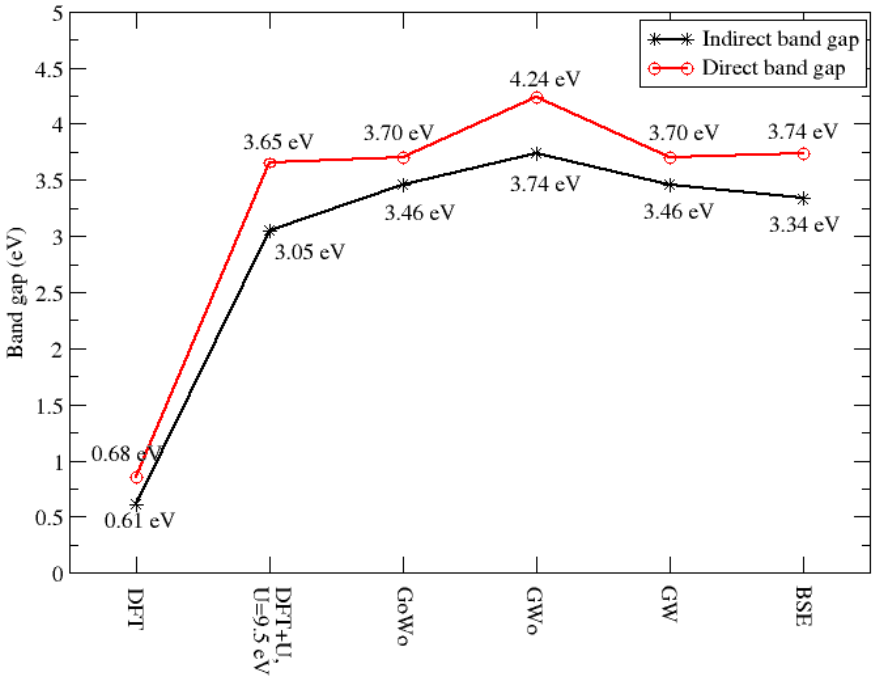

Figure 5.19: Band gap values obtained with DFT, DFT+U, GoWo, GWo, GW and BSE methods for RHL NiO of α_{rh} = 33.557^0.

However, most of the experimental results of the measurement of NiO energy band gap, depend on the preparation techniques, the analysis methods used as seen in Table 2.2, and also the nature of NiO thin films, i.e whether polycrystalline or noncrystalline, etc. As such, some of the variations observed between the calculated values of the energy band gaps and the experimental values could be attributed to these reasons.

CHAPTER SIX

CONCLUSION AND RECOMMENDATIONS

6.1 Conclusion

In this study, the structural, electronic, magnetic and optical properties of bulk NiO have been investigated and compared to the available theoretical and experimental findings. The ground-state properties of rhombohedral (RHL) NiO with α_{rh} = 60.08^0 and RHL NiO with angle α_{rh} = 33.557^0 have been studied with LSDA and LSDA+U approaches, using different values of Hubbard interaction of 5.4 eV, 6.2 eV, 7.3 eV, 8 eV, 8.5 eV, 9 eV, 9.5 eV, 10 eV and 12 eV. The first four U term values have been determined previously by other workers with LCAO, FLAPW, LAPW and LMTO methods, respectively, while the other values have been taken randomly, in order to analyze the properties of NiO. This study found a U value of 9.5 eV predicting the properties of NiO well.

Using those values, the LSDA+U approach has been found to give a better description of the ground-state properties than LSDA. The lattice parameter of NiO was found to increase with increasing U term, whereas the bulk modulus value decreased instead. The lattice parameters and bulk modulus of RHL NiO with α_{rh} = 60.08^0 were found to be 6.716 a.u and 170.3 GPa, respectively, for a calculation without a U term, whereas they were found to be 9.652 a.u and 224.5 GPa, respectively, for RHL NiO with α_{rh} = 33.557^0, for the U term of 9.5 eV. The bond angle Ni-O-Ni and O-Ni-O within LSDA and LSDA+U calculations was a constant value of 90 degrees for RHL NiO with α_{rh} = 33.557^0, while the Ni-O bond length value was increasing with U term, from 3.841 a.u for LSDA, to 3.940 a.u with inclusion of U term of 9.5 eV.

LSDA+U did not describe correctly the electronic properties of RHL NiO with α_{rh} = 60.08^0, as it predicted the material to be metallic. This was attributed to its short lattice constant of 6.758 a.u. However, LSDA+U had a better description of the band gap than LSDA for RHL NiO with α_{rh} = 33.557^0. For the LSDA calculations, narrow indirect and direct band gaps of 0.61 eV and 0.85 eV, were obtained respectively. When a U term was added in the calculations, it opened both the indirect and the direct band gaps up to

3.05 eV and 3.65 eV, respectively, for U term of 9.5 eV. The PDOS for RHL NiO with α_{rh} = 33.557^0 showed a mixed character of Ni 3d and O 2p states within the valence band, but was mainly dominated by an appreciable amount of Ni 3d states. The upper edge of the valence band was dominated by O 2p orbitals whereas the bottom of the conduction band was occupied by Ni 3d down states. Thus, LSDA+U predicted NiO to be a charge transfer insulator which is in good agreement with other previous theoretical and experimental works.

The magnetic properties of bulk RHL NiO with α_{rh} = 33.557^0 and bulk RHL α_{rh} = 60.08^0, were studied by assuming the two Ni atoms to have opposite starting magnetizations, in order to consider its AF state. This study established that RHL NiO is indeed a type two AF material.

The optical properties of fcc NiO and RHL NiO with α_{rh} = 33.557^0 were investigated with GW and BSE methods. From the absorption spectra and electron energy loss (EEL) spectra for fcc NiO, both the fundamental direct and indirect band gaps were found to be 4.25 eV and 5.36 eV, respectively, using GWo calculations, while with BSE, the optical direct and indirect band gaps were found to shift to 3.13 eV and 4.24 eV, respectively. For RHL NiO with α_{rh} = 33.557^0, the absorption spectra and EEL spectra obtained using GWo, have shown the fundamental direct and indirect band gaps to be 3.74 eV and 4.24 eV, respectively. The BSE approach was found to give better prediction of the optical energy band gap of RHL NiO with α_{rh} = 33.557^0. Both the optical direct and indirect band gap values of 3.34 eV and 3.74 eV, respectively, obtained using BSE were found to be closer to the available theoretical and experimental band gap values of NiO. Using the absorption spectrum obtained with BSE, it was found that there is minimal absorption in the range of the infrared to the visible region and stronger absorption towards the ultraviolet region, since the maximum light absorbed by NiO was in the ultraviolet wavelength region near 330 nm. This makes NiO (fcc and RHL with α_{rh} = 33.557^0) a good absorber in the ultraviolet region of the electromagnetic spectrum.

6.2 Recommendations for future studies

This study dealt with bulk NiO ground-state properties using LSDA and LSDA+U approaches, while the optical properties of fcc NiO and RHL NiO were investigated using GW and BSE methods.

There is need for further studies of the properties of this material using other methods used for Many Body Perturbation Theory (MBPT) applied to strongly-correlated materials such as Quantum Monte Carlo (QMC) and Dynamical Mean Field Theory (DMFT) methods.

It would be also interesting to investigate the ground-state properties and optical properties of the surfaces of NiO, and determine the transmittance and reflectivity of NiO as the NiO thin-films are intensively used in solar energy applications.

REFERENCES

[1] Kalam A., Al-Sehemi A. G., Al-Shihri A. S., Du G., and Ahmad T., "Synthesis and characterization of NiO nanoparticles by thermal decomposition of nickel linoleate and their optical properties," *Materials Characterization*, vol. 68, pp. 77–81, (2012).

[2] Forti M., Alonso P., Gargano P., and Rubiolo G., "Transition metals monoxides. An LDA+U study," *Procedia Materials Science*, vol. 1, pp. 230–234, (2012).

[3] Anandan K. and Rajendran V., "Structural, optical and magnetic properties of well-dispersed NiO nanoparticles synthesized by CTAB assisted solvothermal process," *Nanoscience and Nanotechnology: An International Journal*, vol. 2, no. 4, pp. 24–29, (2012).

[4] Reddy A. M., Reddy A. S., Lee K.-S., and Reddy P. S., "Effect of oxygen partial pressure on the structural, optical and electrical properties of sputtered NiO films," *Ceramics International*, vol. 37, no. 7, pp. 2837–2843, (2011).

[5] Sawaby A., Selim M., Marzouk S., Mostafa M., and Hosny A., "Structure, optical and electrochromic properties of NiO thin films," *Physica B: Condensed Matter*, vol. 405, no. 16, pp. 3412–3420, (2010).

[6] Kang T. D., Lee H. S., and Lee H., "Optical properties of black NiO and CoO single crystals studied with spectroscopic ellipsometry," *Journal-Korean Physical Society*, vol. 50, no. 3, p. 632, (2007).

[7] Faleev S. V., van Schilfgaarde M., and Kotani T., "All-electron self-consistent GW Approximation: Application to Si, MnO, and NiO," *Physical review letters*, vol. 93, no. 12, p. 126406, (2004).

[8] Chen H.-L., Lu Y.-M., and Hwang W.-S., "Characterization of sputtered NiO thin films," *Surface and Coatings Technology*, vol. 198, no. 1, pp. 138–142, (2005).

[9] Patil V., Pawar S., Chougule M., Godse P., Sakhare R., Sen S., and Joshi P., "Effect of annealing on structural, morphological, electrical and optical studies of nickel ox-

ide thin films," *Journal of Surface Engineered Materials and Advanced Technology*, vol. 1, pp. 35–41, (2011).

[10] Mironova-Ulmane N., Kuzmin A., Sildos I., and Pärs M., "Polarisation dependent Raman study of single-crystal nickel oxide," *Central European Journal of Physics*, vol. 9, no. 4, pp. 1096–1099, (2011).

[11] Gillen R. and Robertson J., "Accurate screened exchange band structures for the transition metal monoxides MnO, FeO, CoO and NiO," *Journal of Physics: Condensed Matter*, vol. 25, no. 16, p. 165502, (2013).

[12] Liu L., Li X., Liu J., Jiang S., Li Y., Shen G., Mao H., Bi Y., and Xu J., "High pressure structural and elastic properties of NiO up to 67 GPa," *Journal of Applied Physics*, vol. 104, no. 11, pp. 113521–113521, (2008).

[13] Mohanty P., Rath C., Mallick P., Biswal R., and Mishra N., "UV–visible studies of nickel oxide thin film grown by thermal oxidation of nickel," *Physica B: Condensed Matter*, vol. 405, no. 12, pp. 2711–2714, (2010).

[14] Deslippe J. and Louie S. G., "Ab initio theories of the structural, electronic, and optical properties of semiconductors," in *Bulk Crystals to Nanostructures.*, pp. 42–74, Elsevier, (2011).

[15] Giannozzi P., Baroni S., Bonini N., Calandra M., Car R., Cavazzoni C., Ceresoli D., Chiarotti G. L., Cococcioni M., Dabo I., Dal Corso A., de Gironcoli S., Fabris S., Fratesi G., Gebauer R., Gerstmann U., Gougoussis C., Kokalj A., Lazzeri M., Martin-Samos L., Marzari N., Mauri F., Mazzarello R., Paolini S., Pasquarello A., Paulatto L., Sbraccia C., Scandolo S., Sclauzero G., Seitsonen A. P., Smogunov A., Umari P., and Wentzcovitch R. M., "QUANTUM ESPRESSO: a modular and open-source software project for quantum simulations of materials," *Journal of Physics: Condensed Matter*, vol. 21, no. 39, p. 395502, (2009).

[16] Marini A., Hogan C., Grüning M., and Varsano D., "Yambo: An ab initio tool

for excited state calculations," *Computer Physics Communications*, vol. 180, no. 8, pp. 1392–1403, (2009).

[17] Tran F. and Blaha P., "Accurate band gaps of semiconductors and insulators with a semilocal exchange-correlation potential," *Physical review letters*, vol. 102, no. 22, p. 226401, (2009).

[18] Anisimov V. I., Aryasetiawan F., and Lichtenstein A., "First-principles calculations of the electronic structure and spectra of strongly correlated systems: the LDA+ U method," *Journal of Physics: Condensed Matter*, vol. 9, no. 4, p. 767, (1997).

[19] Cococcioni M. and de Gironcoli S., "Linear response approach to the calculation of the effective interaction parameters in the LDA+ U method," *Physical Review B*, vol. 71, no. 3, p. 035105, (2005).

[20] Dudarev S., Botton G., Savrasov S., Humphreys C., and Sutton A., "Electron-energy-loss spectra and the structural stability of nickel oxide: An LSDA+ U study," *Physical Review B*, vol. 57, no. 3, pp. 1505–1509, (1998).

[21] Pickett W., Erwin S., and Ethridge E., "Reformulation of the LDA+ U method for a local-orbital basis," *Physical Review B*, vol. 58, no. 3, p. 1201, (1998).

[22] Mahmoud S. A., Alshomer S., and Mou'ad A., "Structural and optical dispersion characterisation of sprayed nickel oxide thin films," *Journal of Modern Physics*, vol. 2, pp. 1178–1186, (2011).

[23] Cai T., Han H., Yu Y., Gao T., Du J., and Hao L., "Study on the ground state of NiO: The LSDA (GGA)+ U method," *Physica B: Condensed Matter*, vol. 404, no. 1, pp. 89–94, (2009).

[24] Mahmoud S., Akl A., Kamal H., and Abdel-Hady K., "Opto-structural, electrical and electrochromic properties of crystalline nickel oxide thin films prepared by spray pyrolysis," *Physica B: Condensed Matter*, vol. 311, no. 3, pp. 366–375, (2002).

[25] Zhang W., Hu Y., and Tang B., "Phase stability and structural distortion of NiO under high pressure," *Trans. Nonferrous Met. SOC. China*, vol. 16, no. B01, pp. 52–58, (2006).

[26] Misra G., Tripathi P., and Goyal S., "Bulk modulus of semiconductors and its pressure derivatives," *Philosophical magazine letters*, vol. 87, no. 6, pp. 393–401, (2007).

[27] Hugel J. and Kamal M., "Electronic ground state of MnO, FeO, CoO and NiO within the LSDA+ U approximation," *Solid state communications*, vol. 100, no. 7, pp. 457–461, (1996).

[28] Bengone O., Alouani M., Hugel J., and Blochl P., "LDA+U calculated electronic and structural properties of NiO(001) and NiO (111) p(2x2) surfaces.," *Computational Materials Science*, vol. 24, pp. 192–198, (2002).

[29] Wei P. and Qi Z. Q., "Insulating gap in the transition-metal oxides: A calculation using the local-spin-density approximation with the on-site coulomb U correlation correction," *Physical Review B*, vol. 49, no. 16, p. 10864, (1994).

[30] Aryasetiawan F. and Gunnarsson O., "Electronic structure of NiO in the GW approximation," *Physical review letters*, vol. 74, no. 16, p. 3221, (1995).

[31] Jiang H., Gomez-Abal R. I., Rinke P., and Scheffler M., "First-principles modeling of localized d states with the G W@ LDA+ U approach," *Physical Review B*, vol. 82, no. 4, p. 045108, (2010).

[32] Kobayashi S., Nohara Y., Yamamoto S., and Fujiwara T., "GW approximation with LSDA+ U method and applications to NiO, MnO, and V_2O_3," *Physical Review B*, vol. 78, no. 15, p. 155112, (2008).

[33] Muscat J., Wander A., and Harrison N., "On the prediction of band gaps from hybrid functional theory," *Chemical Physics Letters*, vol. 342, no. 3, pp. 397–401, (2001).

[34] Fujimori A. and Mizokawa T., "Electronic structure of transition-metal oxides," *Current Opinion in Solid State and Materials Science*, vol. 2, no. 1, pp. 18–22, (1997).

[35] Lee G. and Oh S.-J., "Electronic structures of NiO, CoO, and FeO studied by 2p core-level X-ray photoelectron spectroscopy," *Physical Review B*, vol. 43, no. 18, p. 14674, (1991).

[36] Sugiyama I., Shibata N., Wang Z., Kobayashi S., Yamamoto T., and Ikuhara Y., "Ferromagnetic dislocations in antiferromagnetic NiO," *Nature nanotechnology*, vol. 8, no. 4, pp. 266–270, (2013).

[37] Sriram S., Balu A., and Thayumanavan A., "Design and development of automated liquid flow deposition method for thin film formation," *Archives of Applied Science Research*, vol. 3, no. 2, pp. 438–447, (2011).

[38] Guziewicz M., Grochowski J., Borysiewicz M., Kaminska E., Domagala J. Z., Rzodkiewicz W., Witkowski B. S., Golaszewska K., Kruszka R., Ekielski M., and Piotrowska A., "Electrical and optical properties of NiO films deposited by magnetron sputtering," *Optica Applicata*, vol. 41, no. 2, pp. 431–440, (2011).

[39] Jiang D., Qin J., Wang X., Gao S., Liang Q., and Zhao J., "Optical properties of NiO thin films fabricated by electron beam evaporation," *Vacuum*, vol. 86, no. 8, pp. 1083–1086, (2012).

[40] Ezema F., Ekwealor A., and Osuji R., "Optical properties of chemical bath deposited nickel oxide (NiOx) thin films," *Superficies Vacio*, vol. 21, no. 1, pp. 6–10, (2008).

[41] Al-Ghamdi A., Mahmoud W. E., Yaghmour S., and Al-Marzouki F., "Structure and optical properties of nanocrystalline NiO thin film synthesized by sol–gel spin-coating method," *Journal of Alloys and Compounds*, vol. 486, no. 1, pp. 9–13, (2009).

[42] Subramanian B., Mohamed Ibrahim M., Senthilkumar V., Murali K., Vidhya V., Sanjeeviraja C., and Jayachandran M., "Optoelectronic and electrochemical properties of nickel oxide (NiO) films deposited by DC reactive magnetron sputtering," *Physica B: Condensed Matter*, vol. 403, no. 21, pp. 4104–4110, (2008).

[43] Karthik K., Selvan G. K., Kanagaraj M., Arumugam S., and Jaya N. V., "Particle size

effect on the magnetic properties of NiO nanoparticles prepared by a precipitation method," *Journal of Alloys and Compounds*, vol. 509, no. 1, pp. 181–184, (2011).

[44] Tadić M., Panjan M., Marković D., Milošević I., and Spasojević V., "Unusual magnetic properties of NiO nanoparticles embedded in a silica matrix," *Journal of Alloys and Compounds*, vol. 509, no. 25, pp. 7134–7138, (2011).

[45] Ichiyanagi Y., Wakabayashi N., Yamazaki J., Yamada S., Kimishima Y., Komatsu E., and Tajima H., "Magnetic properties of NiO nanoparticles," *Physica B: Condensed Matter*, vol. 329, pp. 862–863, (2003).

[46] Bi H., Li S., Zhang Y., and Du Y., "Ferromagnetic-like behavior of ultrafine NiO nanocrystallites," *Journal of magnetism and magnetic materials*, vol. 277, no. 3, pp. 363–367, (2004).

[47] Ren X., Leonov I., Keller G., Kollar M., Nekrasov I., and Vollhardt D., "LDA+ DMFT computation of the electronic spectrum of NiO," *Physical Review B*, vol. 74, no. 19, p. 195114, (2006).

[48] Deng H.-X., Li J., Li S.-S., Xia J.-B., Walsh A., and Wei S.-H., "Origin of antiferromagnetism in coo: A density functional theory study," *Applied Physics Letters*, vol. 96, no. 16, p. 162508, (2010).

[49] Santra B., *Density-Functional Theory Exchange-Correlation Functionals for Hydrogen Bonds in Water.* PhD thesis, Fritz-Haber-Insitut der Max-Planck-Gesellschaft, Berlin, Germany, (2010).

[50] Cococcioni M. and de Gironcoli S., *A LDA+ U study of selected iron compounds*. PhD thesis, SISSA, Italy, (2002).

[51] Woodruff D., "Clean oxide surfaces: a theoretical review," *Oxide Surfaces*, p. 35, (2001).

[52] Godby R. W. and García-González P., "Density functional theories and self-energy

approaches," in *A Primer in Density Functional Theory*, pp. 185–217, Springer, (2003).

[53] Khon W. and Sham L., "Self-consistent equations including exchange and correlation effects," *Phys. Rev*, vol. 140, no. 4A, pp. A1133–A1138, (1965).

[54] Hua X., Chen X., and Goddard W., "Generalized generalized gradient approximation: An improved density-functional theory for accurate orbital eigenvalues," *Physical Review B*, vol. 55, no. 24, p. 16103, (1997).

[55] Foster A. S., *Theoretical modelling of non-contact atomic force microscopy on insulators.* PhD thesis, University College London (University of London), (2000).

[56] Perdew J. P., Burke K., and Wang Y., "Generalized gradient approximation for the exchange-correlation hole of a many-electron system," *Physical Review B*, vol. 54, no. 23, p. 16533, (1996).

[57] Hafner J., "Ab-initio simulations of materials using VASP: Density-functional theory and beyond," *Journal of computational chemistry*, vol. 29, no. 13, pp. 2044–2078, (2008).

[58] Ren X., *LDA + DMFT Investigation of NiO.* PhD thesis, University of Augsburg, Germany, (2005).

[59] Wang L., Maxisch T., and Ceder G., "Oxidation energies of transition metal oxides within the GGA+ U framework," *Physical Review B*, vol. 73, no. 19, p. 195107, (2006).

[60] Anisimov V. I., Zaanen J., and Andersen O. K., "Band theory and Mott insulators: Hubbard U instead of Stoner I," *Physical Review B*, vol. 44, no. 3, p. 943, (1991).

[61] Hedin L., "New method for calculating the one-particle green's function with application to the electron-gas problem," *Physical Review*, vol. 139, no. 3A, p. A796, (1965).

[62] Friedrich C. and Schindlmayr A., "Many-body perturbation theory: the GW approximation," *NIC Series*, vol. 31, pp. 335–355, (2006).

[63] Del Sole R., Pulci O., Olevano V., and Marini A., "Many-body perturbation theory combined with time dependent DFT: A new method for the calculation of the dielectric function of solids," *physica status solidi (b)*, vol. 242, no. 13, pp. 2729–2736, (2005).

[64] Madsen G. K. H. and Novák P., "Charge order in magnetite. An LDA+U study," *EPL (Europhysics Letters)*, vol. 69, no. 5, p. 777, (2005).

[65] Kittel C., *Introduction to Solid States Physics*. John Wiley and Son, New York, seven ed., (2002).

[66] Setyawan W. and Curtarolo S., "High-throughput electronic band structure calculations: Challenges and tools," *Computational Materials Science*, vol. 49, no. 2, pp. 299–312, (2010).

[67] Kokalj A., "Xcrysden. A new program for displaying crystalline structures and electron densities," *Journal of Molecular Graphics and Modelling*, vol. 17, no. 3, pp. 176–179, (1999).

[68] Farag A., Obada M. K., and Mahmoud M. E., "Structural and optical evaluations of deposited nanocrystalline NiO thin films via a Ni (II)-8-hydroxyquinolate complex by the static step-by-step soft surface reaction technique for optoelectronic applications," *Polyhedron*, vol. 71, pp. 75–84, (2014).

[69] Yu X., Xie C., Yang L., and Zhang S., "Highly photoactive sensor based on NiO modified TiO2 porous film for diethyl ether," *Sensors and Actuators*, vol. B, no. 195, pp. 439–445, (2014).

[70] Qamar M., Gondal M., and Yamani Z., "Synthesis of nanostructured nio and its application in laser-induced photocatalytic reduction of Cr (VI) from water," *Journal of Molecular Catalysis A: Chemical*, vol. 341, no. 1, pp. 83–88, (2011).

[71] Seeger K., *Semiconductor Physics*. Springer-Verlag, Berlin, eight ed., (2002).

[72] Marinopoulos A., Wirtz L., Marini A., Olevano V., Rubio A., and Reining L., "Optical absorption and electron energy loss spectra of carbon and boron nitride nanotubes: a first-principles approach," *Applied Physics A*, vol. 78, no. 8, pp. 1157–1167, (2004).

[73] Egerton R., "Electron energy-loss spectroscopy in the TEM," *Reports on Progress in Physics*, vol. 72, no. 1, p. 016502, (2009).

[74] Eguiluz A. G., Restrepo O., Larson B. C., Tischler J. Z., Zschack P., and Jellison G., "Electron–hole excitations in NiO: LSDA+ U-based calculations vs. inelastic X-ray scattering and ellipsometry measurements," *Journal of Physics and Chemistry of Solids*, vol. 66, no. 12, pp. 2281–2289, (2005).

APPENDIX A

STRUCTURAL OPTIMIZATIONS

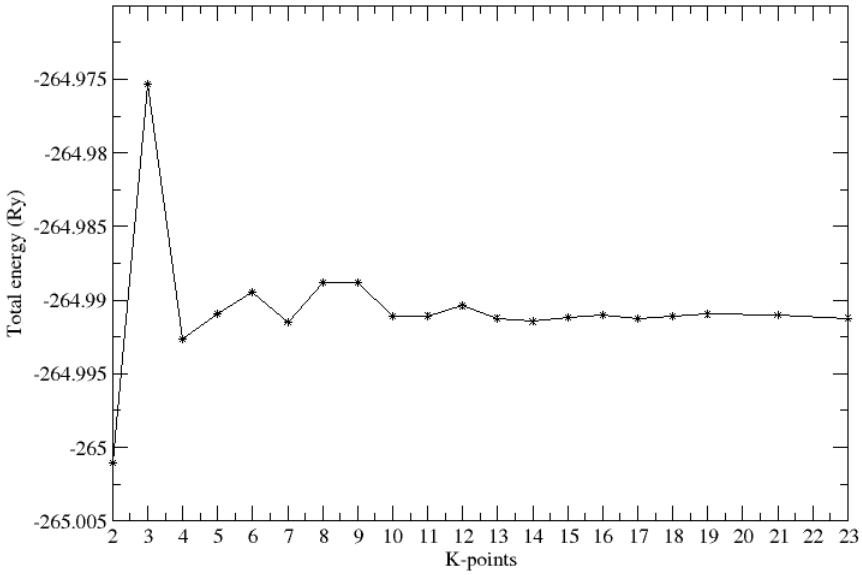

Figure A.1: Optimized k-points for RHL NiO with α_{rh} = 60.08^0.

A converged k-points mesh of $15 \times 15 \times 15$ was considered for RHL NiO with α_{rh} = 60.08^0 since it had a consistent energy for the structure.

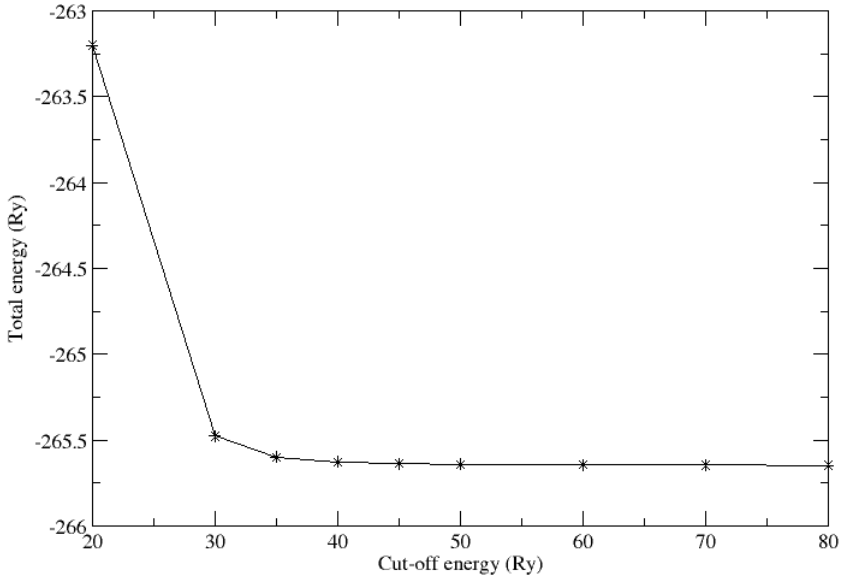

Figure A.2: Optimized plane wave energy cut off for RHL NiO with α_{rh} = 60.08^0.

The plane wave energy cut off of 50 Ry was used for RHL NiO with α_{rh} = 60.08^0 since it had the lowest and consistent energy for the structure.

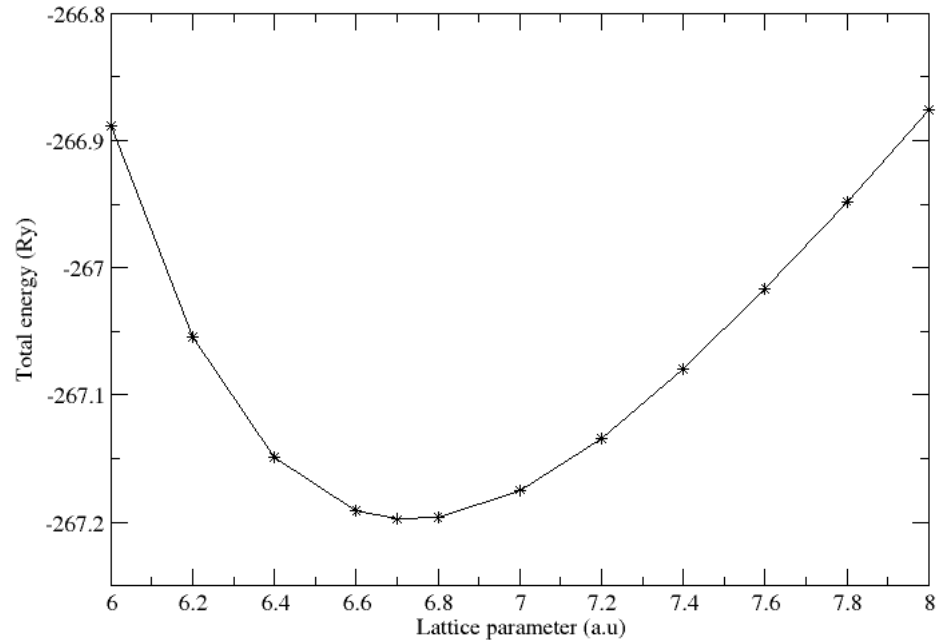

Figure A.3: Optimized lattice constant of RHL NiO with α_{rh} = 60.08^0 using LSDA.

The lattice constant of 6.716 a.u was used as it was found to have the lowest energy for RHL NiO with α_{rh} = 60.08^0, for LSDA calculations without U term.

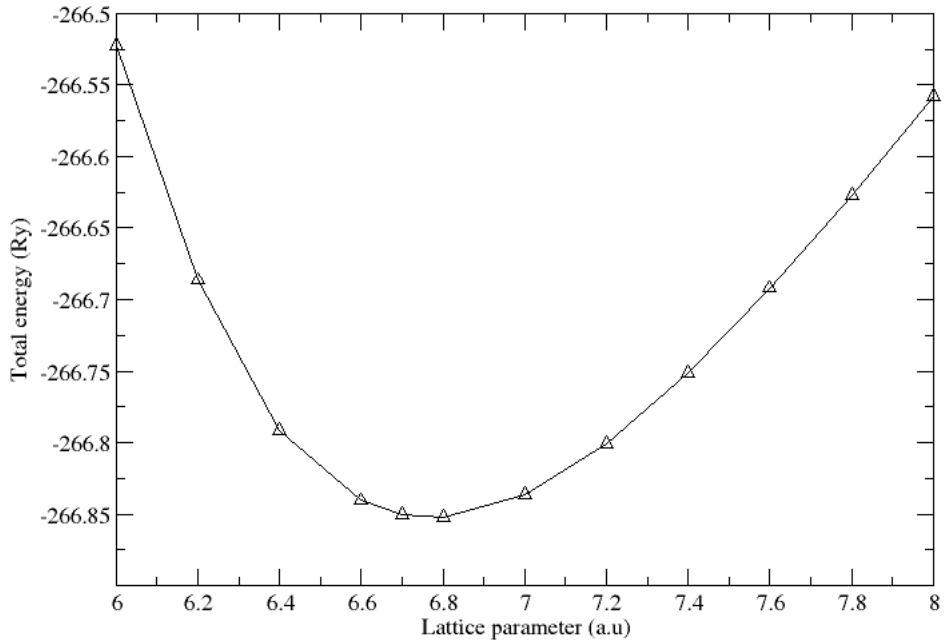

Figure A.4: Optimized lattice constant of RHL NiO with α_{rh} = 60.08^0 using U=5.4 eV.

The lattice constant of 6.785 a.u was used as it was found to have the lowest energy for RHL NiO with α_{rh} = 60.08^0, for LSDA+U calculations with U term of 5.4 eV.

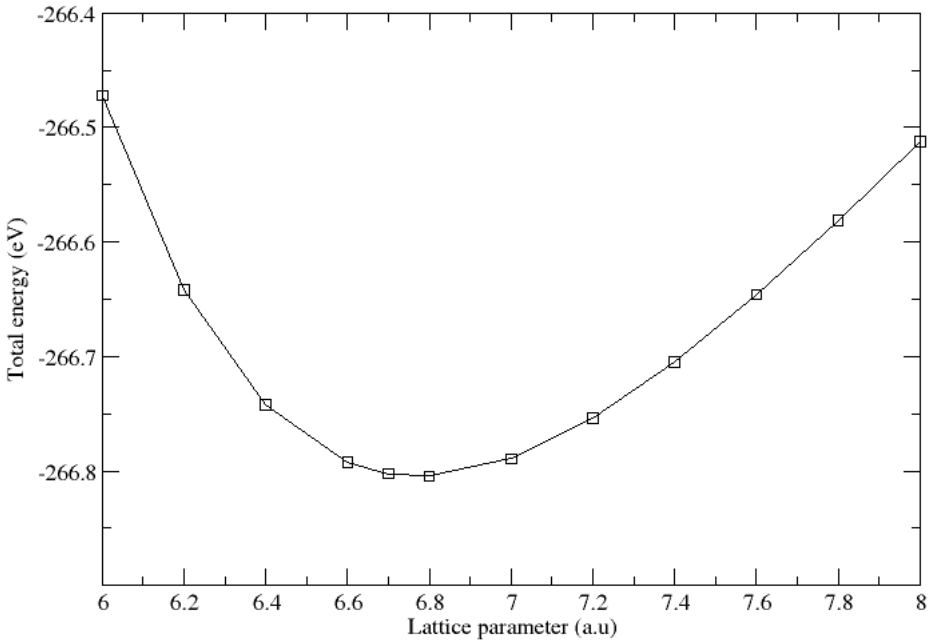

Figure A.5: Optimized lattice constant of RHL NiO with α_{rh} = 60.08^0 using U=6.2 eV.

The lattice constant of 6.786 a.u was used as it was found to have the lowest energy for RHL NiO with α_{rh} = 60.08^0, for LSDA+U calculations with U term of 6.2 eV.

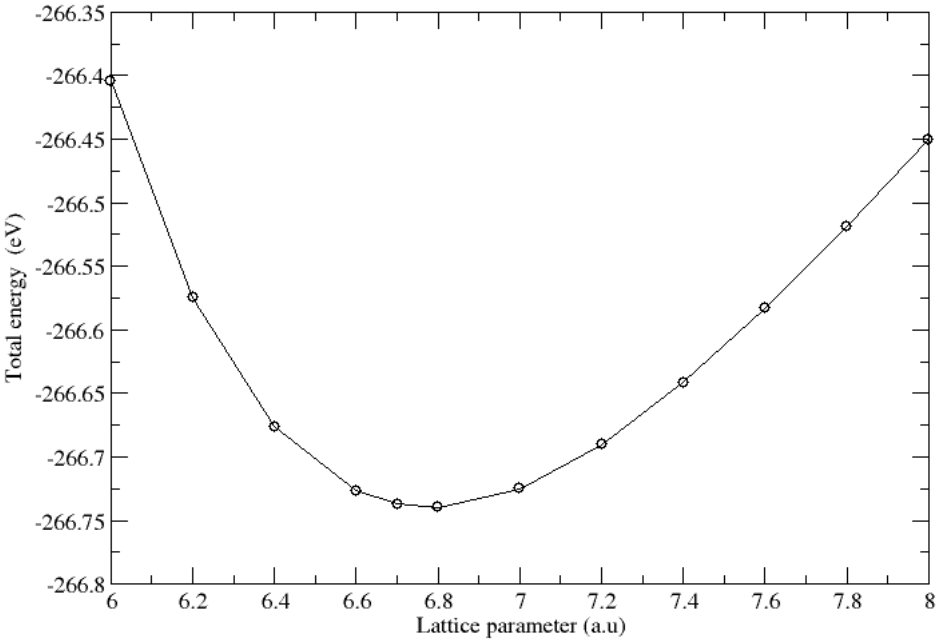

Figure A.6: Optimized lattice constant of RHL NiO with α_{rh} = 60.08^0 using U=7.3 eV.

The lattice constant of 6.789 a.u was used as it was found to have the lowest energy for RHL NiO with α_{rh} = 60.08^0, for LSDA+U calculations with U term of 7.3 eV.

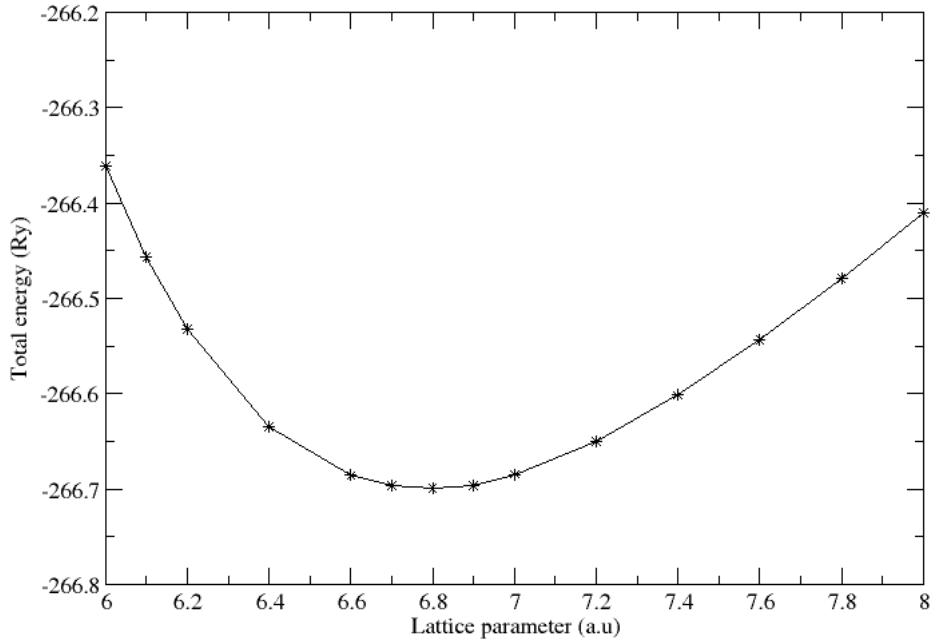

Figure A.7: Optimized lattice constant of RHL NiO with α_{rh} = 60.08^0 using U=8 eV.

The lattice constant of 6.795 a.u was used as it was found to have the lowest energy for RHL NiO with α_{rh} = 60.08^0, for LSDA+U calculations with U term of 8 eV.

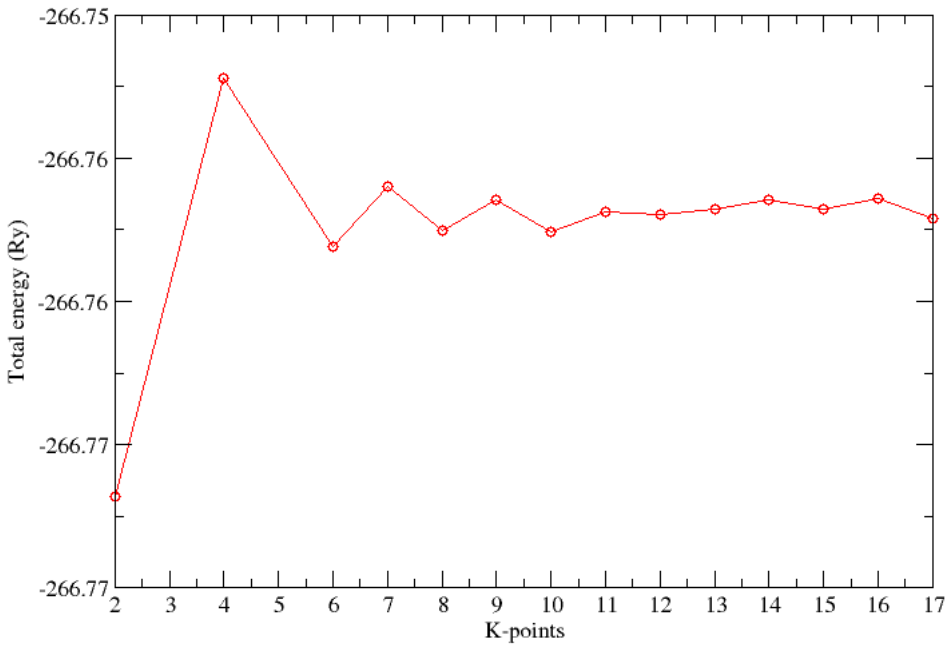

Figure A.8: Optimized k-points for RHL NiO with α_{rh} = 33.557^0 using LSDA.

A converged k-points mesh of 12 × 12 × 12 was considered for RHL NiO with α_{rh} = 33.557^0, using LSDA without U term.

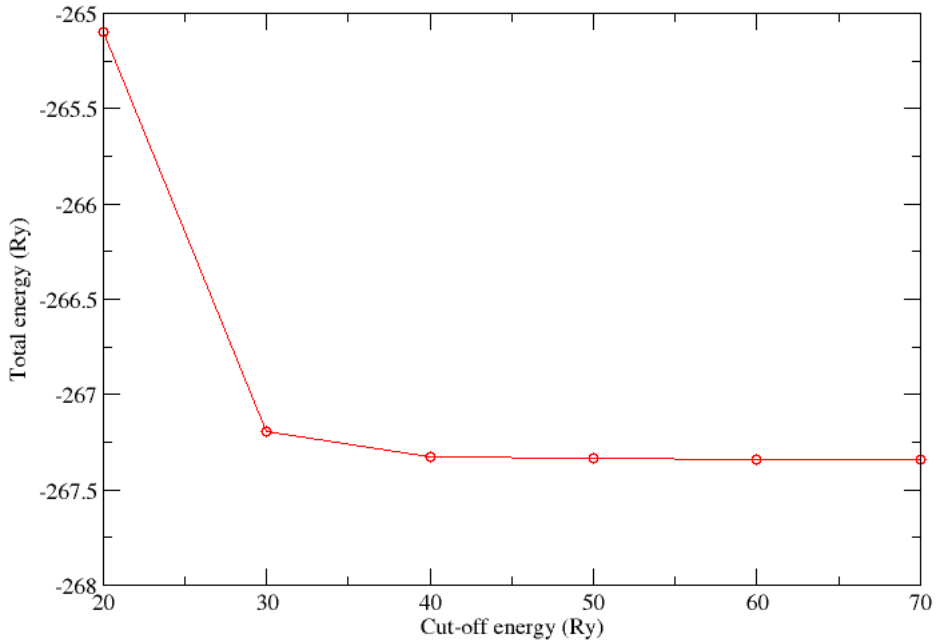

Figure A.9: Optimized plane wave energy cut off for RHL NiO with α_{rh} = 33.557^0 using LSDA.

The plane wave energy cut off of 50 Ry was used for RHL NiO with α_{rh} = 33.557^0 using LSDA without U term, since it had the lowest and consistent energy for the structure.

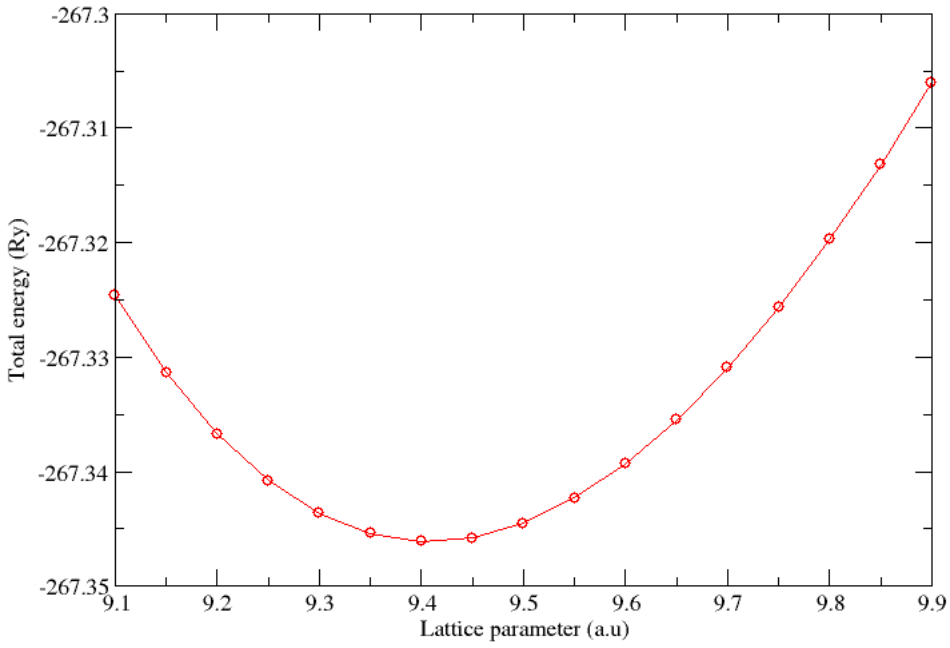

Figure A.10: Optimized lattice constant of RHL NiO with α_{rh} = 33.557^0 using LSDA.

The lattice constant of 9.408 a.u was used since it was found to have the lowest energy for RHL NiO with α_{rh} = 33.557^0 using LSDA without U term.

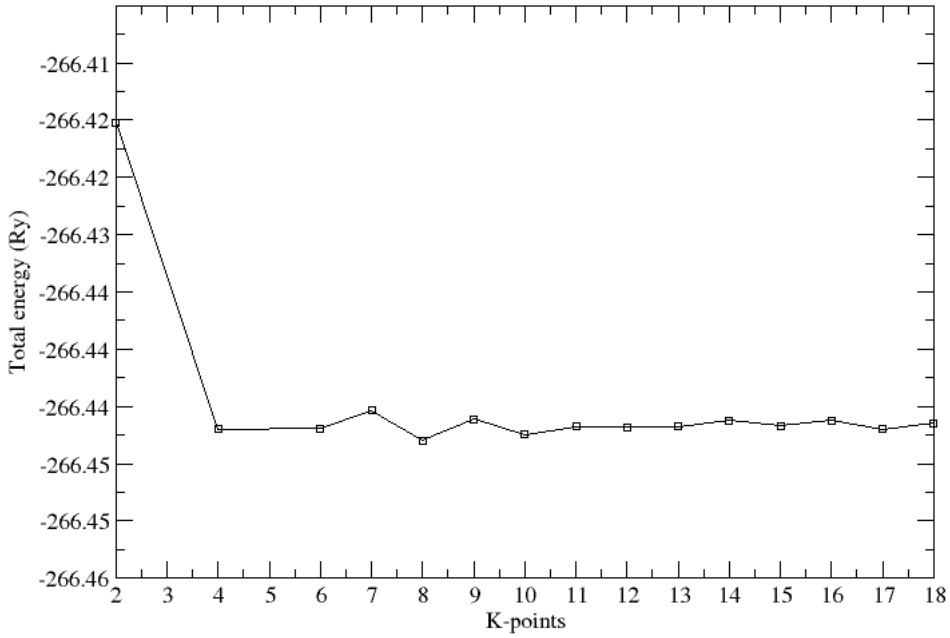

Figure A.11: Optimized k-points for RHL NiO with α_{rh} = 33.557^0 using U=5.4 eV.

A converged k-points mesh of 12 × 12 × 12 was considered for RHL NiO with α_{rh} = 33.557^0, for LSDA+U calculations with U term of 5.4 eV.

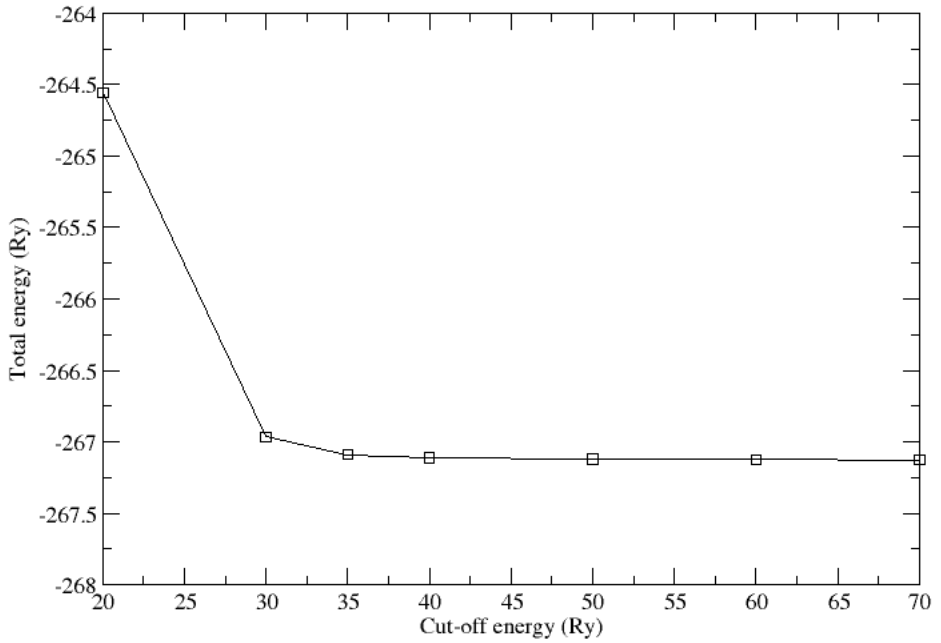

Figure A.12: Optimized plane wave energy cut off for RHL NiO with α_{rh} = 33.557^0 using U=5.4 eV.

The plane wave energy cut off of 50 Ry was used for RHL NiO with α_{rh} = 33.557^0 for LSDA+U calculations with U term of 5.4 eV.

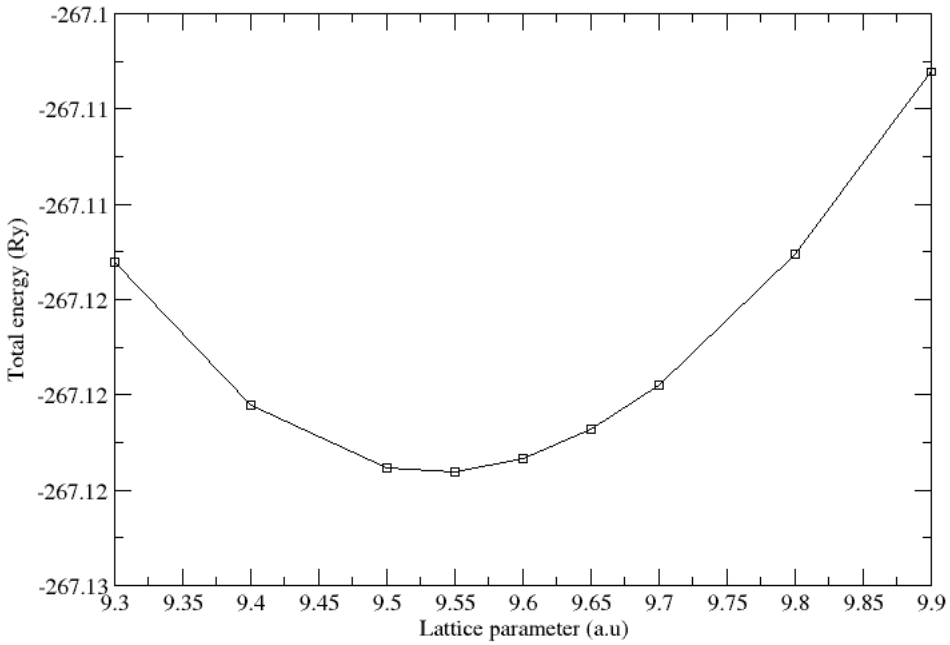

Figure A.13: Optimized lattice constant of RHL NiO with α_{rh} = 33.557^0 using U=5.4 eV.

The lattice constant of 9.536 a.u was used as it was found to have the lowest energy for RHL NiO with α_{rh} = 33.557^0 for LSDA+U calculations with U term of 5.4 eV.

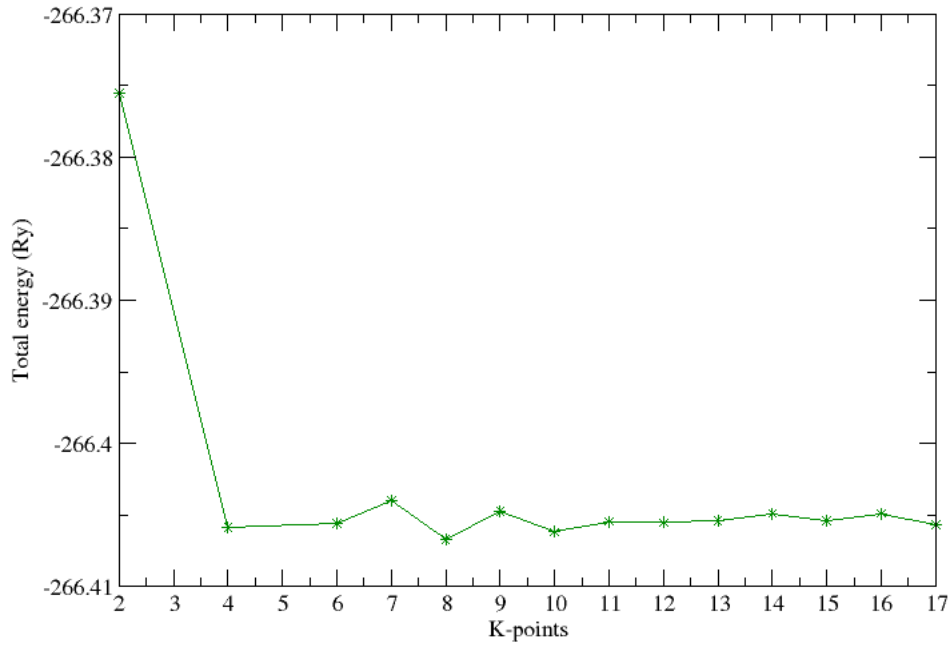

Figure A.14: Optimized k-points for RHL NiO with α_{rh} = 33.557^0 using U=6.2 eV.

A converged k-points mesh of 12 × 12 × 12 was considered for RHL NiO with α_{rh} = 33.557^0, for LSDA+U calculations with U term of 6.2 eV.

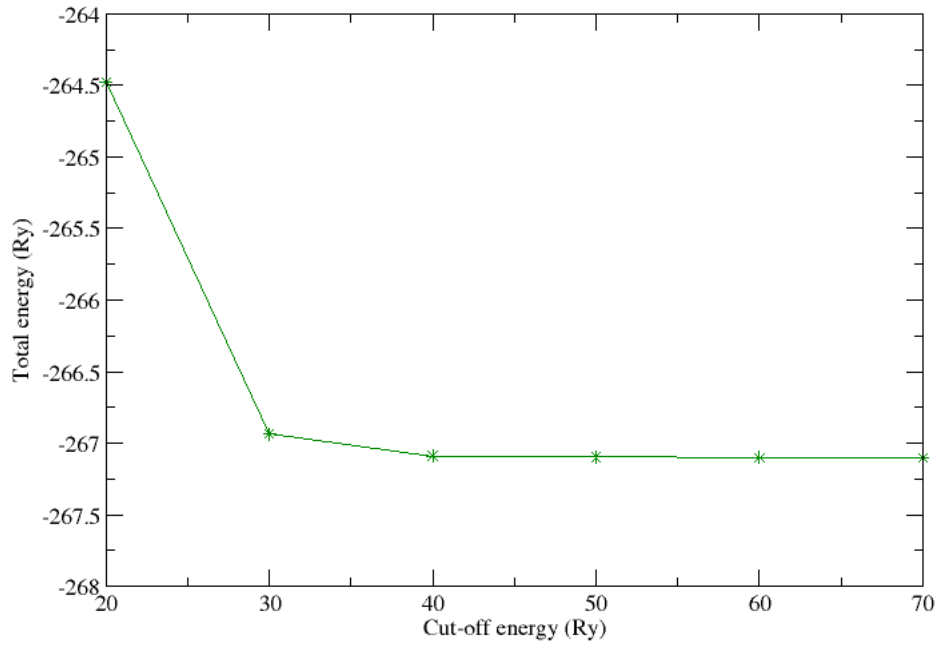

Figure A.15: Optimized plane wave energy cut off for RHL NiO with α_{rh} = 33.557^0 using U=6.2 eV.

The plane wave energy cut off of 50 Ry was used for RHL NiO with α_{rh} = 33.557^0 for LSDA+U calculations with U term of 6.2 eV.

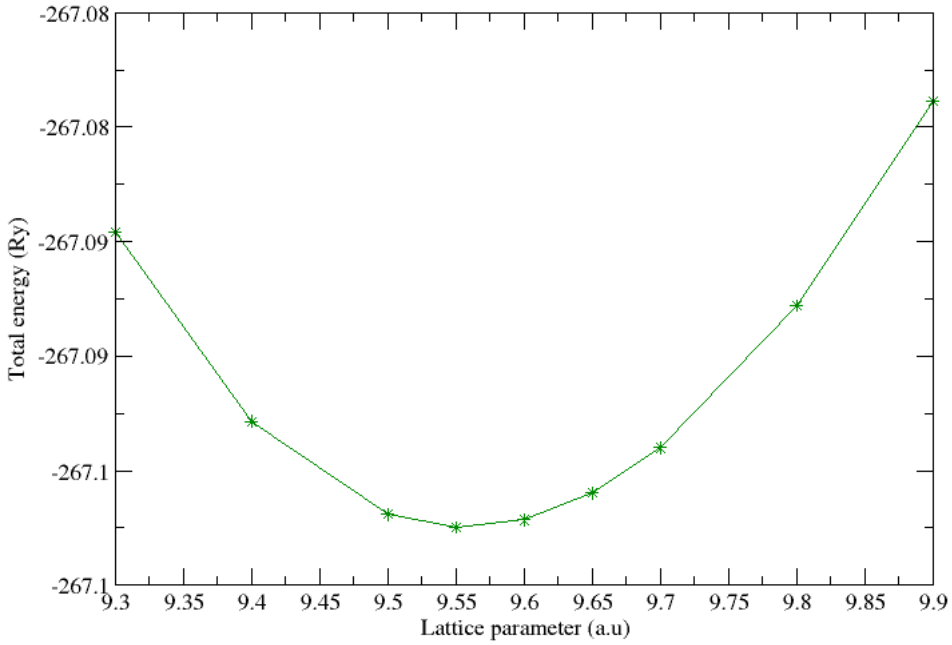

Figure A.16: Optimized lattice constant of RHL NiO with α_{rh} = 33.557^0 using U=6.2 eV.

The lattice constant of 9.556 a.u was used as it was found to have the lowest energy for RHL NiO with α_{rh} = 33.557^0 for LSDA+U calculations with U term of 6.2 eV.

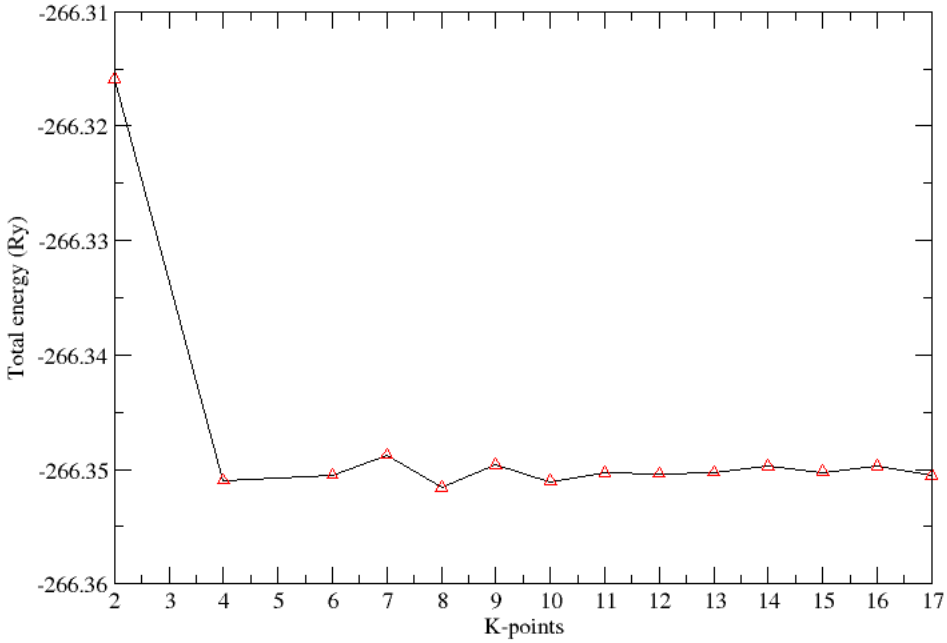

Figure A.17: Optimized k-points for RHL NiO with α_{rh} = 33.557^0 using U=7.3 eV.

A converged k-points mesh of 12 × 12 × 12 was considered for RHL NiO with α_{rh} = 33.557^0, for LSDA+U calculations with U term of 7.3 eV.

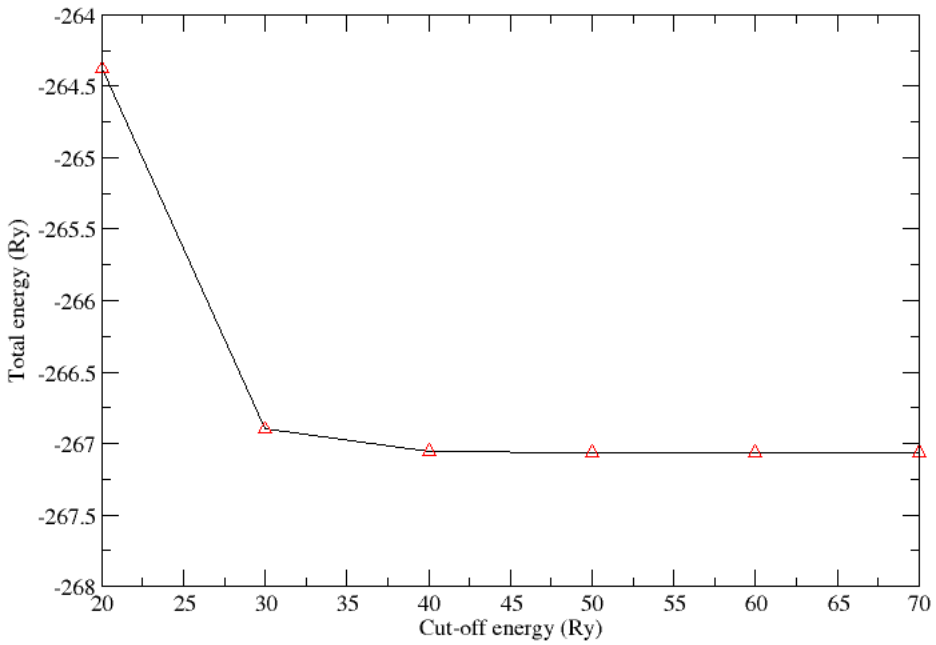

Figure A.18: Optimized plane wave energy cut off for RHL NiO with α_{rh} = 33.557^0 using U=7.3 eV.

The plane wave energy cut off of 50 Ry was used for RHL NiO with α_{rh} = 33.557^0 for LSDA+U calculations with U term of 7.3 eV.

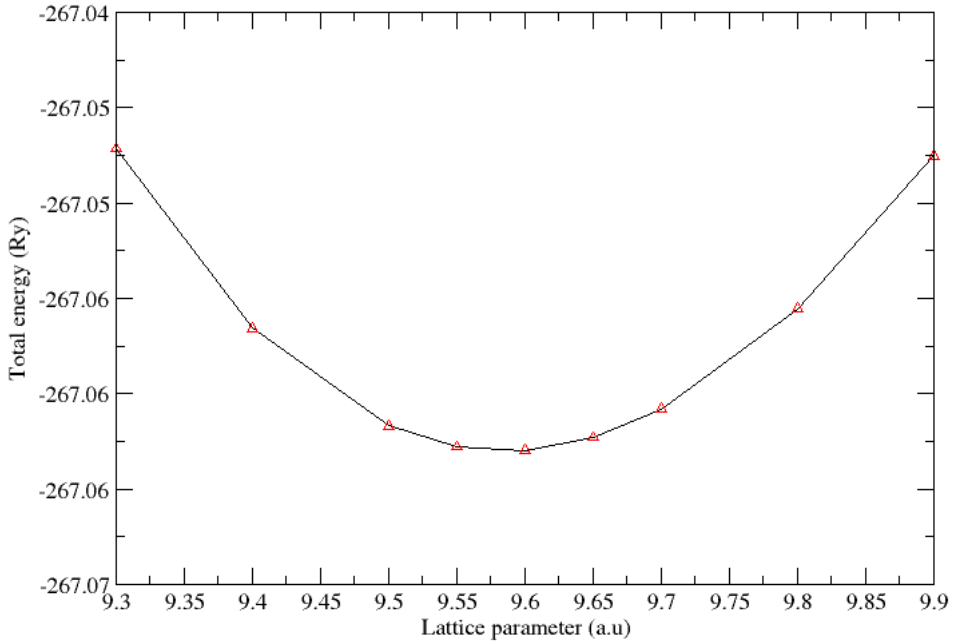

Figure A.19: Optimized lattice constant of RHL NiO with α_{rh} = 33.557^0 using U=7.3 eV.

The lattice constant of 9.586 a.u was used since it was found to have the lowest energy for RHL NiO with α_{rh} = 33.557^0 for LSDA+U calculations with U term of 7.3 eV.

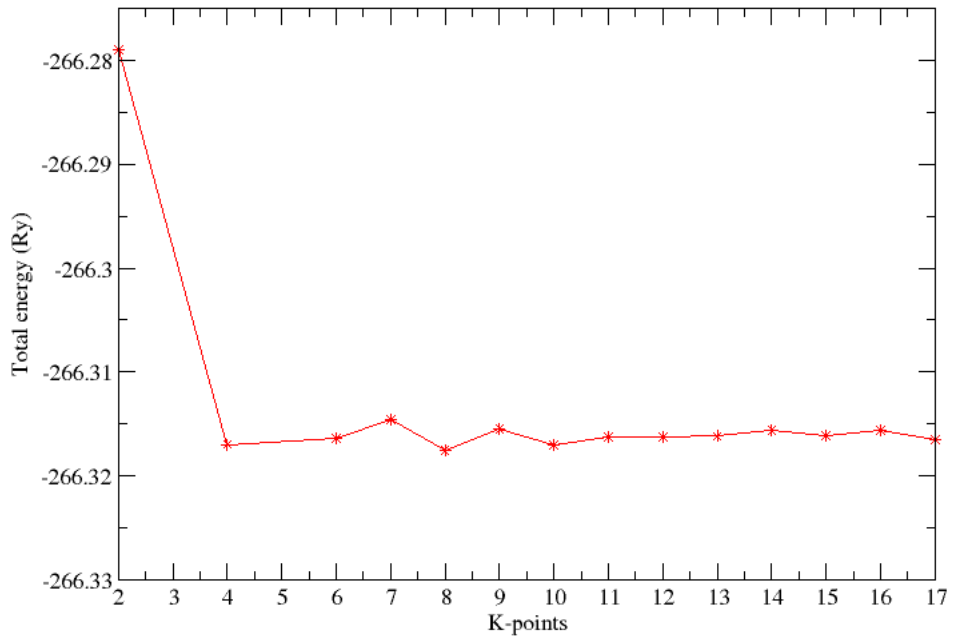

Figure A.20: Optimized k-points for RHL NiO with α_{rh} = 33.557^0 using U=8 eV.

A converged k-points mesh of $12 \times 12 \times 12$ was considered for RHL NiO with α_{rh} = 33.557^0, for LSDA+U calculations with U term of 8 eV.

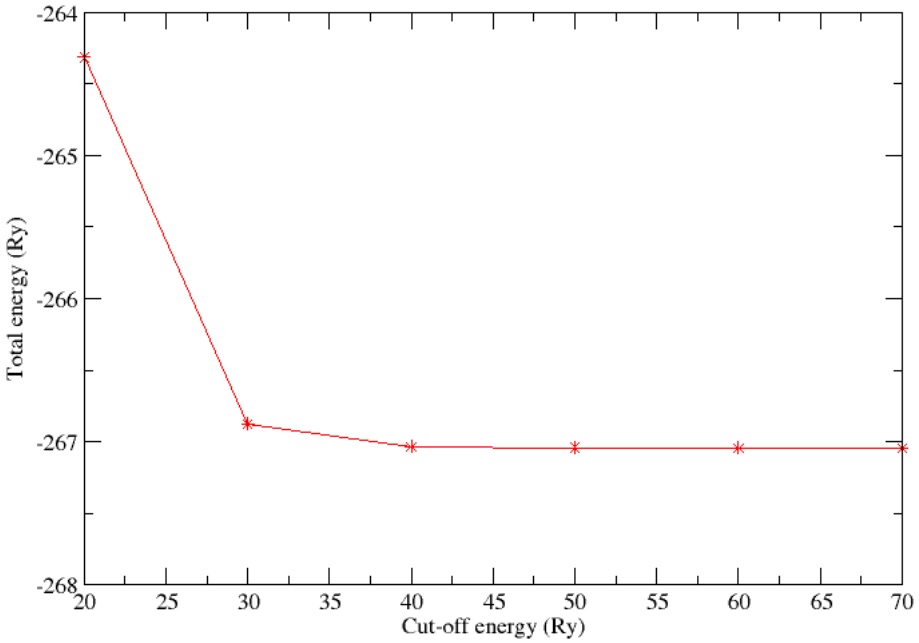

Figure A.21: Optimized plane wave energy cut off for RHL NiO with α_{rh} = 33.557^0 using U=8 eV.

The plane wave energy cut off of 50 Ry was used for RHL NiO with α_{rh} = 33.557^0 for LSDA+U calculations with U term of 8 eV.

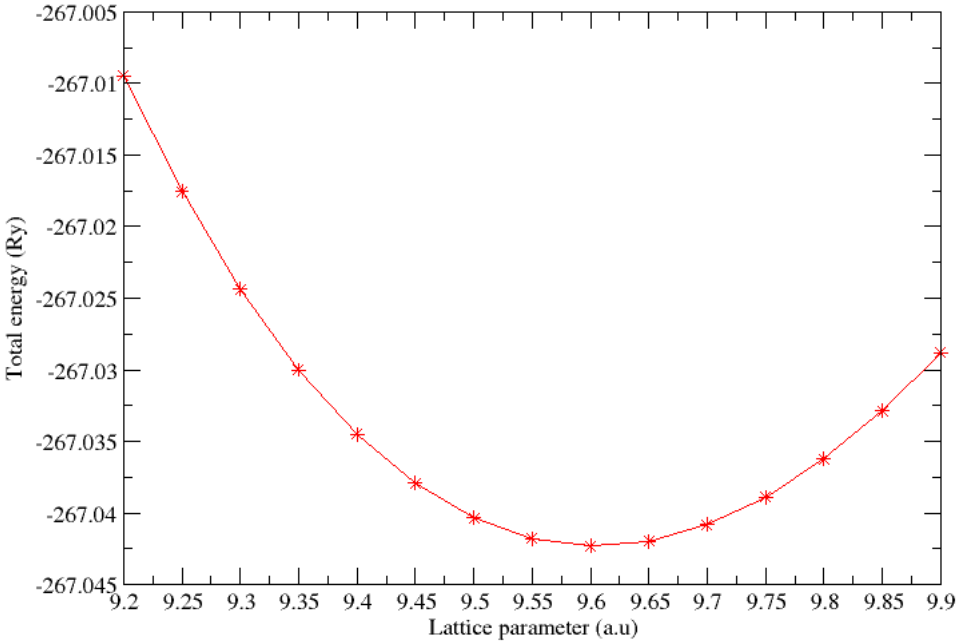

Figure A.22: Optimized lattice constant of RHL NiO with α_{rh} = 33.557^0 using U=8 eV.

The lattice constant of 9.605 a.u was used as it was found to have the lowest energy for RHL NiO with α_{rh} = 33.557^0 for LSDA+U calculations with U term of 8 eV.

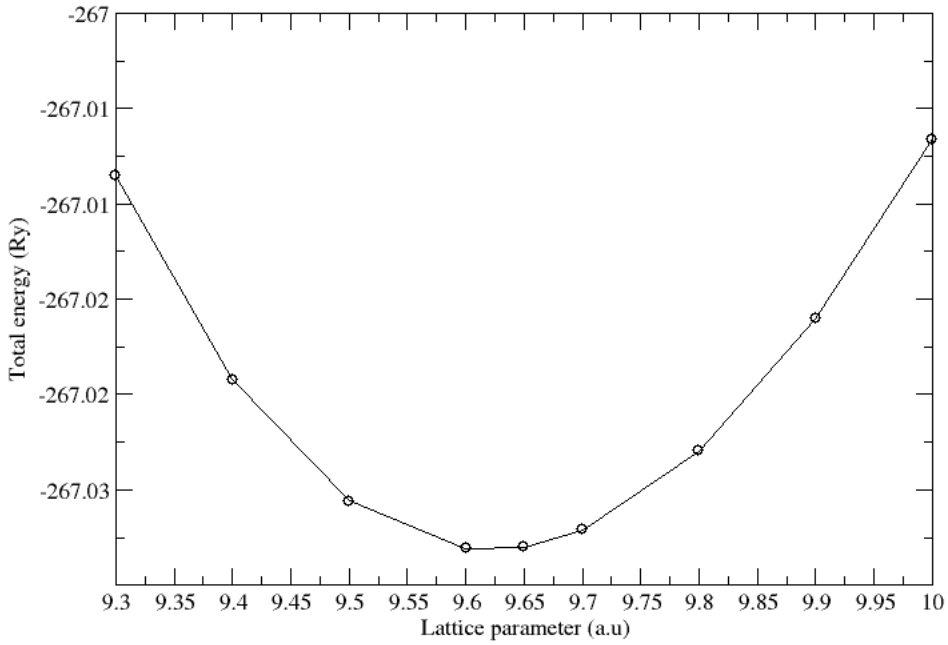

Figure A.23: Optimized lattice constant of RHL NiO with α_{rh} = 33.557^0 using U=8.5 eV.

The lattice constant of 9.620 a.u was used as it was found to have the lowest energy for RHL NiO with α_{rh} = 33.557^0 for LSDA+U calculations with U term of 8.5 eV.

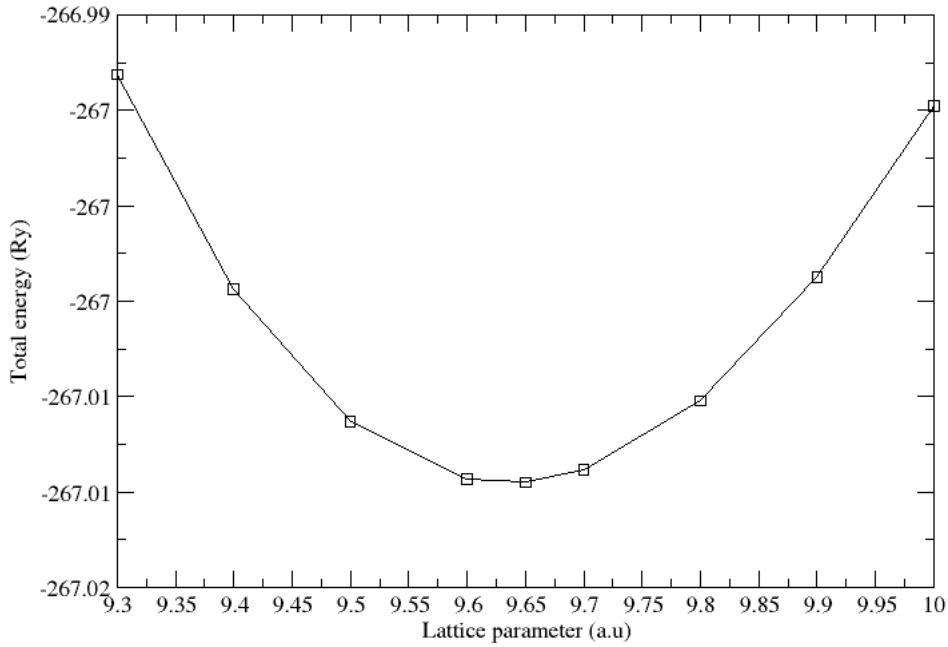

Figure A.24: Optimized lattice constant of RHL NiO with α_{rh} = 33.557^0 using U=9 eV.

The lattice constant of 9.635 a.u was used as it was found to have the lowest energy for RHL NiO with α_{rh} = 33.557^0 for LSDA+U calculations with U term of 9 eV.

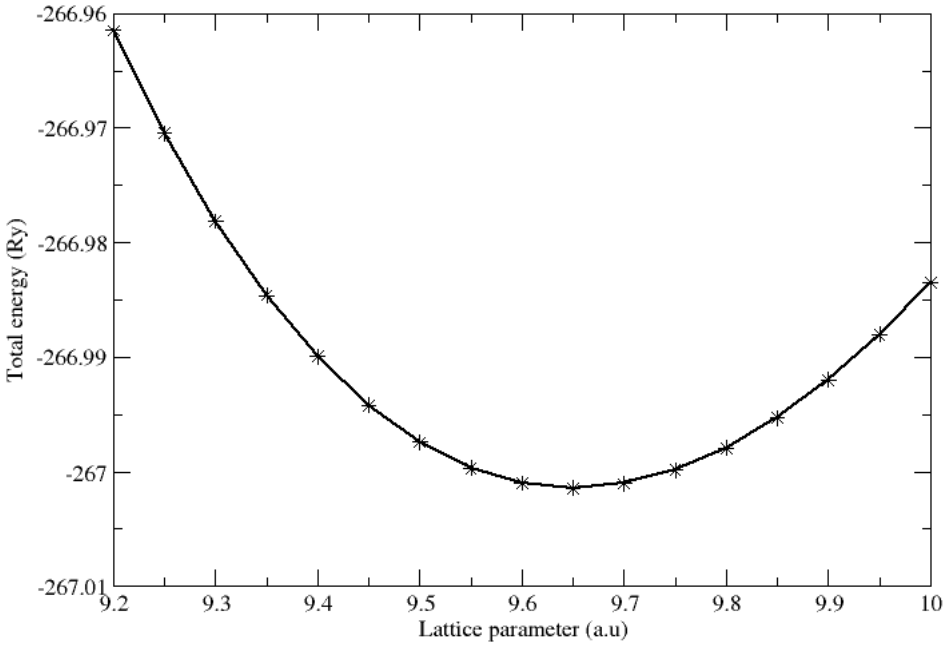

Figure A.25: Optimized lattice constant of RHL NiO with α_{rh} = 33.557^0 using U=9.5 eV.

The lattice constant of 9.652 a.u was used as it was found to have the lowest energy for RHL NiO with α_{rh} = 33.557^0 for LSDA+U calculations with U term of 9.5 eV.

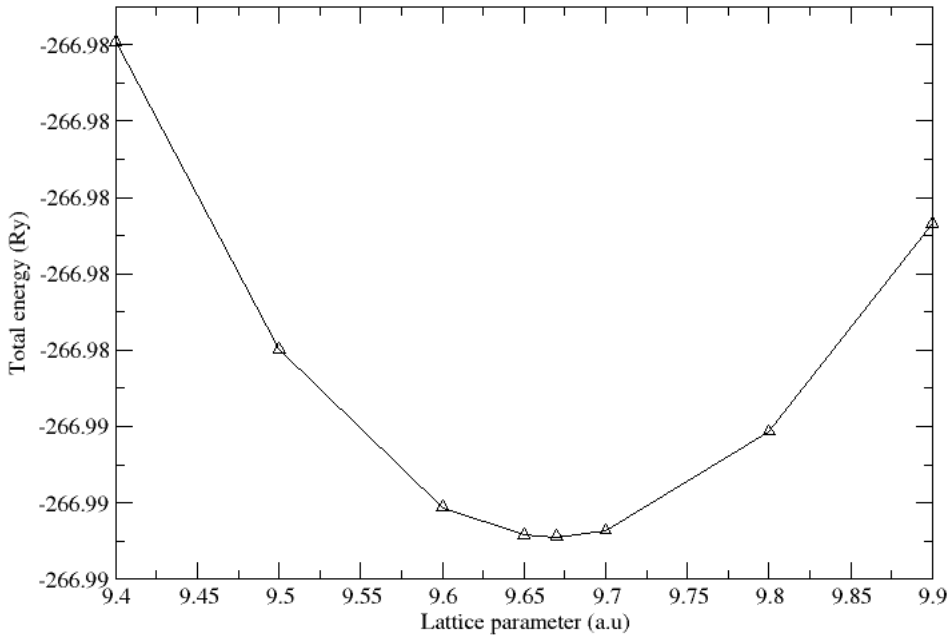

Figure A.26: Optimized lattice constant of RHL NiO with α_{rh} = 33.557^0 using U=10 eV.

The lattice constant of 9.668 a.u was used as it was found to have the lowest energy for RHL NiO with α_{rh} = 33.557^0 for LSDA+U calculations with U term of 10 eV.

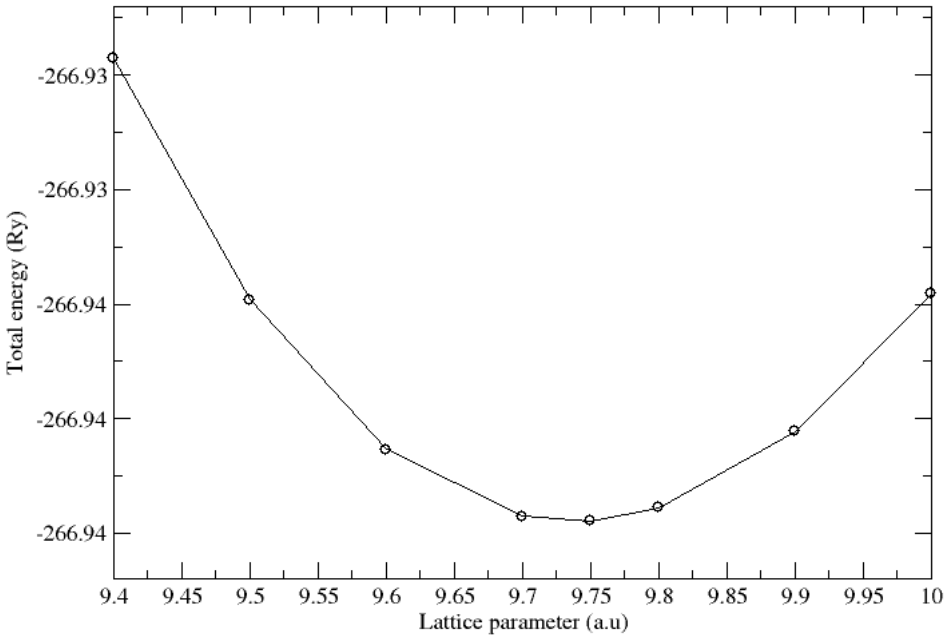

Figure A.27: Optimized lattice constant of RHL NiO with α_{rh} = 33.557^0 using U=12 eV.

The lattice constant of 9.738 a.u was used as it was found to have the lowest energy for RHL NiO with α_{rh} = 33.557^0 for LSDA+U calculations with U term of 12 eV.

APPENDIX B

ELECTRONIC PROPERTIES

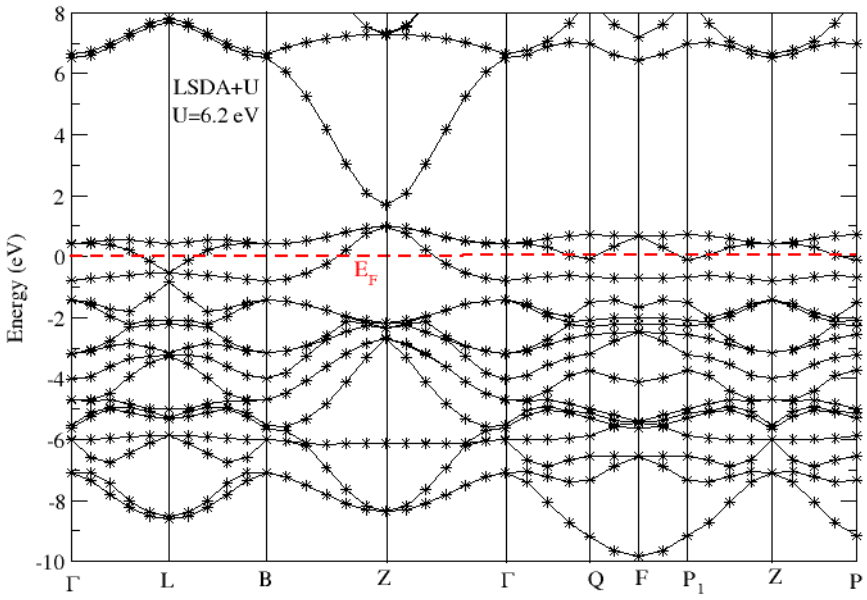

Figure B.1: Band structure of RHL NiO of α_{rh} = 60.08^0 with LSDA+U, U=6.2 eV.

Figure B2 shows the band structure of RHL NiO with α_{rh} = 60.08^0 for LSDA calculations with U term of 6.2 eV. The conduction band and the valence band overlap.

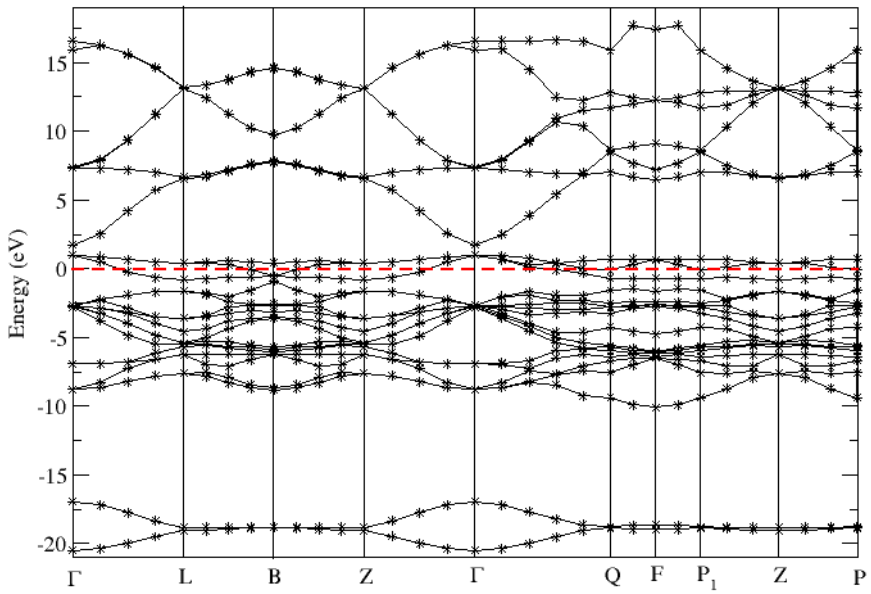

Figure B.2: Band structure of RHL NiO of α_{rh} = 60.08^0 with LSDA+U, U=8 eV.

Figure B1 shows the band structure of RHL NiO with α_{rh} = 60.08^0 for LSDA calculations with U term of 8 eV. The conduction band and the valence band overlap.

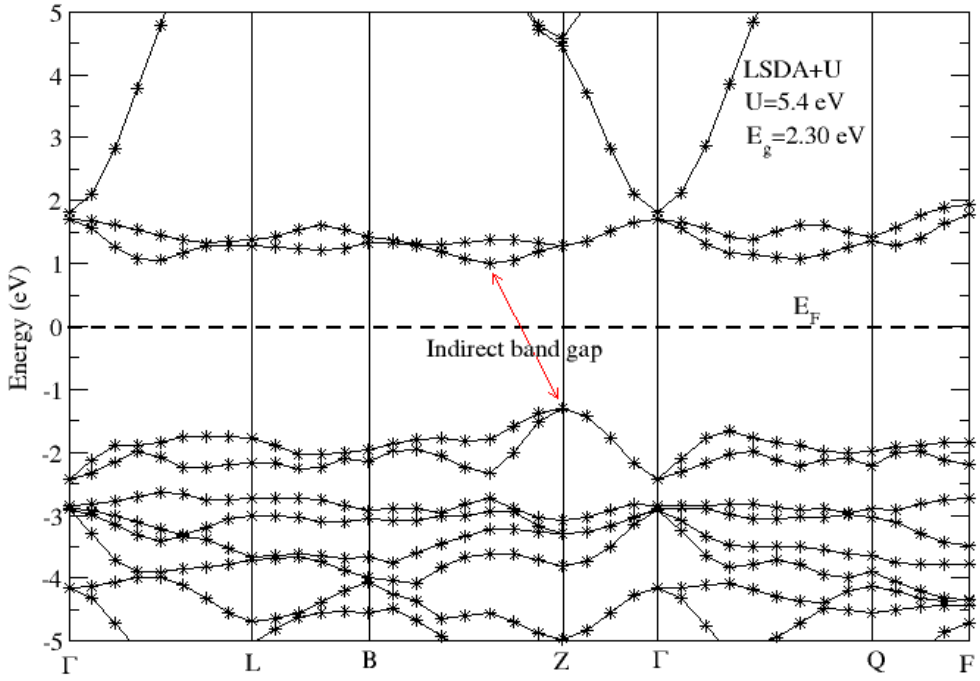

Figure B.3: Band structure of RHL NiO of α_{rh} = 33.557^0 with LSDA+U, U=5.4 eV.

From Figure B3, the minimum indirect and direct band gap values of 2.30 eV and 2.58 eV, respectively, were found for LSDA+U calculations, using Hubbard energy of 5.4 eV.

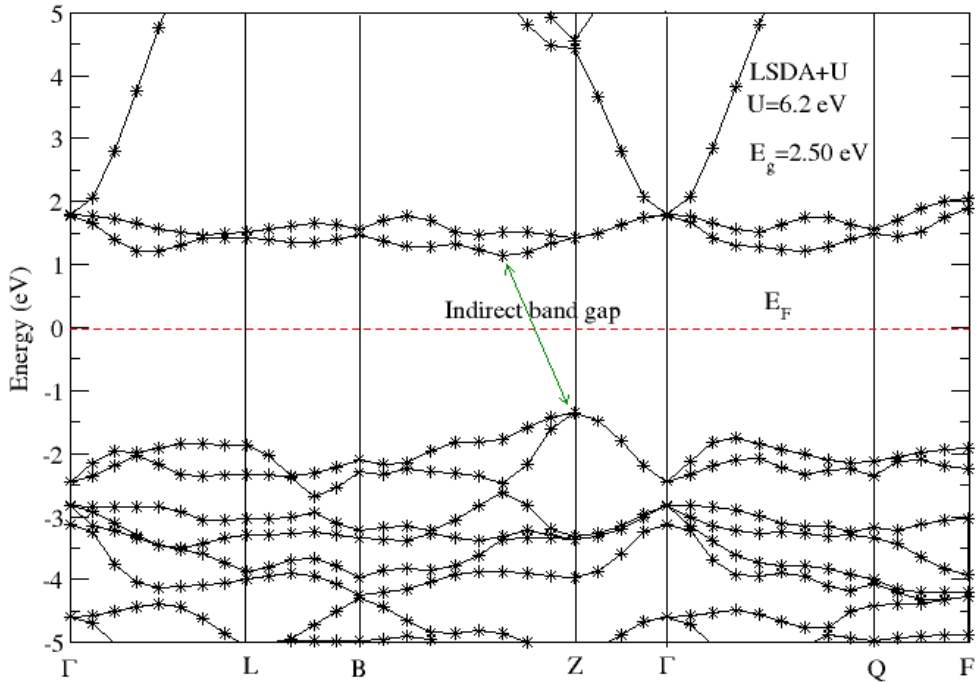

Figure B.4: Band structure of RHL NiO of α_{rh} = 33.557^0 with LSDA+U, U=6.2 eV.

From Figure B4, the minimum indirect and direct band gap values of 2.50 eV and 2.78 eV, respectively, were found for LSDA calculations, using Hubbard energy of 6.2 eV.

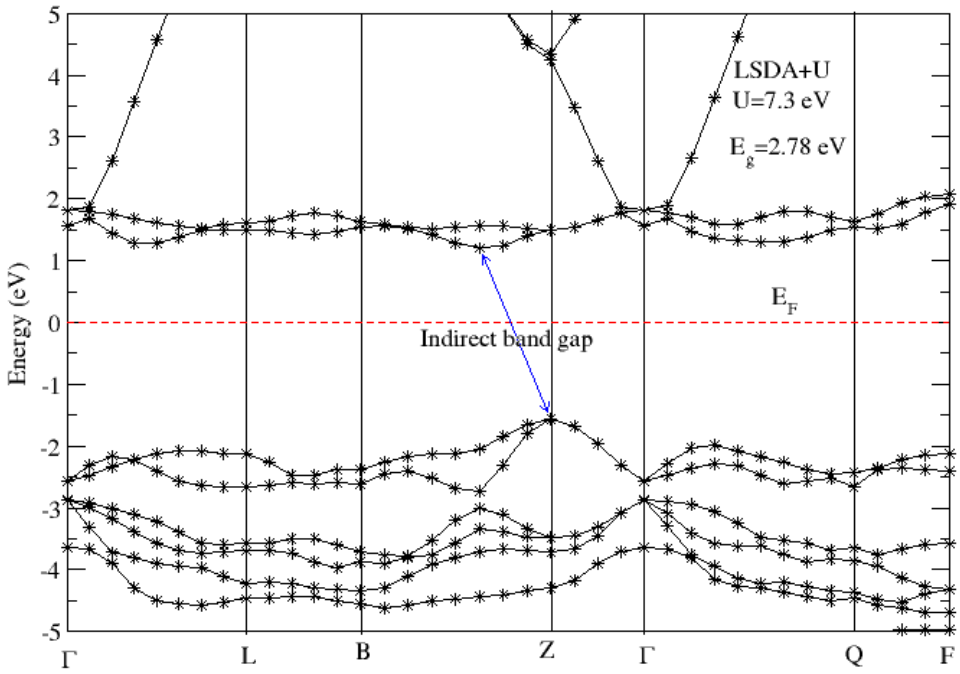

Figure B.5: Band structure of RHL NiO of α_{rh} = 33.557^0 with LSDA+U, U=7.3 eV.

From Figure B5, the minimum indirect and direct band gap values of 2.78 eV and 3.07 eV, respectively, were found using U term of 7.3 eV.

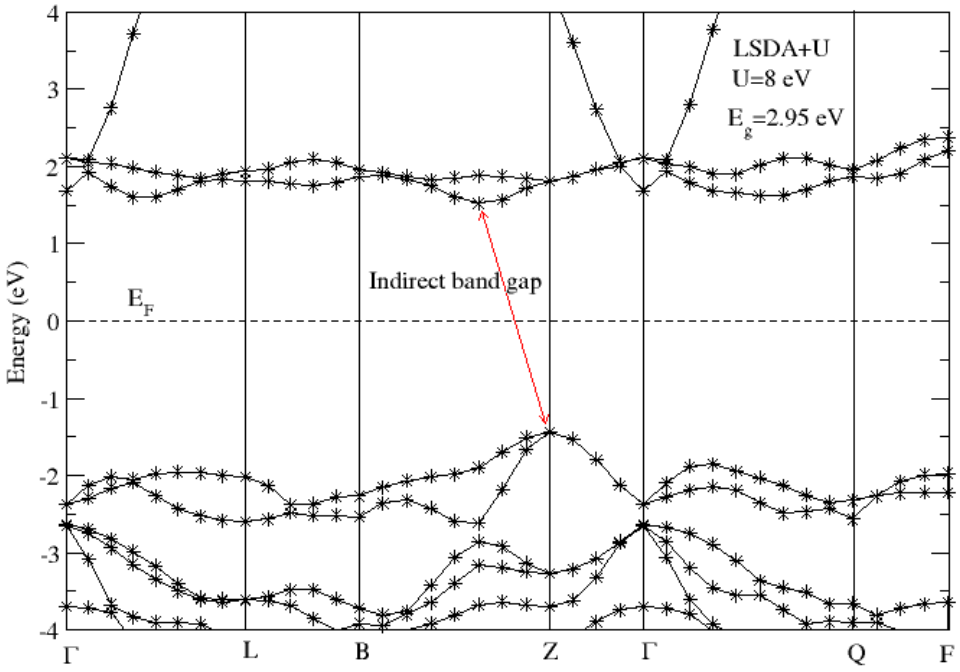

Figure B.6: Band structure of RHL NiO of α_{rh} = 33.557^0 with LSDA+U, U=8 eV.

The minimum indirect and direct band gap values of 2.95 eV and 3.25 eV, respectively, were found using U term of 8 eV.

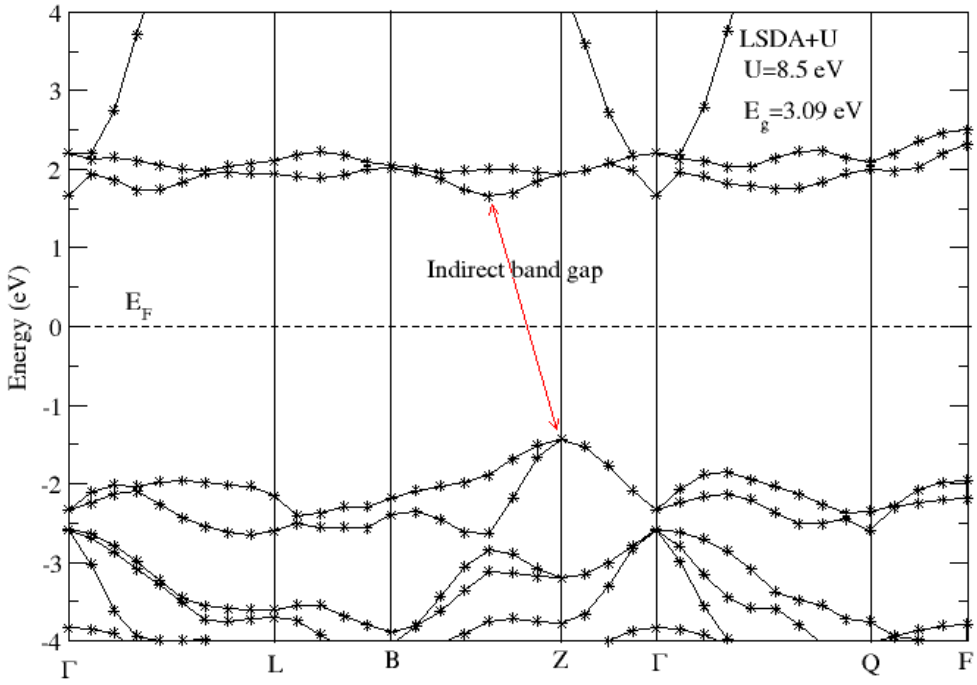

Figure B.7: Band structure of RHL NiO of α_{rh} = 33.557^0 with LSDA+U, U=8.5 eV.

The minimum indirect and direct band gap values of 3.09 eV and 3.38 eV, respectively, were found using U term of 8.5 eV.

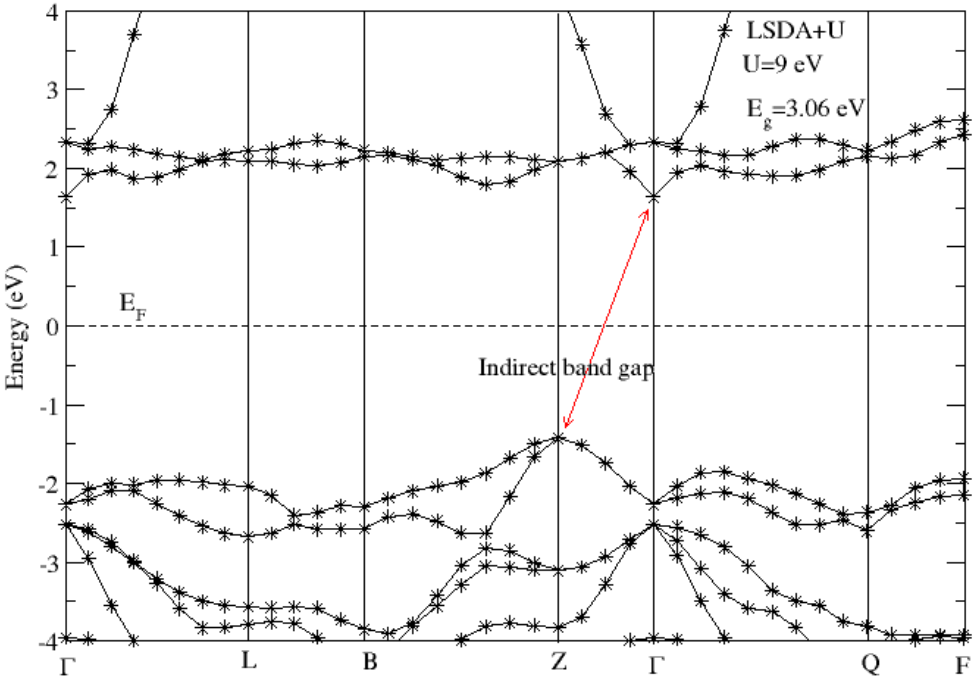

Figure B.8: Band structure of RHL NiO of α_{rh} = 33.557^0 with LSDA+U, U=9 eV.

The minimum indirect and direct band gap values of 3.06 eV and 3.51 eV, respectively, were found using U term of 9 eV.

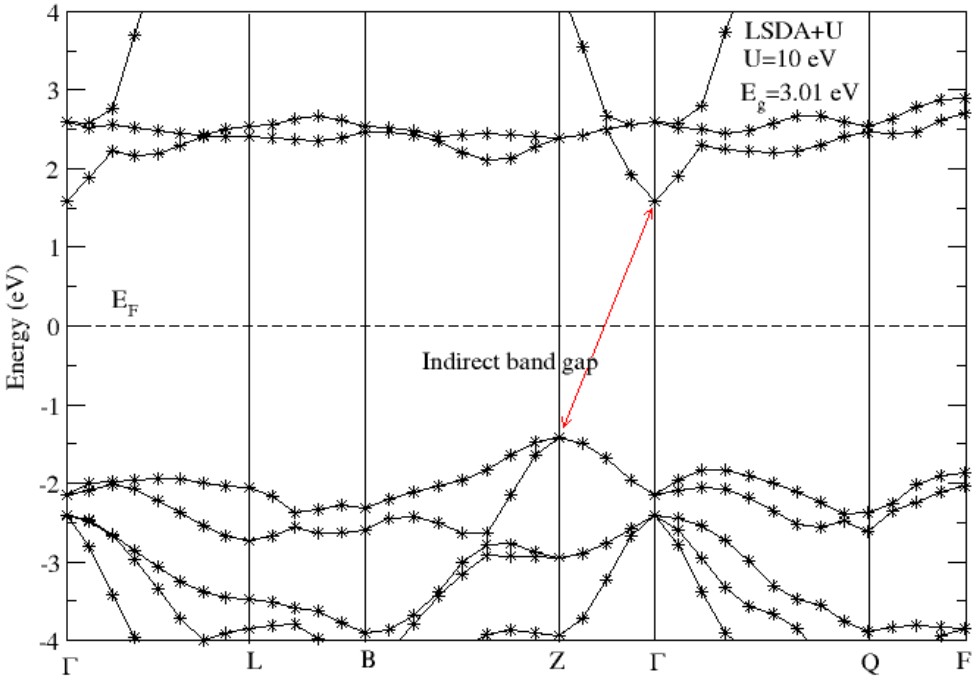

Figure B.9: Band structure of RHL NiO of α_{rh} = 33.557^0 with LSDA+U, U=10 eV.

The minimum indirect and direct band gap values of 3.01 eV and 3.81 eV, respectively, were found using U term of 10 eV.

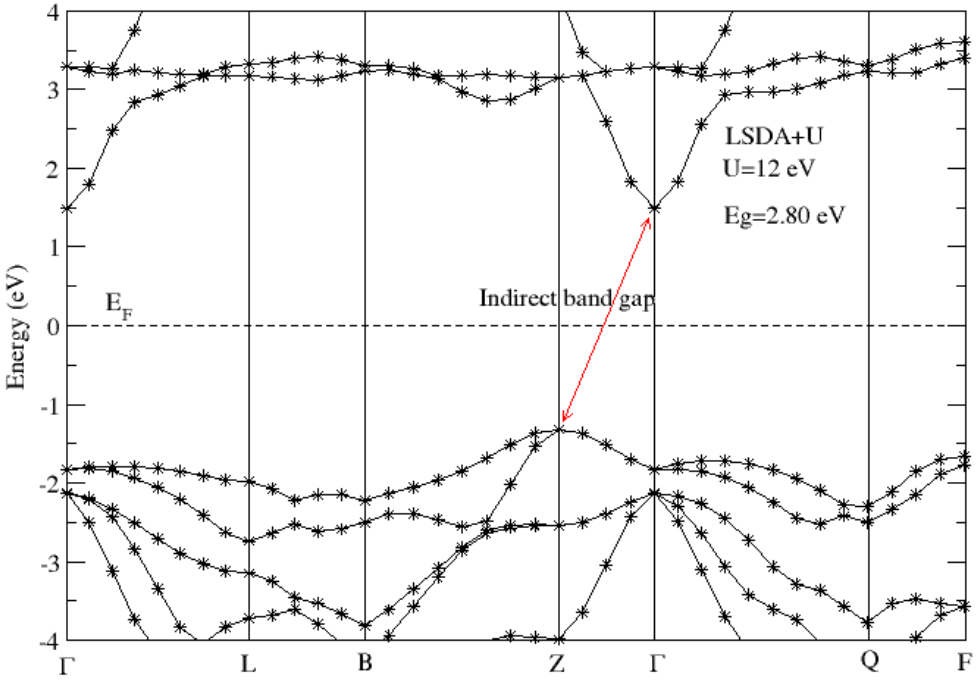

Figure B.10: Band structure of RHL NiO of α_{rh} = 33.557^0 with LSDA+U, U=12 eV.

The minimum indirect and direct band gap values of 2.80 eV and 4.46 eV, respectively, were found using U term of 12 eV.

APPENDIX C

PSEUDOPOTENTIALS USED

Table C.1: Pseudopotentials used for both O and Ni atoms.

Approximation	Type of Atom	Pseudopotential name
LSDA and LSDA+U	Ni	Ni.pz-n-rrkjus_psl.0.1.UPF
	O	O.pz-n-rrkjus_psl.0.1.UPF
GW and BSE	Ni	Ni.pbe-mt_fhi.UPF
	O	O.pbe-mt_fhi.UPF

C.1 Ni.pz-n-rrkjus_psl.0.1.UPF

This pseudopotential was generated using ”atomic” code by A. Dal Corso v.5.0.2 svn rev. 9415

Author: ADC

Generation date: 11 Sep 2012

Pseudopotential type: USPP

Element: Ni

Functional: LDA

Suggested minimum cutoff for wavefunctions: 42 Ry

Suggested minimum cutoff for charge density: 236 Ry

The Pseudo was generated with a Scalar-Relativistic Calculation

Local Potential by smoothing all electron potential with Bessel functions, cutoff radius: 2.1000

Valence configuration:

nl	l	Occupations
4s	0	2.00
4p	1	0.00
3d	2	8.00

C.2 O.pz-n-rrkjus_psl.0.1.UPF

Generated using ”atomic” code by A. Dal Corso v.5.0.2 svn rev. 9415

Author: Lorenzo Paulatto, modified by ADC

Generation date: 11 Sep 2012

Pseudopotential type: USPP

Element: O

Functional: LDA

Suggested minimum cutoff for wavefunctions: 47. Ry

Suggested minimum cutoff for charge density: 323. Ry

The Pseudo was generated with a Scalar-Relativistic Calculation

L component: 2

Cutoff radius for Local Potential: 1.3000

Valence configuration:

nl	l	Occupations
2s	0	2.00
2p	1	4.00

C.3 Ni.pbe-mt_fhi.UPF

Generated using FHI98PP, converted with fhi2upf.x v.5.0.2

Origin: Abinit web site

Date: 23-Jun-2013 (PG)

Pseudopotential type: SL

Element: Ni

Functional: PBE

Suggested minimum cutoff for wavefunctions: 0. Ry

Suggested minimum cutoff for charge density: 0. Ry

The Pseudo was generated with a Non-Relativistic Calculation

L component: 0

Cutoff radius for Local Potential: 0.0000

Valence configuration:

nl	l	Occupations
1s	0	2.00
2p	1	6.00
3d	2	10.00
4d	3	0.00

C.4 O.pbe-mt_fhi.UPF

Generated using FHI98PP, converted with fhi2upf.x v.5.0.2

Origin: Abinit web site

Date: 08-Sep-2012 (PG)

Pseudopotential type: SL

Element: O

Functional: PBE

Suggested minimum cutoff for wavefunctions: 0. Ry

Suggested minimum cutoff for charge density: 0. Ry The Pseudo was generated with a Scalar-Relativistic Calculation

L component: 2

Cutoff radius for Local Potential: 0.0000

Valence configuration:

nl	l	Occupations
1s	0	2.00
2p	1	4.00
3d	2	0.00
4d	3	0.00